Contributions to the Three-Dimensional Vortex Element Method and Spinning Bluff Body Flows

Thesis by
Philippe Chatelain

In Partial Fulfillment of the Requirements
for the Degree of
Doctor of Philosophy

California Institute of Technology
Pasadena, California

2005

(Defended December 3, 2004)

Acknowledgements

I thank my advisor, Anthony Leonard. His open-mindedness, trust and kindness truly shaped this work. None of this would have been possible without my undergraduate advisor, Grégoire Winckelmans, who first introduced me to computational fluid dynamics and vortex methods. Fruitful discussions with Hans Hornung are also acknowledged. My friends and (former) colleagues at the Iris lab, Mark Brady, Gerard O'Reilly, Vincent Wheatley, James Faddy, Nikoo Saber, Paul O'Gorman and Michael Rubel made these five years of work also a fun experience. Michael provided great computing advice and important contributions to this vortex code.

My wife, Caroline gave me her unconditional and invaluable support throughout. Many thanks also go to my parents who always put my education first and never stopped encouraging me. Finally, I do not want to forget my friends, François, Luc and Olivier.

This effort was sponsored by the US Department of Energy under contract No. DE-AC03-98EE50506, and also supported by Caltech discretionary funds. The Master's year was funded by a fellowship of the Belgian American Educational foundation. These contributions are gratefully acknowledged.

Abstract

Several contributions to the three-dimensional vortex element method for incompressible flows are presented. We introduce redistribution schemes based on the hexagonal lattice in two dimensions, and the face-centered cubic lattice in three dimensions. Interpolation properties are studied in the frequency domain and are used to build high-order schemes that are more compact and isotropic than equivalent cubic schemes. We investigate the reconnection of vortex rings at small Reynolds numbers for a variety of configurations. In particular, we trace their dissipative nature to the formation of secondary structures.

A method for flows with moving boundaries is implemented. The contributions of rotating or deforming boundaries to the Biot-Savart law are derived in terms of surface integrals. They are implemented for rigid boundaries in a fast multipole algorithm. Near-wall vorticity is discretized with attached panels. The shape function and Biot-Savart contributions of these elements account for the presence of the boundary and its curvature. A conservative strength exchange scheme was designed to compute the viscous flux from these panels to free elements.

The flow past a spinning sphere is studied for a Reynolds number of 300 and a wall velocity that is equal to half the free-stream velocity. Three directions of the angular velocity are considered. Good agreement with previous numerical and experimental measurements of the force coefficients is observed. Topological features such as the separation and critical points are investigated and compared amongst the configurations.

Finally, preliminary results for flapping motions are presented. Simple rigid geometries are used to model a fish swimming in a free-stream and a flapping plate.

Contents

List of Figures

List of Tables

Chapter 1

The Three-Dimensional Vortex Element Method

1.1 Introduction

Vortex element methods have been growing in popularity since the early 1980's. As their name indicates, they are based on the discretization of vorticity–a quantity that has a compact support in many physical problems–thereby making this approach interesting.

The discretization itself comes in various sorts: filaments, sheets or particles. This last family has shown the most dramatic progression. The treatment of the distortion of the elements and the development of deterministic viscous algorithms have allowed for accurate long-time simulations. During the 1990's, wall boundary conditions and faster algorithms were developed to handle high Reynolds number incompressible flows in two and three dimensions. In recent years, we have seen the application to compressible and reacting flows.

The present work brings contributions to several areas of the method. A particular focus is on the development of a framework to handle moving and deforming boundaries. This opens the way to the simulation of spinning bluff body flows and flapping motions, such as those encountered in biological flows.

This first chapter gives a comprehensive review of the vortex element method for

incompressible flows, with emphases on the approaches and problems that we investigate in later chapters. We end this chapter with an overview of our contributions.

1.2 Fundamentals

1.2.1 Hypothesis and Equations

Vorticity

We are studying the three-dimensional incompressible flow of a viscous fluid. Let us start with the Navier-Stokes' equations

$$\begin{aligned} &\nabla \cdot \mathbf{u} = 0, \\ &\frac{\partial \mathbf{u}}{\partial t} + (\nabla \mathbf{u})\,\mathbf{u} + \nabla\left(\frac{p}{\rho}\right) = \nu \nabla^2 \mathbf{u}\,. \end{aligned} \tag{1.1}$$

The vorticity, $\boldsymbol{\omega}$, is defined as

$$\boldsymbol{\omega} = \nabla \times \mathbf{u}\,.$$

The term $(\nabla \mathbf{u})\,\mathbf{u}$ in Eq. 1.1 can be rewritten as

$$\begin{aligned} (\nabla \mathbf{u})\,\mathbf{u} &= \nabla \cdot (\mathbf{u}\mathbf{u}) \\ &= \boldsymbol{\omega} \times \mathbf{u} + \nabla\left(\frac{\mathbf{u}\cdot\mathbf{u}}{2}\right)\,. \end{aligned} \tag{1.2}$$

With this last result, the curl of Eq. 1.1 becomes

$$\begin{aligned} \nabla \times \left(\frac{\partial \mathbf{u}}{\partial t} + \boldsymbol{\omega} \times \mathbf{u} + \nabla\left(\frac{\mathbf{u}\cdot\mathbf{u}}{2} + \frac{p}{\rho}\right)\right) &= \nabla \times \nu \nabla^2 \mathbf{u} \\ \frac{\partial \boldsymbol{\omega}}{\partial t} + \nabla \times (\boldsymbol{\omega} \times \mathbf{u}) &= \nu\, \nabla^2 \boldsymbol{\omega}\,. \end{aligned} \tag{1.3}$$

Continuing to simplify, we have

$$\frac{\partial \boldsymbol{\omega}}{\partial t} + \nabla \times (\boldsymbol{\omega} \times \mathbf{u}) = \nu \nabla^2 \boldsymbol{\omega}$$

$$\underbrace{\frac{\partial \boldsymbol{\omega}}{\partial t} + (\nabla \boldsymbol{\omega}) \cdot \mathbf{u}}_{=\frac{D\boldsymbol{\omega}}{Dt}} - (\nabla \mathbf{u}) \cdot \boldsymbol{\omega} + \underbrace{\boldsymbol{\omega}\,(\nabla \cdot \mathbf{u})}_{=0} - \underbrace{\mathbf{u}\,(\nabla \cdot \boldsymbol{\omega})}_{=0} = \nu \nabla^2 \boldsymbol{\omega}$$

and finally, we have the evolution equation for vorticity

$$\frac{D\boldsymbol{\omega}}{Dt} = (\nabla \mathbf{u}) \cdot \boldsymbol{\omega} + \nu \nabla^2 \boldsymbol{\omega} \tag{1.4}$$

where the right terms correspond to a stretching effect and a viscous diffusion respectively.

Stream-Function and Velocity

The previous equation allows the computation of the evolution of the vorticity field if the velocity is known. This is made possible through the use of a stream-function $\boldsymbol{\psi}$. We consider the Helmholtz decomposition of velocity

$$\mathbf{u} = \nabla \varphi + \nabla \times \boldsymbol{\psi}, \tag{1.5}$$

with the gauge of $\boldsymbol{\psi}$ set as $\nabla \cdot \boldsymbol{\psi} = 0$. Taking the curl of Eq. 1.5 yields the following Poisson equation for $\boldsymbol{\psi}$:

$$\nabla^2 \boldsymbol{\psi} = -\boldsymbol{\omega}\,. \tag{1.6}$$

The computation of the velocity field therefore requires finding $\boldsymbol{\psi}$ and computing its curl.

1.2.2 Discretization

A Lagrangian method considers the evolution of elements which represent small material volumes V_p. An element is carried by the local flow and carries the integral of some intensive physical quantity f, $\alpha_p = \int_{V_p} f\, dV$. We will refer to this integral as

the strength of the element. We can therefore write the following evolution equations for the position $\mathbf{x}_p$ and strength α_p of an element,

$$\frac{d\mathbf{x}_p}{dt} = \mathbf{u}(\mathbf{x}_p) \tag{1.7}$$

$$\frac{d\alpha_p}{dt} = \int_{V_p} \left(\frac{\partial f}{\partial t} + \nabla \cdot (f\mathbf{u}) \right) d\mathbf{x} \tag{1.8}$$

where Leibniz's theorem was used.

In the context of vortex methods, the physical quantity f is the vorticity $\boldsymbol{\omega}$. For an incompressible three-dimensional flow, the use of Eq. 1.4 in Eq. 1.8 yields

$$\frac{d\mathbf{x}_p}{dt} = \mathbf{u}(\mathbf{x}_p) \tag{1.9}$$

$$\frac{d\boldsymbol{\alpha}_p}{dt} = \int_{V_p} \left((\nabla \mathbf{u}) \cdot \boldsymbol{\omega} + \nu \nabla^2 \boldsymbol{\omega} \right) d\mathbf{x} \tag{1.10}$$

$$= (\nabla \mathbf{u}(\mathbf{x}_p)) \cdot \boldsymbol{\alpha}_p + \nu \int_{V_p} \nabla^2 \boldsymbol{\omega} \, d\mathbf{x} \,, \tag{1.11}$$

where we use a center point rule to evaluate the first term.

We note that our problem has now become a system of ordinary differential equations and that we still need to compute its right-hand side.

1.2.3 Field Computations

Two main families of methods have been proposed to compute velocity from Eqs. 1.6 and 1.5. On the one hand, grid-based solvers have given rise to the so-called Vortex-In-Cell–VIC– methods (see Cottet and Koumoutsakos, 2000, sec. 8.2 and references therein) in which vortex strengths are distributed onto a grid and the velocity field is computed using Eqs. 1.5 and 1.6 and interpolated at the particle positions. This kind of approach is effective for periodic problems, but must be modified to enforce far field boundary conditions.

On the other, we use a second approach which is in a sense, grid-less, and implicitly imposes boundary conditions at infinity. We consider volume elements where the

distribution is singular and the strength is concentrated at the particle center,

$$\boldsymbol{\omega} = \sum_p \boldsymbol{\alpha}_p \delta(\mathbf{x} - \mathbf{x}_p) \; .$$

We can then use the fundamental solution of $-\nabla^2$:

$$-\nabla^2 G(\mathbf{x}, \mathbf{x}') = \delta(\mathbf{x} - \mathbf{x}') \, . \tag{1.12}$$

G is also called the free-space Green's function. In three dimensions, it is given by

$$G(\mathbf{x}, \mathbf{x}') = \frac{1}{4\pi} \left| \mathbf{x} - \mathbf{x}' \right|^{-1} \tag{1.13}$$

and is a radial function which we will write as $G(|\mathbf{x} - \mathbf{x}'|)$ from here on. In this approach, field computation thus amounts to a summation over the elements

$$\boldsymbol{\psi}(\mathbf{x}) = \sum_p G(|\mathbf{x} - \mathbf{x}_p|) \boldsymbol{\alpha}_p \tag{1.14}$$

$$\mathbf{u}(\mathbf{x}) = \sum_p \nabla \left(G(|\mathbf{x} - \mathbf{x}_p|) \right) \times \boldsymbol{\alpha}_p = \sum_p \mathbf{K} \left(\mathbf{x} - \mathbf{x}_p \right) \times \boldsymbol{\alpha}_p \, , \tag{1.15}$$

where we introduce $\mathbf{K} = \nabla G$.

This approach however can encounter stability problems because of the singularities the velocity field displays (Winckelmans and Leonard, 1993). Instead we employ a regularized distribution for the particles $\boldsymbol{\omega}_\sigma = \sum_p \boldsymbol{\alpha}_p \zeta_\sigma(\mathbf{x} - \mathbf{x}_p)$, where σ is a smoothing radius. ζ_σ induces smooth stream function and velocity contributions G_σ and $\mathbf{K}_\sigma$, respectively.

In our implementation, ζ_σ is a Gaussian,

$$\zeta_\sigma(|\mathbf{x}|) = \frac{1}{(2\pi)^{3/2}\sigma^3}\, e^{-\frac{r}{2\sigma^2}} \tag{1.16}$$

$$G_\sigma(|\mathbf{x}|) = \frac{1}{4\pi}\frac{\operatorname{erf}\left(\frac{|\mathbf{x}|}{\sqrt{2}\sigma}\right)}{|\mathbf{x}|} \tag{1.17}$$

$$\mathbf{K}_\sigma(\mathbf{x}) = \frac{-\mathbf{x}}{4\pi|\mathbf{x}|^3}\left(\operatorname{erf}\left(\frac{|\mathbf{x}|}{\sqrt{2}\sigma}\right) - \sqrt{\frac{2}{\pi}}\frac{|\mathbf{x}|}{\sigma}e^{-|\mathbf{x}|^2/2\sigma^2}\right) \tag{1.18}$$

One can find more thorough discussions of the topic of this section in Winckelmans (2004) and Cottet and Koumoutsakos (2000).

1.2.4 Viscous Term

The second term in Eq. 1.11 still needs to be computed. Several techniques have been proposed. Random-walk methods move the elements in a Brownian motion fashion (Chorin, 1973). Re-sampling methods act on the strengths of the elements by sampling the exact solution of the viscous diffusion of singularities at the particle locations. Our approach follows the method of Degond and Mas-Gallic (1989) which is known as the particle strength exchange (PSE) scheme. It is based on an integral representation of the Laplace operator. In $\mathbb{R}^3$, one can indeed write

$$\nabla^2 f(\mathbf{y}) \simeq \frac{2}{\sigma^2}\int \eta_\sigma(\mathbf{x}-\mathbf{y})\,(f(\mathbf{x})-f(\mathbf{y}))\,d\mathbf{x} \;+\; O(\sigma^r)\,, \tag{1.19}$$

which, integrated over the volume of an element, yields

$$\int_{V_p}\nabla^2 f\,d\mathbf{y} \simeq \int\frac{2}{\sigma^2}\int\eta_\sigma(\mathbf{x}-\mathbf{y})\,(f(\mathbf{x})-f(\mathbf{y}))\,d\mathbf{x}\,d\mathbf{y}\,. \tag{1.20}$$

The kernel η_σ has to satisfy moment conditions (Degond and Mas-Gallic, 1989, Cottet and Koumoutsakos, 2000). We have

$$\begin{aligned} &\int x_i x_j \eta_\sigma(\mathbf{x}) d\mathbf{x} = \delta_{ij} \text{ for } i,\ j = 1,2,3 \\ &\int x_i^{i_1} x_j^{i_2} \eta_\sigma(\mathbf{x}) d\mathbf{x} = 0 \text{ for } i_1 + i_2 = 1 \text{ or } 3 \leq i_1 + i_2 \leq r+1 \\ &\int |\mathbf{x}|^{r+2} \eta_\sigma(\mathbf{x}) d\mathbf{x} < \infty \end{aligned} \tag{1.21}$$

One technique to build a kernel η consists in using the function ζ

$$\eta(\rho) = -\frac{1}{\rho}\frac{d}{d\rho}\zeta(\rho)\,, \tag{1.22}$$

which in the case of the Gaussian yields the same Gaussian. If one considers a pair (p, q) of vortex elements, the integral of Eq. 1.20 has a simple expression

$$\left.\frac{d\boldsymbol{\alpha}_p}{dt}\right|_{\text{visc. } q} \simeq \frac{2}{\sigma^2}\eta_\sigma(\mathbf{x}_p - \mathbf{x}_q)\left(V_p\,\boldsymbol{\alpha}_q - V_q\,\boldsymbol{\alpha}_p\right)\ , \tag{1.23}$$

which shows that the scheme is conservative. Ploumhans (2001) proved the convergence of the PSE for particles with a smoothly varying core size σ. This result allows the use of coarser particle distributions in the wake of bluff body flows (Chapter 6).

1.2.5 Wall-Bounded Flows

There are many challenges when dealing with boundaries. Koumoutsakos et al. (1994) and Koumoutsakos and Leonard (1995) introduced a scheme to account for vorticity creation at the wall. This scheme is based on the model of Lighthill (1963) and consists in the incremental introduction of vorticity in the form of vorticity sheets at the boundaries. At every application, the sheet enforces the no-slip condition. Because this sheet $\boldsymbol{\gamma}$ appears within a time step δt, the compatibility with a Neumann boundary condition is immediate

$$\nu\frac{\partial\omega}{\partial n} = \frac{\boldsymbol{\gamma}}{\delta t}\,. \tag{1.24}$$

The sheet strength, $\boldsymbol{\gamma}$, first has to be found using a boundary element method, and then diffused into the flow. Chapter 4 will cover this topic.

Boundaries also affect the order of the method because the interpolation and integration over the elements assumes an unbounded space. Our spherical test functions let some vorticity leak across the boundary and will require completing the set with images to cancel spurious viscous fluxes through the wall. Chapter 5 introduces attached elements with specific test functions to alleviate this problem.

1.2.6 Vorticity Divergence

One issue that is peculiar to three dimensions is the divergence problem. Vorticity is the curl of the velocity field, and as such, it satisfies

$$\nabla \cdot \boldsymbol{\omega} = \nabla \cdot (\nabla \times \mathbf{u}) = 0 \, . \tag{1.25}$$

In two dimensions, this condition is met because $\boldsymbol{\omega} = \omega_z(x, y)\, \mathbf{e}_z$. In three dimensions however, the discretized vorticity field will differ slightly from a solenoidal field. This problem is discussed further in Chapters 2 and 6.

1.3 Numerics

1.3.1 Field Computations Acceleration

The summations in Eq. 1.14 and 1.15 imply a $O(N^2)$ cost when one computes the fields at the positions of all the elements, thus making it intractable even for modest problem sizes.

If we consider the sum for a fixed $\mathbf{x}$, we notice that the contribution of a remote cluster of particles can be closely approximated by the influence of one virtual particle located at the center of the group. This is the central idea of multipole expansions and tree codes; the set is sorted geometrically and hierarchically into a tree and a branch cell contains information about the particles it (or its offspring) contains.

One also needs an error control algorithm so to keep the approximation accurate to a prescribed level. The summation now reduces to a tree traversal. For a given branch, the recursion consists in computing the interactions of its offspring if the error criterion is not met or stopping at the branch and using its multipole information otherwise. The loop is initiated by starting with the root cell.

There are evidently variations on this idea. For more information, one may refer to Barnes and Hut (1986), Salmon et al. (1994), Salmon and Warren (1994) and Winckelmans et al. (1995).

1.3.2 Clustering and Depletion

Because vortex elements follow the flow, they tend to cluster along axes of compression and become depleted regions of stretching. This affects the convergence of the method, which is based on integration and interpolation over all space. Historically, the first convergence results for the three-dimensional method were derived by Beale and Majda (1982). One may refer to Cottet and Koumoutsakos (2000) for a recent proof and a complete historical list of references.

A central idea of these convergence results is that the error grows with some power of h/σ and σ^r, where h is the spacing between the particles and r of the highest vanishing moment of the mollifying function. The Gaussian of Eq. 1.16 has $r = 2$. It is therefore important to keep a regular set of overlapping elements. Several techniques have been designed in this regard; we use particle location processing–redistribution which creates a new undistorted set of elements from the old one. This technique was used in all our simulations and will be covered in details in Chapter 2 as we investigate new arrangements for the particles.

1.3.3 Time Integration

Anderson and Greengard (1985) showed that, for an inviscid problem, the time integration stability condition does not affect the convergence of the vortex method, i.e., the convergence rate is $O(\sigma^r + \delta t^s)$ where s is the order of the time integration. In

practice, this theoretical unconditional stability is tempered by other factors such as the divergence problem or the presence of boundaries.

We use a second order Adams-Bashforth (AB2) scheme. A Runge-Kutta 2 (RK2) scheme is used at the start, or when we have to restart the integration after a redistribution. The stability of the PSE integrated with AB2 is constrained by (Ploumhans, 2001)

$$r_{\text{PSE}} = \frac{\nu\,\Delta t}{h^2} < 0.267\,. \tag{1.26}$$

As mentioned above, there is no Courant-Friedrich-Levy condition, relating the particle size to the time step,

$$\frac{U_{max}\,\Delta t}{h} < O(1)\,. \tag{1.27}$$

For a bounded flow however, a time-step too large will lead to particles crossing boundaries. This last quantity will therefore be monitored near the walls. Other expressions more suitable for a Lagrangian method have been proposed:

$$\text{CFL} = |\boldsymbol{\omega}|_{\max}\,\Delta t \text{ or } |\nabla\mathbf{u}|_{\max}\,\Delta t\,. \tag{1.28}$$

A last condition concerns the mesh Reynolds number

$$Re_h = \frac{U_{max}\,h}{\nu} \lesssim 2\,. \tag{1.29}$$

For vortex methods, there is a more appropriate expression,

$$Re_h = \frac{|\boldsymbol{\omega}|_{max}\,h^2}{\nu}\,. \tag{1.30}$$

It is not independent from the two preceding conditions since

$$\text{CFL} = Re_h\,r_{\text{PSE}}\,. \tag{1.31}$$

1.4 Overview

Chapter 2 presents an alternative to the existing redistribution schemes based on the face-centered cubic lattices. Compactness and isotropy are benefited from the symmetry properties of this lattice.

Chapter 3 studies the physics of the reconnections of vortex rings from various standpoints and in particular, the energy spectrum.

Chapters 4 to 7 present work that broadens the applicability of the method to moving and deforming geometries. The case of spinning spheres at $Re = 300$ is considered in Chapter 6. Chapter 5 proposes a new element class to represent near-wall vorticity to alleviate regularization problems in those regions. These elements also implement some of the boundary conditions required in flows with deforming and rotating boundaries. Chapter 7 discusses preliminary results for flapping and swimming motions.

Chapter 8 concludes this thesis. It includes a discussion of our results, and directions of future work.

Chapter 2

Face-Centered Cubic Redistributions

2.1 Introduction

As we have seen in Chapter 1, the vortex element method strongly depends on integration and interpolation. In particular, this translates into accuracy degradation when our interpolating elements get too far apart.

One can follow a few different approaches to tackle this problem. One approach consists in progressively introducing new elements in the domain. While elegant, this approach requires a costly algorithm to find the new elements' positions and strengths (see Gharakhani, 2001).

The other approach is to build a whole new set of elements from the old ones. This process must take place every few time steps in order to prevent the particle distribution from getting too distorted. This redistribution process consists in interpolating the new strengths at the nodes of a new non-distorted lattice.

2.2 Redistribution Properties

A redistribution scheme has two components: a lattice and an interpolation function. The term lattice is preferred to mesh because it remains a mathematical object and can span an unbounded region of $\mathbb{R}^3$. Concretely, the lattice nodes are never stored in an array; they are generated on demand.

Ploumhans and Winckelmans (2000) proved the second order accuracy of the particle strength exchange for elements with a smoothly varying size. One can thus use a stretched lattice for problems where it is interesting to vary the resolution. This method will be applied to the simulation of bluff body flows in Chapter 6 and 7.

The interpolation rule will be characterized in terms of its smoothness, order of accuracy and support (Fig. 2.1). We will introduce and generalize some results from Cottet and Koumoutsakos (2000). A central result concerns the order of interpolation.

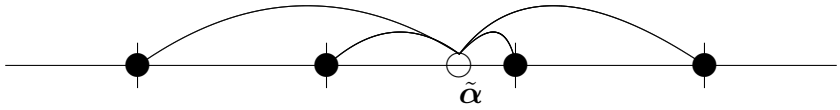

Figure 2.1: Redistribution in one dimension: the strength of a particle of the distorted set (open circle) is redistributed onto four nodes (solid circles)

Let us define the new particles with positions $\mathbf{x}_p$ and strengths $\boldsymbol{\alpha}_p$ as

$$\boldsymbol{\alpha}_p = \sum_q \tilde{\boldsymbol{\alpha}}_q W\left(\frac{\mathbf{x}_p - \tilde{\mathbf{x}}_q}{h}\right) \tag{2.1}$$

in terms of the interpolation function W and the old positions and strengths $\tilde{\mathbf{x}}_q$ $\tilde{\boldsymbol{\alpha}}_q$. If we consider an interpolated quantity $\sum_p \boldsymbol{\alpha}_p \phi(\mathbf{x} - \mathbf{x}_p)$ e.g. vorticity or velocity, the discrepancy we introduce can be written as

$$\begin{aligned} E(\mathbf{x}) &= \sum_p \tilde{\boldsymbol{\alpha}}_p \phi(\mathbf{x} - \tilde{\mathbf{x}}_p) - \sum_p \boldsymbol{\alpha}_p \phi(\mathbf{x} - \mathbf{x}_p) \\ &= \sum_p \tilde{\boldsymbol{\alpha}}_p \left[\phi(\mathbf{x} - \tilde{\mathbf{x}}_p) - \sum_q \phi(\mathbf{x} - \mathbf{x}_q) W\left(\frac{\mathbf{x}_q - \tilde{\mathbf{x}}_p}{h}\right)\right] \end{aligned}$$

The error behavior will thus be dictated by the factor inside the square brackets, which we can express as

$$f(\mathbf{x} - \tilde{\mathbf{x}}_p) = \sum_q \left(\phi(\mathbf{x} - \tilde{\mathbf{x}}_p) - \phi(\mathbf{x} - \mathbf{x}_q)\right) W\left(\frac{\mathbf{x}_q - \tilde{\mathbf{x}}_p}{h}\right). \tag{2.2}$$

To obtain the above expression, we have imposed

$$\sum_q W(\mathbf{x} - \mathbf{x}_q) = 1\,, \tag{2.3}$$

which is physically equivalent to the conservation of circulation. In order to bound f, we expand ϕ about $\mathbf{x} - \mathbf{x}_q$,

$$f(\mathbf{x} - \tilde{\mathbf{x}}_p) = \sum_q \sum_{|\boldsymbol{\beta}|=1\cdots\infty} (-1)^{|\boldsymbol{\beta}|} \left(\mathbf{x}_q - \tilde{\mathbf{x}}_p\right)^{\boldsymbol{\beta}} \partial_{\boldsymbol{\beta}}\phi(\mathbf{x} - \mathbf{x}_q) W\left(\frac{\mathbf{x}_q - \tilde{\mathbf{x}}_p}{h}\right)\,, \tag{2.4}$$

where $\boldsymbol{\beta} = \boldsymbol{\beta}_1 \cdots \boldsymbol{\beta}_n$ are n-tuples with $|\boldsymbol{\beta}| = \boldsymbol{\beta}_1 + \cdots + \boldsymbol{\beta}_n$. It is readily seen from this last expression that the moments of W will characterize the error behavior, i.e., if

$$\sum_q \mathbf{x}_q^{\boldsymbol{\beta}}\, W\left(\frac{\mathbf{x} - \mathbf{x}_q}{h}\right) = \mathbf{x}^{\boldsymbol{\beta}} \text{ for } 0 \leq |\boldsymbol{\beta}| \leq m - 1 \tag{2.5}$$

then

$$E \sim O\left(h^m\right)\,. \tag{2.6}$$

One may refer to Cottet and Koumoutsakos (2000) for a full proof.

Our work focuses on the development and study of interpolation functions W on a different family of lattices. For this reason, we introduce a notation that reflects the arrangement of the new points $\mathbf{x_n} = h\mathbf{Rn}$, in the fashion of Merserau (1979) and Van De Ville et al. (2004). $\mathbf{R}$ is the matrix whose columns are the principal directions of the lattice. Let us also define the matrix $\hat{\mathbf{R}} = (\mathbf{R}^{-1})^t$ which defines a dual lattice. h is the lattice step and being just a rescaling, it will be dropped from the remainder of this chapter for the sake of clarity.

Let us now consider the properties of the Fourier transform of the interpolation kernel. The switch to Fourier space will indeed facilitate the development of high order schemes. Theorem 7.2.1 from Cottet and Koumoutsakos (2000) and Schoenberg (1973) can be generalized to multi-dimensional cases and any kind of lattice as follows.

Theorem 1. *Consider the interpolation formula*

$$Q(\mathbf{x}) = \sum_{\mathbf{n}} q_{\mathbf{Rn}} W\left(\mathbf{x} - \mathbf{Rn}\right) ,$$

where $q_{\mathbf{Rn}}$ *is the weight of the point* $\mathbf{Rn}$*. Let the interpolation function decay fast enough to satisfy the condition*

$$|W\left(\mathbf{x}\right)| \leq Ae^{-B|\mathbf{x}|}, \text{ where } A > 0,\ B > 0.$$

The formula is of degree m *if the following two conditions on* $g(k) = \int W(\mathbf{x}) e^{-i\mathbf{kx}}\, d\mathbf{x}$ *hold simultaneously:*

$$g(\mathbf{k}) - |\mathbf{R}| \text{ has a zero of order } m \text{ at } \mathbf{k} = 0\,, \tag{2.7}$$

$$g(\mathbf{k}) \text{ has zeros of order } m \text{ or higher at all } \mathbf{k} = 2\pi\hat{\mathbf{R}}\mathbf{n}\ (\mathbf{n} \neq 0). \tag{2.8}$$

Proof. Let us consider the interpolation function in lattice coordinates $\boldsymbol{\chi}$; by definition we have for $V(\boldsymbol{\chi})$

$$\int V(\boldsymbol{\eta}) e^{-i(\boldsymbol{\kappa}+2\pi\mathbf{n})\cdot\boldsymbol{\eta}} d\boldsymbol{\eta} = \hat{V}\left(\boldsymbol{\kappa} + 2\pi\mathbf{n}\right) .$$

Following Cottet and Koumoutsakos (2000), we multiply both sides by $e^{2\pi\mathbf{n}\cdot\boldsymbol{\chi}}$, sum over $\mathbf{n}$, then use the Poisson summation formula on the left-hand side:

$$\sum_{\mathbf{n}} e^{2\pi i\mathbf{n}\cdot\boldsymbol{\chi}} \int V(\boldsymbol{\eta}) e^{-i(\boldsymbol{\kappa}+2\pi\mathbf{n})\cdot\boldsymbol{\eta}} d\boldsymbol{\eta} = \sum_{\mathbf{n}} e^{2\pi\mathbf{n}\cdot\boldsymbol{\chi}} \hat{V}\left(\boldsymbol{\kappa} + 2\pi\mathbf{n}\right) \tag{2.9}$$

$$\sum_{\mathbf{n}} e^{i\boldsymbol{\kappa}\cdot(\boldsymbol{\chi}-\mathbf{n})}\, V(\boldsymbol{\chi} - \mathbf{n}) = \sum_{\mathbf{n}} e^{2\pi\mathbf{n}\cdot\boldsymbol{\chi}} \hat{V}\left(\boldsymbol{\kappa} + 2\pi\mathbf{n}\right) . \tag{2.10}$$

We now reintroduce the physical coordinates $\mathbf{x} = \mathbf{R}\boldsymbol{\chi}$ and define W as $V(\boldsymbol{\chi}) = W(\mathbf{x})$.

We have $\hat{V}(\boldsymbol{\kappa}) = \hat{W}(\hat{\mathbf{R}}\boldsymbol{\kappa})/\left|\mathbf{R}\right|$ and

$$\begin{aligned}
\sum_{\mathbf{n}} e^{i\boldsymbol{\kappa}\cdot\mathbf{n}}\, W\left(\mathbf{x}-\mathbf{R}\mathbf{n}\right) &= e^{i\boldsymbol{\kappa}\cdot\boldsymbol{\chi}} \sum_{\mathbf{n}} e^{2\pi\mathbf{n}\cdot\boldsymbol{\chi}} \frac{\hat{W}\left(\hat{\mathbf{R}}\boldsymbol{\kappa}+2\pi\hat{\mathbf{R}}\mathbf{n}\right)}{\left|\mathbf{R}\right|} \\
\sum_{\mathbf{n}} e^{i\mathbf{k}\cdot\mathbf{R}\mathbf{n}}\, W\left(\mathbf{x}-\mathbf{R}\mathbf{n}\right) &= e^{i\mathbf{k}\cdot\mathbf{x}} \sum_{\mathbf{n}} e^{2\pi\hat{\mathbf{R}}\mathbf{n}\cdot\mathbf{x}} \frac{\hat{W}\left(\mathbf{k}+2\pi\hat{\mathbf{R}}\mathbf{n}\right)}{\left|\mathbf{R}\right|}
\end{aligned} \tag{2.11}$$

where we let $\mathbf{k} = \hat{\mathbf{R}}\boldsymbol{\kappa}$, the physical frequency. We then proceed as in Cottet and Koumoutsakos (2000): we develop $e^{i\mathbf{k}\cdot\mathbf{R}\mathbf{n}}$ about 0 in the left-hand side and use the conditions 2.7 and 2.8 on the right-hand side

$$\begin{aligned}
\sum_{\nu} \frac{i^{|\nu|}\mathbf{k}^{\nu}}{\nu!} \sum_{\mathbf{n}} \left(\mathbf{R}\mathbf{n}\right)^{\nu} W\left(\mathbf{x}-\mathbf{R}\mathbf{n}\right) &= e^{i\mathbf{k}\cdot\mathbf{x}} \frac{\hat{W}\left(\mathbf{k}\right)}{\left|\mathbf{R}\right|} + \mathcal{O}\left(\mathbf{k}^{m}\right) \\
&= \sum_{\nu} \frac{i^{|\nu|}\mathbf{k}^{\nu}}{\nu!}\mathbf{x}^{\nu} + \mathcal{O}\left(\mathbf{k}^{m}\right) .
\end{aligned}$$

The identification of the coefficients of $\mathbf{k}$ shows that the interpolation is of order m. □

2.3 Hexagonal and Face-Centered Cubic Redistributions

2.3.1 Lattice Properties

The face-centered cubic lattice can be introduced in a couple of different ways, through mathematics or crystallography, for example. Let us first consider the latter perspective. A lattice can be defined in terms of a unit cell. It is the simplest repeating unit in the crystal, has parallel opposite faces, and its edges connect equivalent points of the lattice.

The face-centered cubic lattice bears its name from the configuration of its unit cell (see Fig. 2.2). It is cubic and has additional lattice sites at the center of its faces.

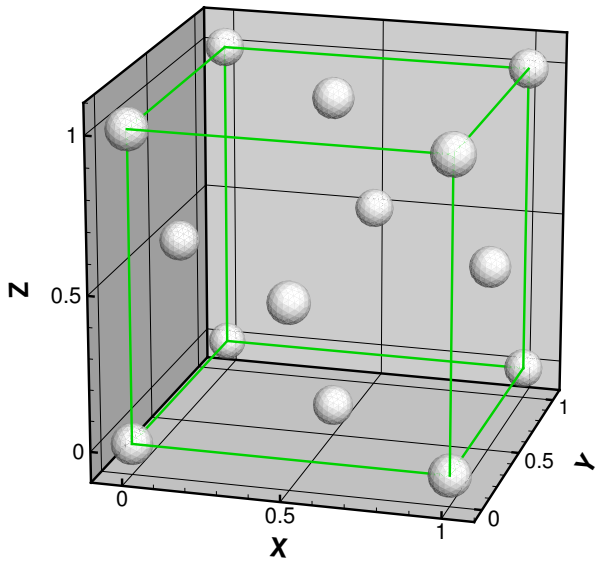

Figure 2.2: Face-centered cubic lattice: unit cell

The FCC lattice can also be constructed as the periodic stack of two-dimensional hexagonal lattices with the spacing between the layers at $\sqrt{6}/3h$ (Fig. 2.3(a)). There are three hexagonal lattices in a period A, B and C; if B lies at the origin of the coordinate system in Fig. 2.3(b), A is shifted by $\left(-1/2, -\sqrt{3}/6\right)$ and C, by $\left(1/2, \sqrt{3}/6\right)$.

This construction scheme highlights an outstanding feature of this lattice: it corresponds to the packing of spheres. As a matter of fact, the FCC lattice is one of two lattices that pack spheres the most densely. It is also called the Cubic Close Packing lattice. The second lattice to achieve this is the Hexagonal Close Packing lattice which is built from the packing of two families of hexagonal lattices.

On a side note, the question of finding the densest arrangement of spheres is an old and famous problem in mathematics. Kepler (Strena sue de nive sexangula, 1611) conjectured that the CCP— or FCC— and HCP lattices offered the densest arrangements with a density of $\frac{\pi}{\sqrt{18}} \approx 0.74048$. This conjecture was studied for centuries, starting with Gauss (1876) and proved only recently by Hales (1992, 1997a,b).

The equivalent close-packing lattice in two dimensions is obviously the hexagonal

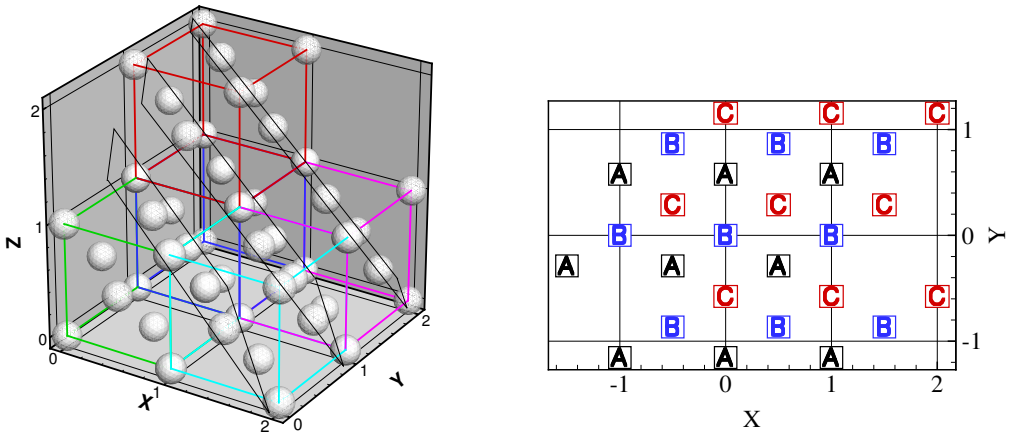

(a) Unit cells and hexagonal planes

(b) Hexagonal lattices

Figure 2.3: Face-centered cubic lattice: construction with three families of hexagonal lattices

one which we used in the construction of Fig. 2.3(b). This lattice already has the interest of the image treatment community (Merserau (1979) and Van De Ville et al. (2004)). On the one hand, it can be the pixel pattern of a sensor that will produce digital images with the same pattern. On the other, it can be interesting to resample and work on digitized images of that nature for their treatment because of the properties of the hexagonal lattice, e.g. edge recognition, etc.

The advantages in our frame-work are also abundant. The VEM indeed uses test and smoothing functions that have spherical–cylindrical in 2D–symmetry. The close packing property is associated with very good symmetry and isotropy; a lattice site is surrounded by 12 equidistant neighbors, compared to 6 for a cubic lattice. These natural properties can be beneficial in several ways:

1. The core overlap issue: Vortex elements on a FCC lattice will supposedly display a better behavior when subjected to strain.

2. Redistribution functions: The lattice symmetries can be used to design more isotropic and compact schemes.

3. The interaction with boundaries: The numerous symmetries will help reduce noise in quantities measured at the wall.

Finally, let us mention that the matrices $\mathbf{R}$ and $\hat{\mathbf{R}}$ for the hexagonal and FCC lattices are given in appendix A.

2.3.2 Interpolation Functions

Due to the nature of the close-packing lattices, we cannot use the tensor product of known one-dimensional functions to interpolate the particles strengths onto the new sites. The use of the lattice coordinates would indeed lead to a non-isotropic redistribution. The scheme construction has to be carried out in two and three dimensions from the start. We propose two methods to build interpolation functions for the hexagonal and FCC lattices.

Splines

In a first approach, one can use the same idea as for one-dimensional splines. It consists in starting from the lowest order "closest-point" function and then taking successive convolutions of this function with itself. For two or three dimensions such a function is also called the indicator function of the *Voronoi* cell $\mathfrak{C}$(Van De Ville et al., 2004) and is defined as

$$\chi(\mathbf{x}) = \begin{cases} 1 & \mathbf{x} \in \mathfrak{C} \\ 1/m_{\mathbf{x}} & \mathbf{x} \in \partial\mathfrak{C} \\ 0 & \mathbf{x} \notin \mathfrak{C} \end{cases} \tag{2.12}$$

where $m_{\mathbf{x}}$ is number of lattice sites which that position is equidistant to (i.e., in 3 dimensions, 2 on a face, 3 or more on an edge, etc.). By definition, the tiling of this function over the lattice sites forms a partition of unity and by consequence, the volume of those cells is $\int \chi(\mathbf{x})d\mathbf{x} = |\mathbf{R}|$. We define the functions $\mathfrak{F}_m$ as

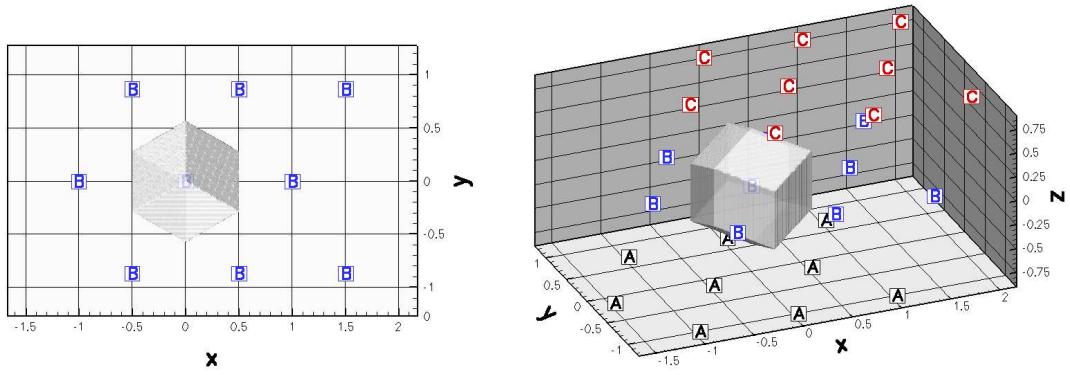

(a) Hexagonal (b) FCC

Figure 2.4: The hexagonal and face-centered cubic lattices and their Voronoi cells

$$\mathfrak{F}_0 = \chi(\mathbf{x}) \tag{2.13}$$

$$\mathfrak{F}_m = \mathfrak{F}_{m-1} * \mathfrak{F}_0 / \int \mathfrak{F}_0 dx \tag{2.14}$$

where we introduced the following notation for the convolution

$$(f * g)(\mathbf{x}) = \int f(\boldsymbol{\xi} - \mathbf{x})\, g(\boldsymbol{\xi})\, d\boldsymbol{\xi}\,.$$

One sees that all the $\mathfrak{F}_\mathfrak{m}$'s will too form a partition of unity. Interestingly enough, the functions for $m \geq 1$ show second order accuracy. The Fourier transform of $\mathfrak{F}_0$ is a sinc function (see Van De Ville et al., 2004, II.B); it vanishes at the dual lattice sites except the origin, $\hat{\mathfrak{F}}_0\left(2\pi\hat{\mathbf{R}}\mathbf{n}\right) = |\det(\mathbf{R})|\,\delta_\mathbf{n}$. $\hat{\mathfrak{F}}_1$ and its successors will therefore present the second order roots at the lattice sites necessary for second order interpolation.

An analytical construction scheme is described in Van De Ville et al. (2004) for the hexagonal lattice but it serves a purpose different from ours. It builds increasingly smooth splines with a growing support whereas we are more interested in increasing the order of the redistribution (Eq. 2.5) and in keeping the support small, thus preventing the creation of too many new elements.

Compact High-Order Schemes

The nature of the FCC and hexagonal lattices allows the design of simple second order schemes, represented by a piecewise linear function. In 2D, this yields the simple scheme represented in Fig. 2.5(a). In the three-dimensional case, the interpolation construction is a bit more tedious. To keep the scheme compact and follow the hexagonal lattice example, we need to consider redistribution inside the tetrahedrons and the octahedrons that constitute the face-centered cubic lattice. In a tetrahedron, the function is linear. Inside a octahedron, the function is built piecewise linear to be isotropic, second order, and remain continuous across these different regions.

These schemes (given in Appendix A) are arguably the most compact second order schemes. The hexagonal scheme redistributes onto three points. Three degrees of freedom are needed to conserve the first two moments. In three dimensions, the FCC scheme redistributes onto four or six points when four degrees of freedom are needed. With their small support, good conservation properties, and relatively simple analytical expressions, they constitute an interesting starting point to build smoother and higher order interpolations.

As a first step following the method described above for the splines, we take the convolution of these simple schemes by themselves and obtain C^2 schemes (Fig. 2.5(b)). In doing so, we increase the support of our interpolation.

The second step consists of increasing the order. In the fashion of Monaghan (1985), we use the ansatz:

$$\tilde{W}(\mathbf{x}) = AW + B\,\mathbf{x}\cdot\nabla W\,. \tag{2.15}$$

The generalization of this result to several dimensions and any type of lattice will be facilitated in Fourier space. Let us assume that the Fourier transform $\hat{W}$ has, as described in theorem 1, a zero of order m at the origin and zeros of order $p \geq m+2$ at the sites of the dual lattice. An example of such a function is the second order C^2 hexagonal function, for which $m = 2$ and $p = 4$ (Fig. 2.6). We can use this m-order

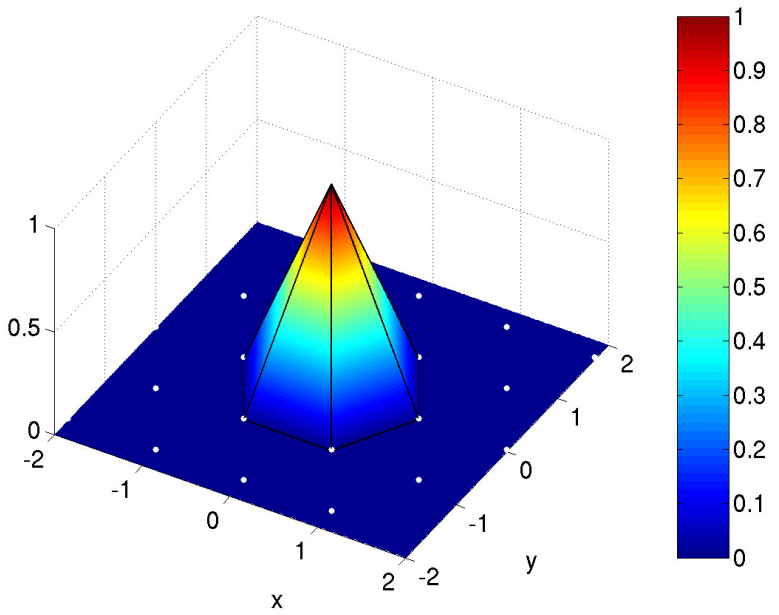

(a) C^0

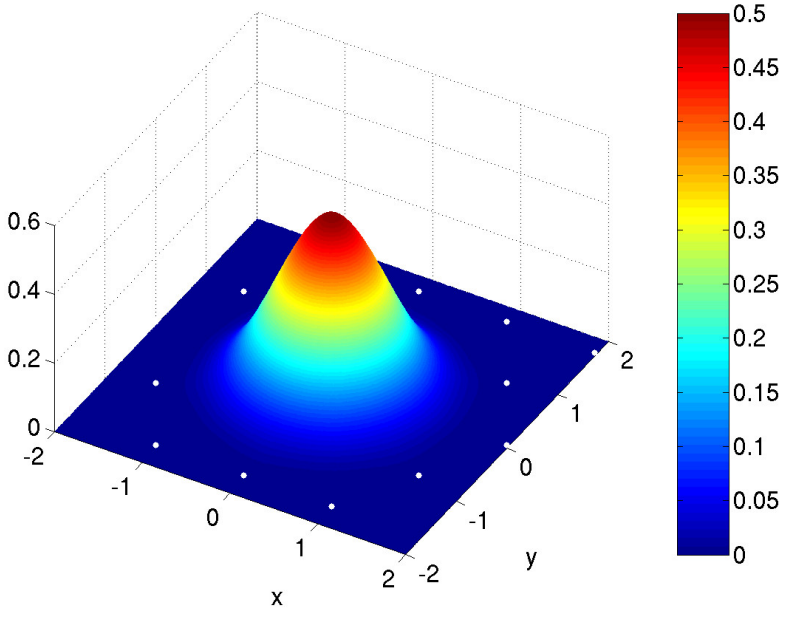

(b) C^2

Figure 2.5: Second order hexagonal schemes

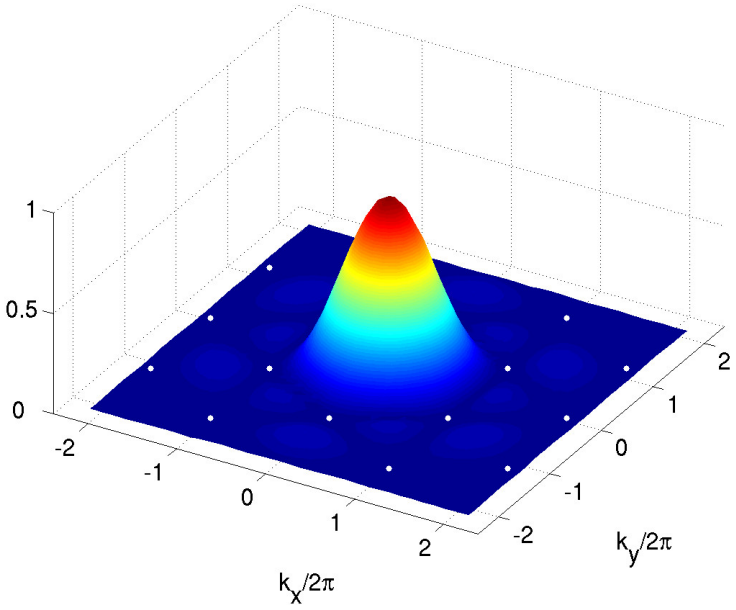

(a) C^0

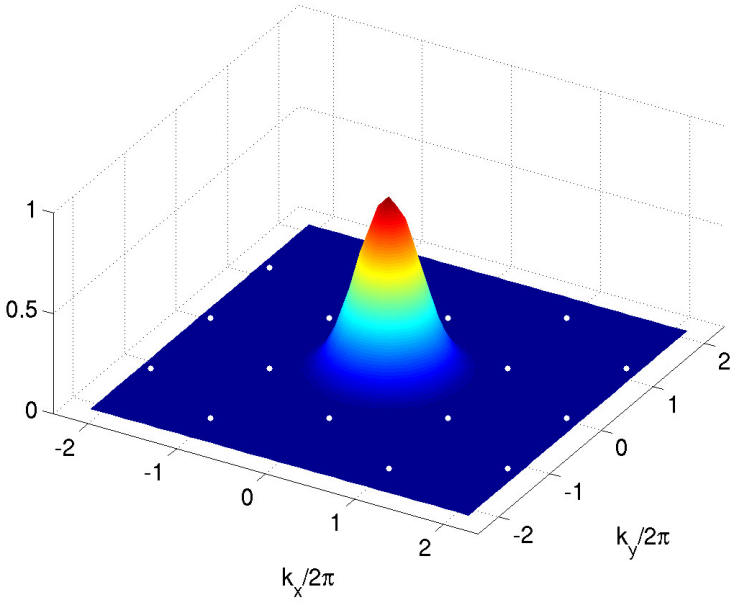

(b) C^2

Figure 2.6: Fourier transforms of the second order hexagonal schemes

scheme to build a $(m+1)$-order scheme:

$$\tilde{W}(\mathbf{x}) = (1+\frac{n}{m})W + \frac{1}{m}\,\mathbf{x}\cdot\nabla W\,. \tag{2.16}$$

Proof. Let us consider the Fourier transform of $\tilde{W}$,

$$\begin{aligned}
\hat{\tilde{W}} &= \mathcal{F}\left(AW + B\,\mathbf{x}\cdot\nabla W\right)\\
&= A\hat{W} + B\,(i\nabla)\cdot\left(i\mathbf{k}\hat{W}\right)\\
&= A\hat{W} - B\,(\nabla\cdot\mathbf{k})\,\hat{W} - B\mathbf{k}\cdot\nabla\hat{W}\\
&= (A-nB)\,\hat{W} - B\mathbf{k}\cdot\nabla\hat{W}
\end{aligned} \tag{2.17}$$

where $n = \nabla\cdot\mathbf{k}$ is the number of dimensions.

We will now solve for A and B to meet condition 2.7. $\hat{W} - |\mathbf{R}|$ and $\mathbf{k}\cdot\nabla\hat{W}$ both have a zero of order m at zero. In order to have $\hat{\tilde{W}}(0) = |\mathbf{R}|$, we need to impose

$$A - nB = 1\,. \tag{2.18}$$

We can increase the order of that root. Developing Eq. 2.17 about 0, we get

$$\begin{aligned}
\hat{\tilde{W}}(\mathbf{k}) &= |\mathbf{R}| + (-1)^m\frac{\mathbf{M}_{\boldsymbol{\nu}}}{m!}\mathbf{k}^{\boldsymbol{\nu}} - B\,\mathbf{k}\cdot\nabla\left((-1)^m\frac{\mathbf{M}_{\boldsymbol{\nu}}}{m!}\mathbf{k}^{\boldsymbol{\nu}}\right) + \mathcal{O}\left(\mathbf{k}^{m+1}\right)\\
&= |\mathbf{R}| + (-1)^m\frac{\mathbf{M}_{\boldsymbol{\nu}}}{m!}\mathbf{k}^{\boldsymbol{\nu}} - B\,(-1)^m\frac{\mathbf{M}_{\boldsymbol{\nu}}}{(m-1)!}\mathbf{k}^{\boldsymbol{\nu}} + \mathcal{O}\left(\mathbf{k}^{m+1}\right)
\end{aligned} \tag{2.19}$$

where $\boldsymbol{\nu}$ is a m-tuple, $1 < \nu_i < n$, $\mathbf{k}^{\boldsymbol{\nu}} = k_{\nu_1}k_{\nu_2}...k_{\nu_p}$, and summation over ν_i is implied. The symmetry of the mth derivatives tensor was also used. If one chooses $B = 1/m$, the extremum at zero will be of order $m+1$.

Finally, the condition 2.8 will be satisfied as well because the term, $-B\mathbf{k}\cdot\nabla\hat{W}$ still has zeros of order $p-1 \geq m+1$ at all the dual lattice sites $\hat{\mathbf{R}}\mathbf{n}$. □

Using this result for the second order C^2 functions for the hexagonal and FCC lattices, we obtain the schemes shown in Fig. 2.7(a) and Fig. 2.8(a). We see that along with a more compact support (12 and 40 points, respectively), the Hex and FCC

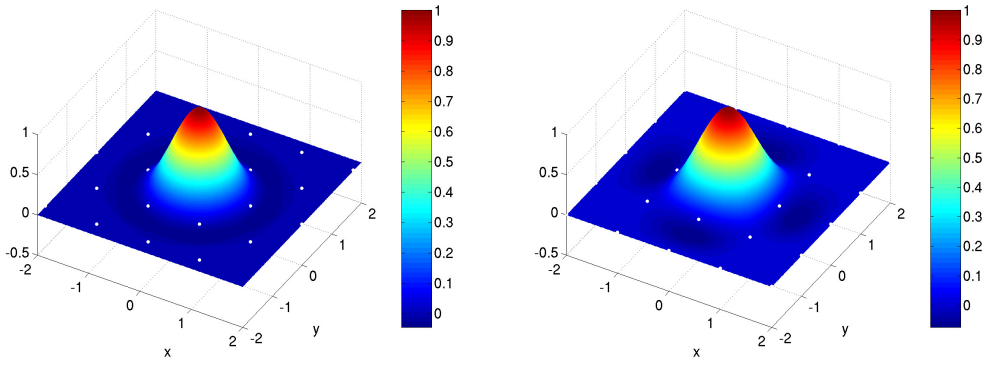

(a) H'_3 (b) M'_4

Figure 2.7: Third order schemes in the Hexagonal (H'_3) and cubic (M'_4) lattices

schemes show better isotropy than their counterparts on a cubic lattice (Fig. 2.7(b) and Fig. 2.8(b)) built from the tensor product of 1D schemes.

It is interesting to realize that this order improvement could also be applied to a second order scheme in a cubic lattice. This will obviously yield a scheme different from a tensor product of third order schemes. Let us consider the M'_4 scheme in two dimensions. Built from the tensor product of one-dimensional schemes, it is

$$M'_4(x,y) = \left(\frac{3}{2}M_4(x) + \frac{1}{2}x\frac{dM_4}{dx}(x)\right)\left(\frac{3}{2}M_4(y) + \frac{1}{2}y\frac{dM_4}{dy}(y)\right).$$

Now applying the above construction in 2D to the scheme $M_4(x,y)$, we get

$$\begin{aligned} M'_{4\,iso}(x,y) &= 2M_4(x)M_4(y) + \frac{1}{2}(x,y)\cdot\nabla\left(M_4(x)M_4(y)\right) \\ &= M'_4(x,y) - (M'_4(x) - M_4(x))(M'_4(y) - M_4(y)). \end{aligned} \tag{2.20}$$

This scheme has the same order and level of continuity as the regular M'_4, but as shown in Fig. 2.9, the lobes so characteristic of the tensor product have disappeared. One inconvenience though is the behavior of the scheme at the origin. The scheme does not reach the unit value, $M'_{4\,iso}(0,0) = \frac{8}{9}$. This is also true to a lesser degree for

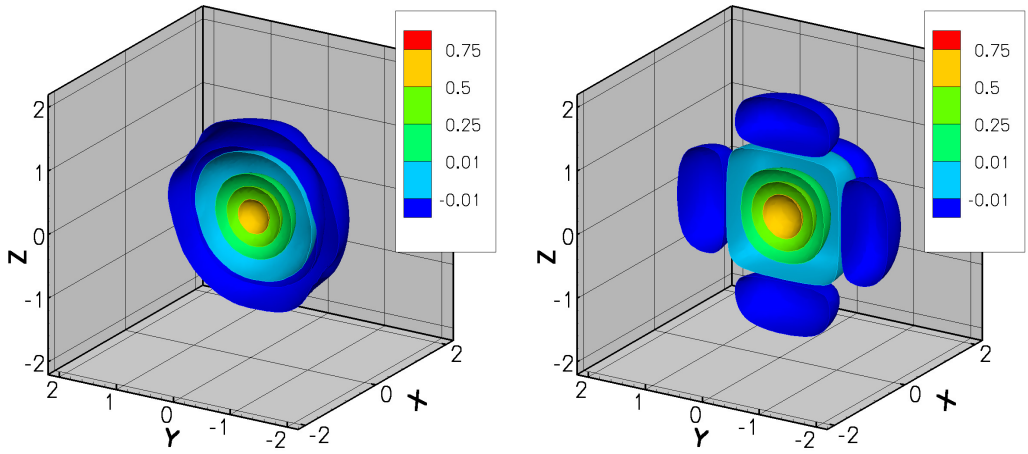

(a) F_3' (b) M_4'

Figure 2.8: Third order schemes in the FCC (F_3') and cubic (M_4') lattices

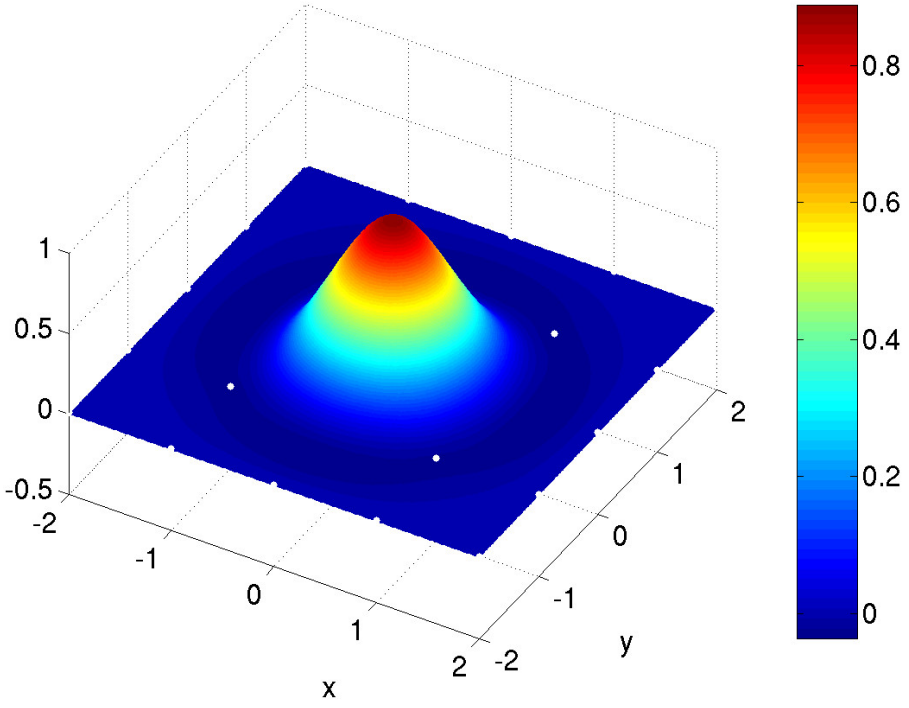

Figure 2.9: Isotropic third order scheme in the cubic lattice $M_{4\,iso}'$

the third order FCC scheme, F_3'. The value at 0 is 0.95. The third order hexagonal scheme does reach 1.

These two schemes therefore redistribute a particle already at a lattice site onto several sites, creating a slightly weaker particle surrounded by weak particles with positive and negative weights.

2.4 Applications

2.4.1 Implementation

While the hexagonal functions could all be derived analytically, the high order FCC functions had to be computed. The convolution of the C^0 scheme by itself and the gradient of Eq. 2.16 were computed in Fourier space. We then switched back to physical space to generate a look-up table.

2.4.2 Test Cases

Our test consists in two colliding vortex rings. This configuration deforms the set of particles and thus tests the quality of the core overlap through the simulation. There are two sets of results. The first one is a well resolved case at $Re = 250$ where we compare two second order schemes: the Λ_1 in the cubic lattice and our FCC_1 scheme. The second set of results is at $Re = 500$ with a coarser resolution (thus under-resolved) and we consider the two second order schemes along with a third order scheme, M_4'. The redistribution frequency (once every ten time steps) was the same in all of our tests.

$Re = 250$

Because of the different lattices used, we define the grid Reynolds number as $Re_h = \frac{UV_p^{1/3}}{\nu}$. It will depend on the actual density of points. The results in this section were obtained at $Re_h \approx 12 \rightarrow 4$. The FCC lattice introduces fewer points than the Λ_1

scheme and shows the same divergence error (Fig. 2.10). The error decreases for $t > 6$ as the rings are decaying.

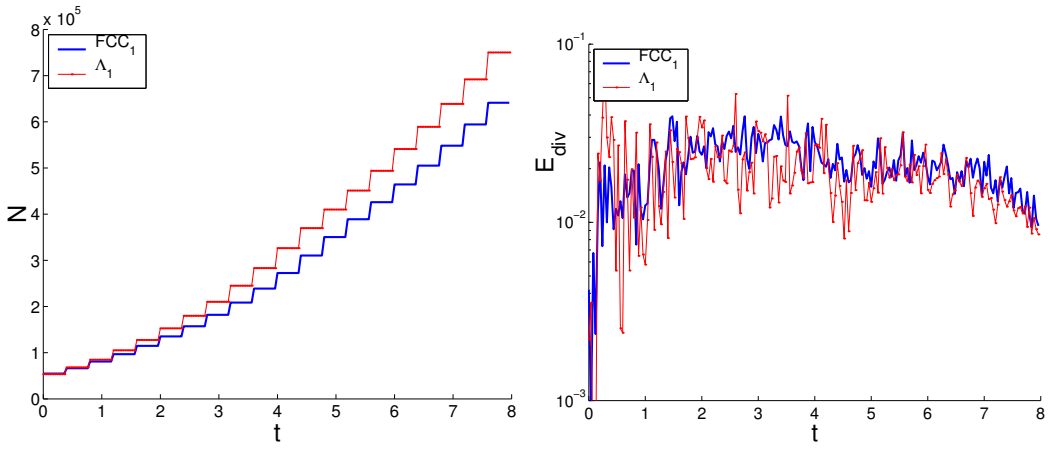

(a) Number of particles

(b) Field error

Figure 2.10: Colliding rings at $Re = 250$

$Re = 500$

We now consider the under-resolved case, $Re_h \approx 27 \rightarrow 13$. One can now notice a significant difference between the two second order schemes. The error for the FCC_1 scheme stays at the level of the M_4' which introduces far more particles because of its wider stencil (Fig. 2.11).

2.5 Conclusions

We have introduced the first representatives of a new family of interpolation schemes based on the face-centered cubic lattice. Our schemes have two outstanding features:

1. Thanks to the many symmetries of the FCC lattice, they are more compact than the equivalent schemes in a cubic lattice. This results in a slower growth of the number of particles because of a tighter *halo* of new particles around the

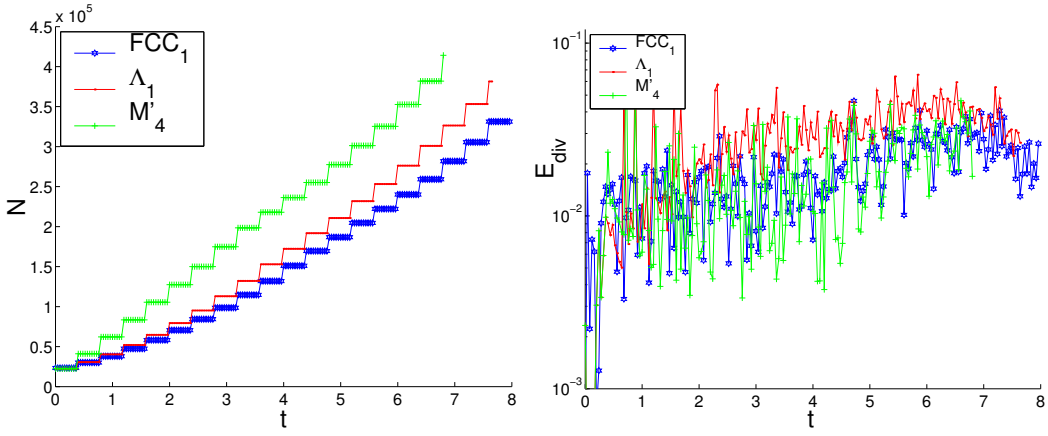

(a) Number of particles

(b) Field error

Figure 2.11: Colliding rings at $Re = 500$

set of old particles. At the end of our runs, the number of elements for the FCC lattice was found to be $\sim 15\%$ lower than in the case of the equivalent cubic scheme (Λ_1).

2. Symmetry is also beneficial to the overlap of the particle cores and allows for better communication between the particles, even under stretching. We have observed a significant reduction in the divergence error for high Re_h cases.

Chapter 3

Reconnection of Vortex Rings

3.1 Introduction

In flow phenomena as diverse as quantum (Kivotides et al., 2002), magnetic (Christensson and Hindmarsh, 1999), and incompressible (Leonard, 1985) fluids, it is useful to study the physics of turbulence by modeling the system as a collection of tubular flux loops which in the case of vortical fields are called vortex filaments. An intrinsic property of such highly structured systems is their ability to dynamically change their topology via reconnection mechanisms. Does this change in topology affect in turn properties of fluid turbulence like intermittency and scalar-mixing (which depend directly on the structure of the flow) or the dynamics of energy in wavenumber space? Or is it the case that reconnection events are not generic and thus, have no direct impact on the mean properties of turbulent flows? The aim of this chapter is to address these issues by fully resolving the Navier-Stokes dynamics of interacting vortex rings for three simple geometries having great potential for illuminating the physics of reconnection. Although the flows considered are not strictly turbulent, the hope is that in a future structural approach to the problem of turbulence, a significant part of the flow complexity could be traced back to the physics of similar vortex interactions.

Incompressible vortex reconnections have an extensive bibliography (for a review of the work up to 1994, see Kida and Takaoka (1994) and Kerr and Hussain (1989)). In Pelz (1997), Shelley et al. (1993) and Pumir and Kerr (1987), reconnections of vortex tubes were considered with an emphasis on the possibility of singularity formation as $Re \to \infty$. In Winckelmans (1995), the strong interactions between vortex rings were computed with the interest in developing numerical methods and turbulence models rather than in focusing on the physics of reconnection. In Aref and Zawadzki (1991), it is discussed how a linked vortex configuration could be achieved starting from an unlinked initial state, and in Zawadzki and Aref (1991), it is considered how the mixing of a non-diffusing passive scalar is affected during vortex ring collision. The reconnection of two approaching (but not colliding) vortex rings was studied experimentally in Schatzle (1987) and theoretically in Ashurst and Meiron (1987). This chapter extends these studies by considering generic vortex configurations and by capturing more features of vortex reconnections in a turbulent flow.

3.2 Method

We solve the Navier-Stokes equations for an unbounded three-dimensional incompressible viscous flow. We employ the vortex element method introduced in Chapter 1, along with the face-centered cubic redistributions discussed in Chapter 2.

3.2.1 Diagnostics

We calculate the global kinetic energy E and enstrophy Ω defined as

$$E = \frac{1}{2}\int \boldsymbol{u}\cdot\boldsymbol{u}\, d\boldsymbol{x}\,, \tag{3.1}$$

$$\Omega = \int \boldsymbol{\omega}\cdot\boldsymbol{\omega}\, d\boldsymbol{x}\,. \tag{3.2}$$

For unbounded flows, the relation between kinetic energy and enstrophy is

$$\frac{d}{dt}E = -\nu\Omega\,. \tag{3.3}$$

3.2.2 Spectrum

We also compute the evolution of the spectrum of the kinetic energy $E(k)$ which, in terms of the Fourier transform of vorticity

$$\hat{\boldsymbol{\omega}} = \frac{1}{(2\pi)^{3/2}} \int \boldsymbol{\omega}(\boldsymbol{r})\, e^{-i\,\boldsymbol{r}\cdot\boldsymbol{k}}\, d\boldsymbol{r}\ , \tag{3.4}$$

is defined as

$$E(k) = \frac{1}{2}(2\pi)^3 \int_{|\boldsymbol{k}|=k} \hat{\boldsymbol{\omega}} \cdot \hat{\boldsymbol{\omega}}^*\, d\Omega_k\ , \tag{3.5}$$

where $d\Omega_k$ denotes $\sin\theta_k\, d\theta_k\, d\phi_k$, the solid angle element in spherical coordinates. The calculation of the spectrum requires a double summation over the vortex elements which results to $\mathcal{O}(N^2)$ complexity. Because of this, the calculation of the spectrum is much more costly than the solution of the Biot-Savart law. Since the number of particles grows substantially during our simulations, from around $N = 5\,10^4$ at $t = 0$ to $8\,10^5$ in the end, our computational resources did not allow us to compute the spectra for all times. The details of the derivation and implementation are given in Appendix B.

3.3 Results

3.3.1 Configuration

All calculations were done with the same Reynolds number: $Re = \frac{\Gamma}{\nu} = 250$, where Γ is the circulation of one ring and ν is the kinematic viscosity. This small value of Re was dictated by the computational cost and the need for well-resolved reconnection regions. All the rings have the same initial Γ. All of our conclusions are conditioned upon the relatively small value of Re, as well as on the common initial circulation and should not be extrapolated uncritically to other settings. The initial vorticity distribution in the cross-section of every ring is Gaussian with a cutoff

$$\omega_\theta = \frac{\Gamma}{2\pi\sigma^2} e^{\frac{-r^2}{2\sigma^2}} \tag{3.6}$$

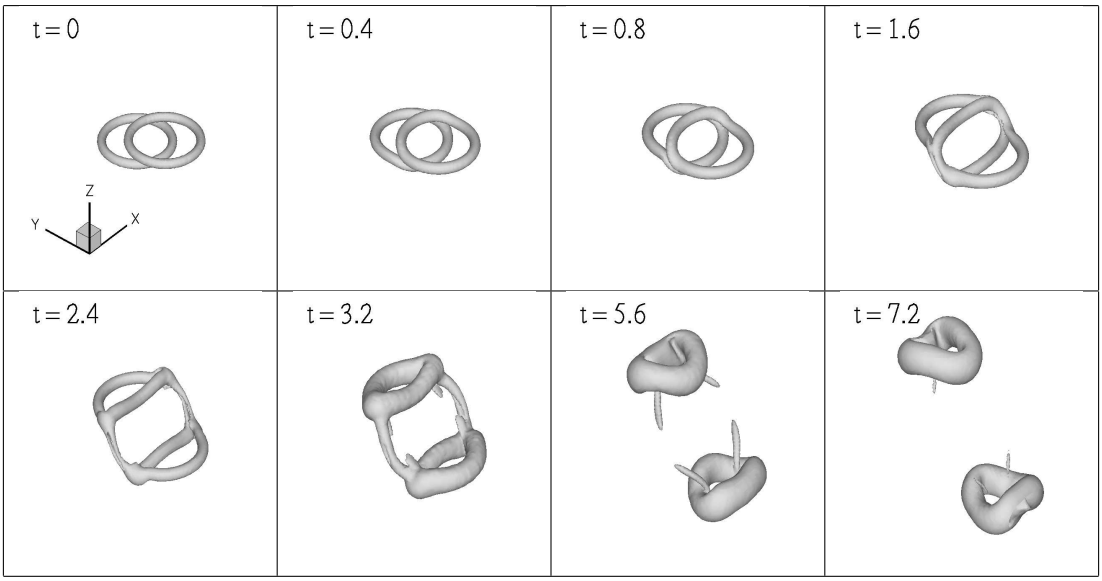

Figure 3.1: Vortex rings in an offset collision: contours of vorticity (from $t = 0$ to 2.4, the contour is $\omega = 0.15\,\omega_{\rm max}^{\rm t=0}$; for $t > 2.4$, it is $\omega = 0.025\,\omega_{\rm max}^{\rm t=0}$)

where r is the distance to the core center, σ is the core radius, and ω_θ is the azimuthal vorticity. We chose $\sigma = 0.05\,R$ (where R is the radius of the ring) to ensure that the rings are still thin when reconnections occur. Our results were made dimensionless in the following manner: $t = \frac{\Gamma\,t'}{R^2}$, $x = \frac{x'}{R}$, $\omega = \frac{R^2\,\omega'}{\Gamma}$ where t', x', ω' are dimensional.

We studied three configurations. In the first case (Fig. 3.1), the initial rings are placed at a distance of $R/4$ apart in the z direction, offset by R along the y axis and they move in opposite directions along the z axis.

In the second case (Fig. 3.2), two rings of different radii (R and $R/2$) and of initial separation $R/4$ are moving in the same direction along the z axis, with the center of the small ring on a collision course with the circumference of the large one. The small ring has a larger self-induced velocity and catches up with the large ring.

Finally, in the third case (Fig. 3.3), the two rings are linked at 90^o, a ring going through the other in its center. One is moving in the positive z direction, the other in the positive y direction.

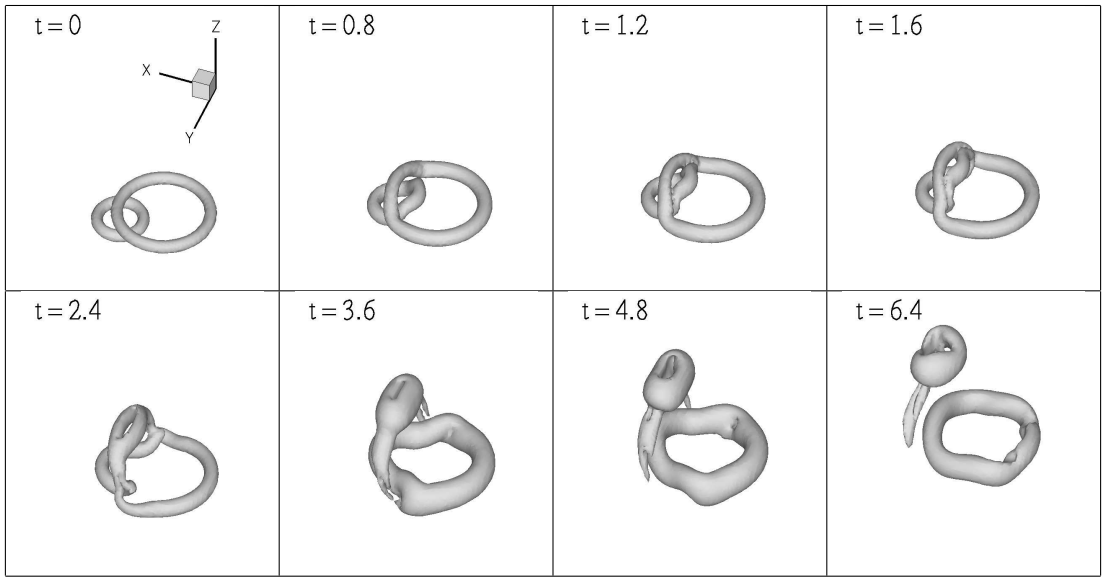

Figure 3.2: Vortex rings of different radii: contours of vorticity (from $t = 0$ to 2.4, the contour is $\omega = 0.15\,\omega_{\rm max}^{\rm t=0}$; for $t > 2.4$, it is $\omega = 0.05\,\omega_{\rm max}^{\rm t=0}$)

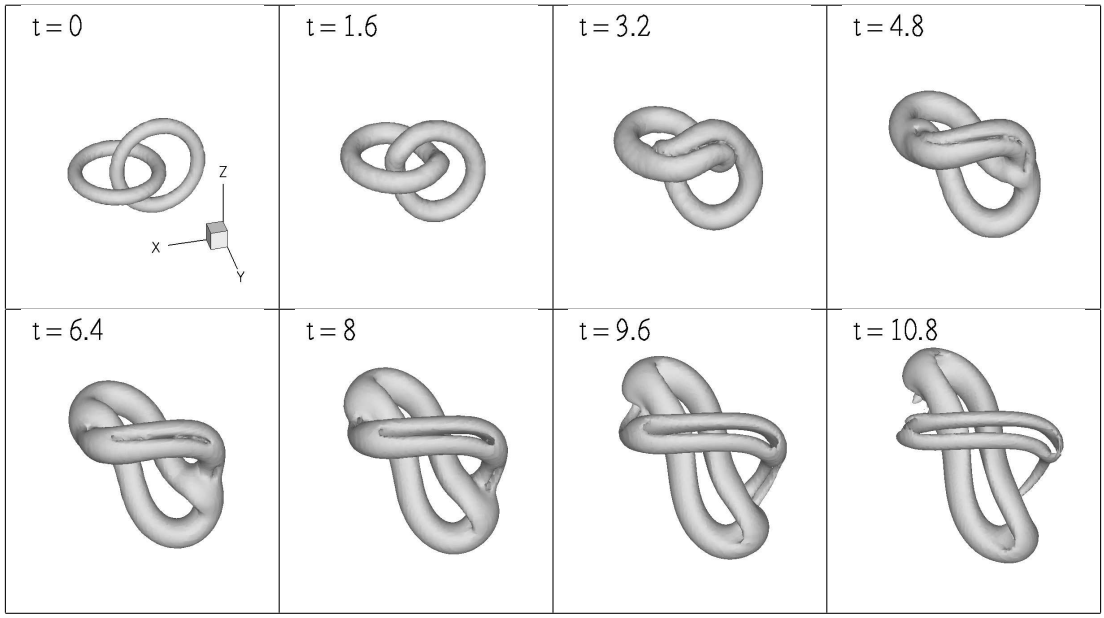

Figure 3.3: Linked vortex rings: contours of vorticity; $\omega = 0.025\,\omega_{\rm max}^{\rm t=0}$

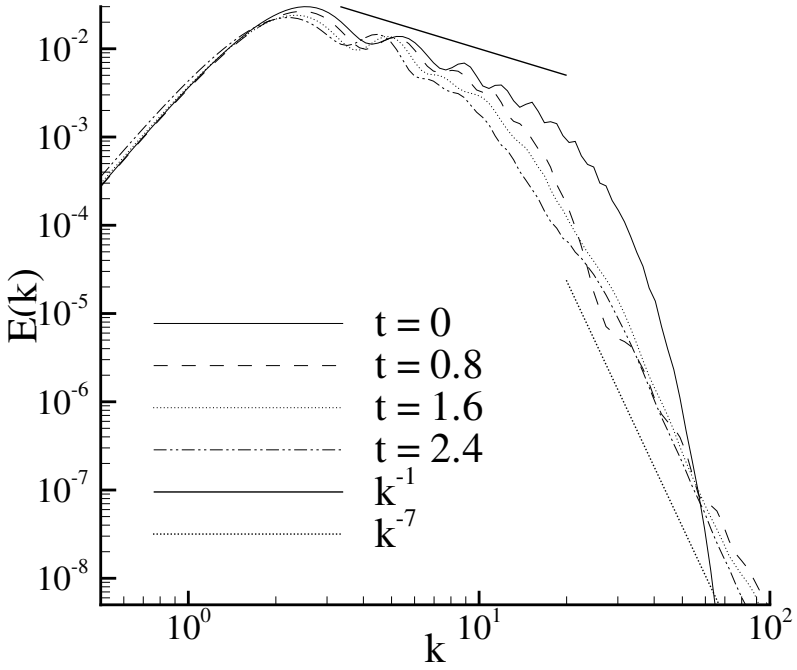

Figure 3.4: Vortex rings in an offset collision: evolution of the energy spectrum

3.3.2 Discussion

All three evolutions lead to ring reconnection (Figs. 3.1, 3.2 and 3.3) and have common features. The latter will be discussed here in the context of the first configuration, observing that the phenomena are the same for the other two cases. The spectrum at $t = 0$ (Fig.3.4) has the characteristic oscillations of the spectrum of isolated vortex rings and a cutoff at the scale of ring core radius $\sigma = 0.05$, $k = 20$. Our results (Figs. 3.1 and 3.5) suggest that the reconnection starts approximately around $t = 0.6$ and ends around $t = 1.75$ with a duration $\Delta t_r = 1.15$. Specifically, as the rings approach each other, they stretch and deform near the collision points so that their respective vorticities become locally anti-parallel. The two ends of this stretching region eventually become reconnection kinks where in the absence of singularities, the strong vorticity gradients are smoothed out by diffusion. This is also seen in the graphs of the global quantities (Fig. 3.5) where the beginning of the reconnection process corresponds to a hump in the graph of Ω and to a steepening of the slope

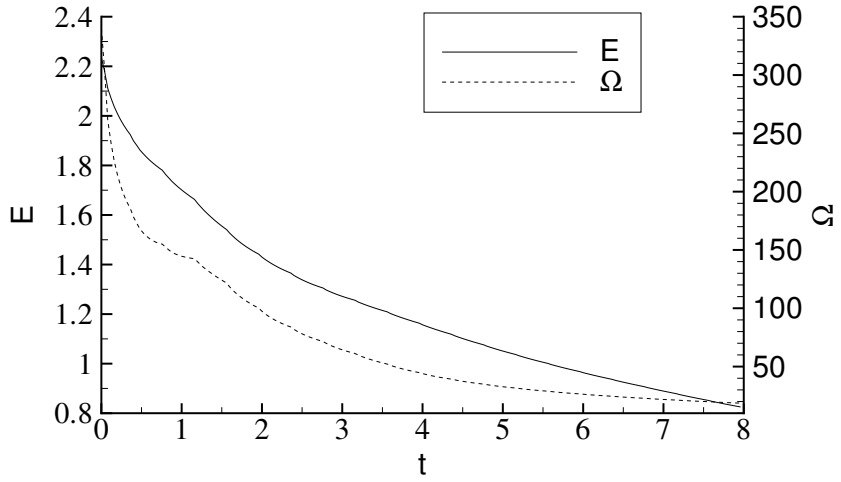

Figure 3.5: Vortex rings in an offset collision: kinetic energy and enstrophy

of $E(t)$ between $t = 0.6$ and $t = 1.4$. Our calculation predicts that the filament core radius increases from the initial value $\sigma_0 = 0.05R$ to the value at reconnection $\sigma_r = 0.12R$ due to diffusion. Using this latter value, we calculate the viscous time scale $t_v = \sigma_r^2/\nu = 0.36$. Scaling the convective ring velocity with $\Gamma/4\pi R$, we estimate the time needed for a ring to traverse σ_r: $t_c = 4\pi R\sigma_r/\Gamma = 1.5$. These times are of the same order as Δt_r; this indicates that both viscous and convective phenomena participate in the reconnection physics. The relative magnitudes of t_v and Δt_r are different from the ones in Schatzle (1987) where the Reynolds number was 1600 and the viscous time scale was therefore much larger than the duration of reconnection.

After some time (Fig. 3.6), we can say that two new rings are formed. The pairs of filaments between the reconnection regions are stretched further as the new rings move apart from each other ($t = 1.6$ to 5.6). These stretched vorticity structures are responsible for a continued transfer of energy to the smallest scales until these structures are dissipated away. This conclusion is supported by the results displayed in Fig. 3.4. The initial exponential cutoff of the spectrum gives way to a non-exponential region (although it still remains very steep) for $t \geq 0.8$. The spectrum still has an exponential cutoff that lies outside the range of Fig. 3.4; this cutoff corresponds to scales close to the particle core size. Between $t = 0.8$ and 2.4 there is a significant

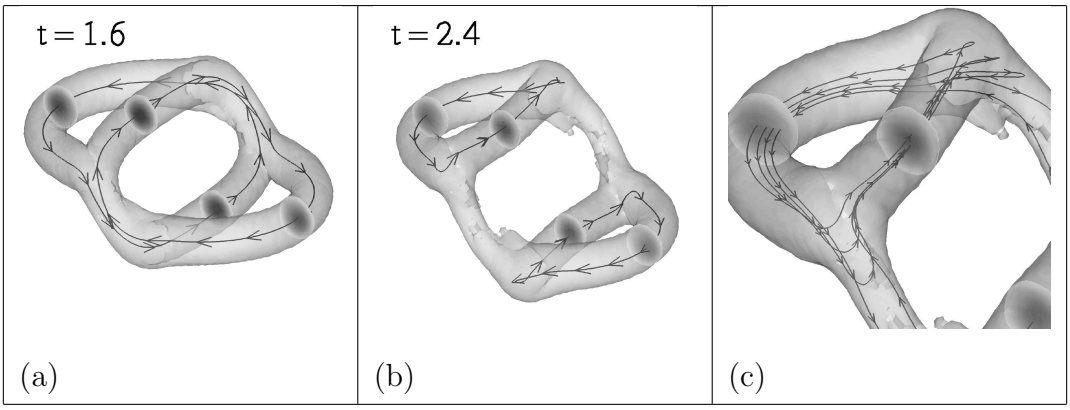

Figure 3.6: Vortex rings in an offset collision: contour of vorticity and vortex lines at $t = 1.6$ and 2.4; the transparent contour is $\omega = 0.025\,\omega_{\max}^{t=0}$; the vortex lines in (a) and (b) were chosen to pass through the vortex core center (the maximum value of ω) at a location away from the reconnection kinks; in (c), a few neighboring lines are also shown for $t = 2.4$

decay of the energy spectrum for $k < 20$, but little change for $k > 20$. This last observation indicates that in the small scales of motion, an approximate balance between energy transfer from large scales due to stretching and local energy dissipation due to diffusion is temporarily attained. This conclusion is also consistent with the vorticity structure shown in Fig. 3.7 where it is observed that between $t = 0.8$ and $t = 2.4$ (the time of the last spectrum calculation), the vorticity magnitude in the secondary structures (where the global maximum of vorticity resides) stops increasing and in fact it decays slightly.

It is conceivable that for Re numbers higher than 250, an intermediate scaling range that is in between the k^{-1} and k^{-7} regimes could appear with inertial type of scaling. It is also expected that with increasing Re number, the hump observed in the global enstrophy during the reconnection could become more pronounced and (according to the previous discussion) shorter in duration.

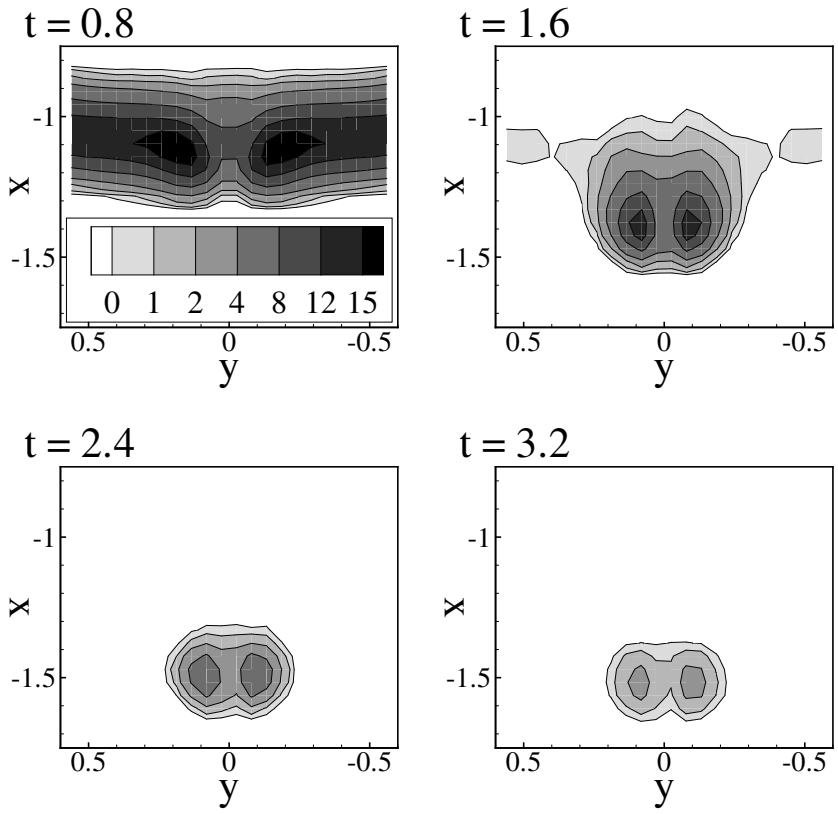

Figure 3.7: Vortex rings in an offset collision: contours of vorticity magnitude in the plane $z = 0$ from $t = 0.8$ to 3.2

3.4 Conclusions

In conclusion, we studied three generic vortex ring configurations and we found that in all cases, the rings reconnect. This suggests that reconnection is a common phenomenon in vortex filament encounters and perhaps also in turbulent flows. In addition, we observe an intensification of dissipation which is local in time and could be a mechanism contributing to turbulence intermittency.

A by-product of reconnection is the formation of stretched structures with anti-parallel vorticity which transfer energy to the smallest scales where it is rapidly dissipated. Without this energy redistribution in wavenumber space, the decay of global kinetic energy would have been slower. This important effect depends directly on the details of the initial vortex configuration (compare with experiments in Schatzle (1987)). The observed intensification of small scale motions hints to an enhancement of small scale mixing of passive scalars with $Sc \geq 1$.

The excited Kelvin waves represent a fast mechanism for energy transfer, but the small Re number of our calculations is not suitable for understanding their full importance. In particular, they are confined to low wavenumbers in opposition to the Kelvin waves observed in reconnections in quantum fluids (Kivotides et al., 2001). This is because quantum filaments are inviscid and have a very thin core ($\sigma \sim 0.1\, nm$) so that high wavenumber Kelvin waves propagate without damping even for rings with small circulation.

Besides illuminating important physics, the present work will guide future introduction of phenomenological reconnection models into vortex filament computational methods. In this way, the applicability of the latter methods will be extended to flows with complex vorticity configurations.

Chapter 4

Flows Around Rotating and Deforming Boundaries

4.1 Introduction

The Lagrangian nature of the Vortex element method makes it quite appealing for external flows around complex and evolving geometries. The applications are numerous. An obvious one is the family of biological flows which cover a wide range of Reynolds numbers, with insect flight in the medium range of $Re \simeq 100 \rightarrow 300$. This chapter focuses on the additional steps needed in the framework of vortex methods to account for the rotation or deformation of the boundaries. We cover some fundamentals and existence results in Section 4.2; we then study the Biot-Savart boundary terms in Section 4.3. In Section 4.4, we consider the boundary conditions on vorticity. Finally, we discuss the conservation of global quantities for such flows in Section 4.5.

4.2 Kinematics

In a first step, let us consider the flow exterior to a set of bodies $\Omega_i(t)$, i.e. $\mathbb{R}^3 \backslash \cup \{\Omega_i(t)\}$ as our flow domain. We consider the usual Helmholtz decomposition of the velocity

field,

$$\begin{aligned} \mathbf{u} &= \mathbf{u}_{\boldsymbol{\omega}} + \mathbf{u}_{\phi} && (4.1) \\ &= \nabla \times \boldsymbol{\psi} + \nabla\phi && (4.2) \end{aligned}$$

where we fix the gauge of $\boldsymbol{\psi}$ as $\nabla \cdot \boldsymbol{\psi} = 0$. We restrict ourselves to the case of incompressible flows. We therefore have

$$\begin{aligned} \nabla^2\boldsymbol{\psi} &= -\nabla \times \mathbf{u} = -\boldsymbol{\omega}\,, && (4.3) \\ \nabla^2\phi &= 0\,. && (4.4) \end{aligned}$$

Boundary conditions have to be imposed on the velocity field with the no-slip condition at the solid boundaries

$$\mathbf{u}(\mathbf{x})|_{\mathbf{x}\in\partial\Omega_i(t)} = \mathbf{u}|_{\partial\Omega_i(t)} \tag{4.5}$$

and possibly a free-stream velocity

$$\mathbf{u}|_{\mathbf{x}\to\infty} = \mathbf{u}_{\infty}\,. \tag{4.6}$$

4.2.1 Extended Domain and Fields

The development of field computations and boundary conditions can quickly become tedious if one considers the domain $\mathbb{R}^3 \setminus \cup\{\Omega_i(t)\}$. The extension of the fields to $\mathbb{R}^3$ facilitates our work, even more so in the case of deforming boundaries. More explicitly, we consider the extensions of $\boldsymbol{\psi}$, $\boldsymbol{\omega}$ and $\mathbf{u}$ to $\mathbb{R}^3$. The extended velocity field may therefore have some divergence inside the immersed bodies since general deformations may involve some dilatation.

If we make the required assumptions about the regularity of the velocity field, we can apply Poincaré's formula (Brard (1973) and Cottet and Koumoutsakos (2000))

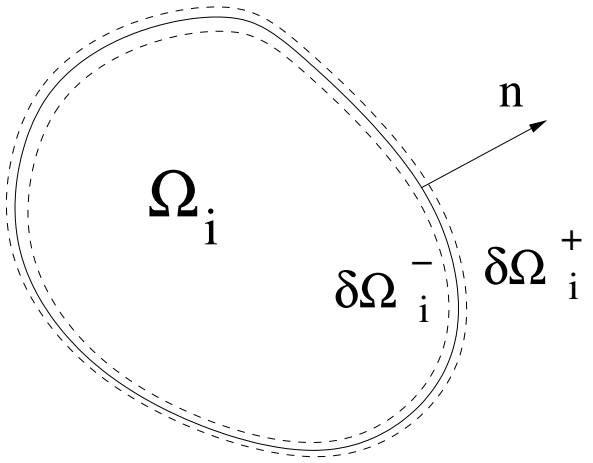

Figure 4.1: Boundaries and sign convention

inside Ω_i

$$\begin{aligned}
&\nabla \times \left(\int_{\partial\Omega_i^-} G\left(\mathbf{x}-\mathbf{x}'\right)\left(-\mathbf{n}\times\mathbf{u}^-(\mathbf{x}')\right) dS + \int_{\Omega_i} G\left(\mathbf{x}-\mathbf{x}'\right)\boldsymbol{\omega}\left(\mathbf{x}'\right) d\mathbf{x}' \right) + \\
&\nabla \left(\int_{\partial\Omega_i^-} -G\left(\mathbf{x}-\mathbf{x}'\right)\left(-\mathbf{n}\cdot\mathbf{u}^-(\mathbf{x}')\right) dS + \int_{\Omega_i} -G\left(\mathbf{x}-\mathbf{x}'\right)\left(\nabla\cdot\mathbf{u}(\mathbf{x}')\right) d\mathbf{x}' \right) \qquad (4.7) \\
&= \begin{cases} \mathbf{u}(\mathbf{x}) & \mathbf{x}\in\Omega_i \\ 0 & \mathbf{x}\in\mathbb{R}^3\setminus\Omega_i \end{cases}
\end{aligned}$$

and outside Ω_i

$$\begin{aligned}
&\nabla \times \left(\int_{\cup\partial\Omega_i^+} G\left(\mathbf{x}-\mathbf{x}'\right)\left(\mathbf{n}\times\mathbf{u}^+(\mathbf{x}')\right) dS + \int_{\mathbb{R}^3\setminus\cup\Omega_i} G\left(\mathbf{x}-\mathbf{x}'\right)\boldsymbol{\omega}\left(\mathbf{x}'\right) d\mathbf{x}' \right) + \\
&\nabla \left(\int_{\cup\partial\Omega_i^+} -G\left(\mathbf{x}-\mathbf{x}'\right)\left(\mathbf{n}\cdot\mathbf{u}^+(\mathbf{x}')\right) dS + \int_{\mathbb{R}^3\setminus\cup\Omega_i} -G\left(\mathbf{x}-\mathbf{x}'\right)\underbrace{\left(\nabla\cdot\mathbf{u}(\mathbf{x}')\right)}_{=0} d\mathbf{x}' \right) \qquad (4.8) \\
&= \begin{cases} \mathbf{u}(\mathbf{x}) & \mathbf{x}\in\mathbb{R}^3\setminus\cup\Omega_i \\ 0 & \mathbf{x}\in\cup\Omega_i \end{cases} .
\end{aligned}$$

We assume that there is no through-flow, i.e., $\mathbf{n}\cdot\mathbf{u}^+ = \mathbf{n}\cdot\mathbf{u}^-$. The sum of the two

above equations gives us an expression for the velocity in the extended domain $\mathbb{R}^3$

$$\begin{aligned}\mathbf{u}(\mathbf{x}) = (\mathbf{K}\times) * \boldsymbol{\omega}_{\cup\Omega_i} - \mathbf{K} * \sigma_{\cup\Omega_i} + (\mathbf{K}\times) * \boldsymbol{\omega}_{\mathbb{R}^3\setminus\cup\Omega_i} \\ + \int_{\cup\partial\Omega_i} \mathbf{K}(\mathbf{x}-\mathbf{x}') \times \boldsymbol{\gamma}(\mathbf{x}') dS\,;\end{aligned} \tag{4.9}$$

where $\mathbf{K} = \nabla G$. The different terms on the right-hand side of Eq. 4.9 deserve some attention:

- $\boldsymbol{\omega}_{\cup\Omega_i}$ is the vorticity inside the bodies present in the flow;
- $\sigma_{\cup\Omega_i}$ is the dilatation $\nabla \cdot \mathbf{u}$ inside the bodies;
- $\boldsymbol{\omega}_{\mathbb{R}^3\setminus\cup\Omega_i}$ is the vorticity present in the flow;
- $\boldsymbol{\gamma} = \mathbf{n} \times (\mathbf{u}^+ - \mathbf{u}^-)$ are bound vortex sheets which have to appear in order to enforce the kinematic condition of Eq. 4.5.

For boundaries that move as if they were the boundaries of rigid objects, the first two items can be simplified, the vorticity "inside" the bodies reduces to twice their angular velocities $2\mathbf{W}_i$, and the dilatation is null.

Before proceeding, we introduce the notations $\mathbf{u}_i$, $\boldsymbol{\omega}_i$ and σ_i; these will refer to the known velocity, vorticity and divergence fields inside the deforming object Ω_i, up to and including $\partial\Omega_i^-$.

4.2.2 Boundary Vorticity and Integral Equations

Let us now concentrate on the boundary vorticity term. This term is an unknown that is solved for through the enforcement of the boundary conditions. One can consider either through-flow or slip cancellation at the wall. If we use the latter, we have to consider the limit of the tangential component of Eq. 4.9 for $\mathbf{x} \to \mathbf{x}_{\partial\Omega_i^-}$,

$$\mathbf{u}\cdot\mathbf{t} \to \left(\mathbf{u}_{\text{ext}} - \frac{\boldsymbol{\gamma}\times\mathbf{n}}{2} + \int_{\cup\partial\Omega_i} \mathbf{K}\times\boldsymbol{\gamma}\, dS\right)\cdot\mathbf{t}\,, \tag{4.10}$$

where $\mathbf{u}_{\text{ext}}$ regroups the first three terms of the right-hand side of Eq. 4.9 and the vectors $\mathbf{t}$ lie in the local tangent plane. If we match this value to the tangential wall velocity, we obtain

$$\left(\frac{\boldsymbol{\gamma}\times\mathbf{n}}{2}-\int_{\cup\partial\Omega_i}\mathbf{K}\times\boldsymbol{\gamma}\,dS\right)\cdot\mathbf{t}=(\mathbf{u}_{\text{ext}}-\mathbf{u}_i)\cdot\mathbf{t}\,. \tag{4.11}$$

Well-Posedness

Eq. 4.11 is a Fredholm equation of the second kind which justifies our earlier choice of the no-slip condition; this guarantees well-posedness when we switch to finite dimension spaces for the solution, i.e., we use a panel discretization.

Existence

Brard (1973) considers the existence issue for Eq. 4.11 without the projection into the local tangential plane $(\cdot\mathbf{t})$

$$T\boldsymbol{\gamma}=\left(-\frac{\mathbf{n}\times}{2}-\int_{\cup\partial\Omega_i}\mathbf{K}\times\,dS\right)\boldsymbol{\gamma}=\mathbf{u}_{\text{ext}}-\mathbf{u}_i\,. \tag{4.12}$$

The existence condition requires that the right-hand side be orthogonal to $\ker(T^*)$, which is formed by the functions $\xi(\mathbf{x}')=\text{const}\,\mathbf{n}(\mathbf{x}')$. The condition is then

$$\int_{\cup\partial\Omega_i^-}\mathbf{n}\cdot(\mathbf{u}_{\text{ext}}-\mathbf{u}_i)=0\,; \tag{4.13}$$

By the divergence theorem, we have

$$\int_{\cup\Omega_i}\nabla\cdot(\mathbf{u}_{\text{ext}}-\mathbf{u}_i)=0\,; \tag{4.14}$$

which is satisfied because $\nabla\cdot\mathbf{u}_i=\nabla\cdot\mathbf{u}_{\text{ext}}=\sigma_i$ inside Ω_i.

Because we use the projection above, this existence condition is implicitly imposed. We should however verify that the no through-flow condition will be enforced as well.

We have

$$\begin{aligned} \nabla \times (\mathbf{u} - (\mathbf{K}\times) * \boldsymbol{\omega}_{\Omega_i} + \mathbf{K} * \sigma_{\Omega_i}) &= 0 \\ \nabla \cdot (\mathbf{u} - (\mathbf{K}\times) * \boldsymbol{\omega}_{\Omega_i} + \mathbf{K} * \sigma_{\Omega_i}) &= 0 \end{aligned}$$

for $\mathbf{x} \in \Omega_i$. $(\mathbf{u} - (\mathbf{K}\times) * \boldsymbol{\omega}_{\Omega_i} + \mathbf{K} * \sigma_{\Omega_i})$ can therefore be expressed as the gradient of a harmonic field Φ inside the boundary Ω_i

$$(\mathbf{u} - (\mathbf{K}\times) * \boldsymbol{\omega}_{\Omega_i} + \mathbf{K} * \sigma_{\Omega_i}) = \nabla\Phi \text{ with } \Delta\Phi = 0 \, .$$

Solving Eq. 4.11 thus sets Φ to a constant on $\partial\Omega_i^-$. By the maximum principle, Φ is constant in Ω_i, thus implying that $\mathbf{u} \cdot \mathbf{n} = \partial\Phi/\partial n = 0$.

Uniqueness

Uniqueness issues will appear if the operator on the left-hand side of Eq. 4.11 has a non-trivial kernel. This in turn will depend on the topology of the problem; non-simply-connected $\partial\Omega_i$ will allow non-unique solutions. This is the case for any object in two dimensions and for objects with holes in three dimensions.

For such cases, $\dim(\ker[T])$ additional conditions have to be enforced; they are found by applying Kelvin's circulation theorem to irreducible loops in the domain (Cottet and Koumoutsakos, 2000). For the moment, we will restrict ourselves to simply-connected geometries.

4.3 Boundary Contributions

Eq. 4.9 shows that the velocity used in Eq. 1.9 and 1.10 must include additional contributions from the objects in addition to the usual Biot-Savart terms $(\mathbf{K}\times) * \boldsymbol{\omega}_{\mathbb{R}^3 \setminus \cup\Omega_i}$, and $\int_{\cup\partial\Omega_i} \mathbf{K}(\mathbf{x}-\mathbf{x}') \times \boldsymbol{\gamma}(\mathbf{x}')dS$, if there are bound vortex sheets. We proceed

and call these contributions $\mathbf{u}_b$,

$$\mathbf{u}_b = (\mathbf{K}\times) * \boldsymbol{\omega}_{\cup\Omega_i} - \mathbf{K} * \sigma_{\cup\Omega_i} + (\mathbf{K}\times) * \boldsymbol{\omega}_{\mathbb{R}^3\setminus\cup\Omega_i} \ , \tag{4.15}$$

$\boldsymbol{\psi}_b$ and ϕ_b for the corresponding stream function and potential,

$$\boldsymbol{\psi}_b = G * \boldsymbol{\omega}_{\cup\Omega_i} + G * \boldsymbol{\omega}_{\mathbb{R}^3\setminus\cup\Omega_i} \tag{4.16}$$

$$\phi_b = -G * \sigma_{\cup\Omega_i} \ . \tag{4.17}$$

These terms are volume integrals which may not have a convenient discretization; one might rather have a panel representation of the boundary. In addition, these terms involve quantities that are not known in practical problems. Indeed, let us consider the swimming motion of a fish where the kinematics are imposed. One may not realistically know the velocity field and deformations inside the fish and will only impose the displacement of the skin of the fish. Similarly, from a physical point of view, the details of the deformations inside the objects should not have an influence on the velocity field in the flow. For these reasons, the present section covers methods to transform those volume integrals into surface integrals.

4.3.1 Rigid Objects

In the case of a rigid object, the dilatation sources are null and the vorticity is a constant equal to twice the angular velocity. We start from the stream function:

$$\boldsymbol{\psi}_b(\mathbf{x}) = \sum_i 2\mathbf{W}_i \int_{\Omega_i} G(\mathbf{x}-\mathbf{x}')d\mathbf{x}' \tag{4.18}$$

If we rewrite the Green's function

$$G(\mathbf{u}) = \frac{1}{4\pi}|\mathbf{u}|^{-1} = \frac{1}{4\pi}\nabla\cdot\left(\frac{\mathbf{u}}{2|\mathbf{u}|}\right) \ , \tag{4.19}$$

we obtain, by the divergence theorem

$$\boldsymbol{\psi}_b(\mathbf{x}) = -\sum_i \frac{\mathbf{W}_i}{4\pi} \int_{\partial\Omega_i} \frac{\mathbf{x}-\mathbf{x}'}{|\mathbf{x}-\mathbf{x}'|} \cdot \mathbf{n} dS(\mathbf{x}') \,. \tag{4.20}$$

The velocity field and its gradient can then be obtained by successively taking the curl and the gradient of the above expression:

$$\mathbf{u}_b(\mathbf{x}) = \sum_i \frac{\mathbf{W}_i}{4\pi} \times \int_{\partial\Omega_i} \frac{\mathbf{n}}{|\mathbf{x}-\mathbf{x}'|} - \frac{((\mathbf{x}-\mathbf{x}')\cdot\mathbf{n})\,(\mathbf{x}-\mathbf{x}')}{|\mathbf{x}-\mathbf{x}'|^3}\, dS(\mathbf{x}') \tag{4.21}$$

$$\begin{aligned}\nabla\mathbf{u}_b(\mathbf{x}) = \sum_i \frac{\mathbf{W}_i}{4\pi} \times \int_{\partial\Omega_i} & - \frac{\mathbf{n}\,(\mathbf{x}-\mathbf{x}') + (\mathbf{x}-\mathbf{x}')\,\mathbf{n} + ((\mathbf{x}-\mathbf{x}')\cdot\mathbf{n})\,\mathbf{I}}{|\mathbf{x}-\mathbf{x}'|^3} \\ & + \frac{3\,((\mathbf{x}-\mathbf{x}')\cdot\mathbf{n})\,(\mathbf{x}-\mathbf{x}')\,(\mathbf{x}-\mathbf{x}')}{|\mathbf{x}-\mathbf{x}'|^5}\, dS(\mathbf{x}')\end{aligned} \tag{4.22}$$

Contour Dynamics

One can notice that by taking the curl of Eq. 4.3, we obtain the following expression

$$\nabla^2\mathbf{u} = -\nabla\times\boldsymbol{\omega} \tag{4.23}$$

which is at the basis of contour dynamics (Zabusky et al., 1979). If we consider patches of constant vorticity in three dimensions, $\nabla\times\boldsymbol{\omega}$ is only non-zero and singular at the boundaries of the patches. We apply Green's function to obtain an alternative to Eq. 4.21,

$$\mathbf{u}_b = \sum_i \frac{2\mathbf{W}_i}{4\pi} \times \int_{\partial\Omega_i} \frac{\mathbf{n}}{|\mathbf{x}-\mathbf{x}'|}\, dS(\mathbf{x}') \,. \tag{4.24}$$

This approach, while yielding a simple expression for the velocity, makes no provision for the stream function. Also of interest is that the velocity is not expressed as a curl; the error made in the multipole approximation could therefore have some divergence.

Implementation

The integrals 4.20, 4.21 and 4.22 can be evaluated with a panel description of the boundaries. As for the regular Biot-Savart law, we have to accelerate their computation through the use of multipole expansions. We detail this procedure in Appendix D along with the development of the error bound.

4.3.2 Deforming Objects

In the case of general deformations, it is far more difficult to find a surface-based integral. We present some expressions for velocity. Using the idea of contour dynamics, we have, for constant volume deformations,

$$\mathbf{u}_b(\mathbf{x}) = \sum_i \int_{\partial\Omega_i} G(\mathbf{x}-\mathbf{x}')\boldsymbol{\omega}_i(\mathbf{x}') \times \mathbf{n}\, dS + \sum_i \int_{\Omega_i} G(\mathbf{x}-\mathbf{x}') \left(\nabla \times \boldsymbol{\omega}_i\right)(\mathbf{x}')\, d\mathbf{x}' \,. \quad (4.25)$$

The second term can be rewritten in terms of velocity, thanks to the identity $\nabla \times \nabla \times \mathbf{u} = \nabla(\nabla \cdot \mathbf{u}) - \nabla^2\mathbf{u}$ with $\nabla \cdot \mathbf{u} = 0$,

$$\mathbf{u}_b(\mathbf{x}) = \sum_i \int_{\partial\Omega_i} G(\mathbf{x}-\mathbf{x}')\boldsymbol{\omega}_i(\mathbf{x}') \times \mathbf{n}\, dS - \sum_i \int_{\Omega_i} G(\mathbf{x}-\mathbf{x}')\nabla^2\mathbf{u}_i(\mathbf{x}')\, d\mathbf{x}' \,. \quad (4.26)$$

We can then use Green's second identity

$$\int_V \left(f\nabla^2 g - g\nabla^2 f\right)\, dV = \int \left(f\nabla g - g\nabla f\right) \cdot \mathbf{n}\, dS$$

to obtain

$$\begin{aligned} \mathbf{u}_b(\mathbf{x}) = &\sum_i \int_{\partial\Omega_i} G(\mathbf{x}-\mathbf{x}')\boldsymbol{\omega}_i(\mathbf{x}') \times \mathbf{n}\, dS - \sum_i \int_{\Omega_i} \nabla^2_{\mathbf{x}'}(G(\mathbf{x}-\mathbf{x}'))\mathbf{u}_i(\mathbf{x}')\, d\mathbf{x}' \\ &+ \sum_i \int_{\partial\Omega_i} \left(\mathbf{u}_i \nabla_{\mathbf{x}'}(G(\mathbf{x}-\mathbf{x}')) - G(\mathbf{x}-\mathbf{x}')\nabla_{\mathbf{x}'}\mathbf{u}_i\right) \cdot \mathbf{n}\, dS \,. \end{aligned} \quad (4.27)$$

We see that the second term is null because $\mathbf{x}$ lies outside the objects Ω_i.

A similar approach can be followed for dilatation. For irrotational flows, one has

$$\nabla^2 \mathbf{u} = \nabla \sigma \,, \tag{4.28}$$

which gives us the expression of velocity

$$\mathbf{u}_b^\sigma(\mathbf{x}) = \sum_i \int_{\partial\Omega_i} G(\mathbf{x}-\mathbf{x}')\sigma_i(\mathbf{x}')\mathbf{n}\, dS - \sum_i \int_{\Omega_i} G(\mathbf{x}-\mathbf{x}') \left(\nabla\sigma_i\right)(\mathbf{x}')\, d\mathbf{x}' \,. \tag{4.29}$$

We can use the identity above, this time with $\nabla \times \mathbf{u} = 0$, and the second Green's identity to find

$$\begin{aligned} \mathbf{u}_b^\sigma(\mathbf{x}) = &\sum_i \int_{\partial\Omega_i} G(\mathbf{x}-\mathbf{x}')\sigma_i(\mathbf{x}')\mathbf{n}\, dS \\ &+ \sum_i \int_{\partial\Omega_i} \left(\mathbf{u}_i \nabla_{\mathbf{x}'}(G(\mathbf{x}-\mathbf{x}')) - G(\mathbf{x}-\mathbf{x}')\nabla_{\mathbf{x}'}\mathbf{u}_i\right)\cdot \mathbf{n}\, dS \,. \end{aligned} \tag{4.30}$$

One can then combine the results 4.27 and 4.30 for general deformations

$$\begin{aligned} \mathbf{u}_b(\mathbf{x}) = &\sum_i \int_{\partial\Omega_i} G(\mathbf{x}-\mathbf{x}') \left(\boldsymbol{\omega}_i(\mathbf{x}') \times \mathbf{n} + \sigma_i \mathbf{n}\right)\, dS \\ &+ \sum_i \int_{\partial\Omega_i} \left(\mathbf{u}_i \nabla_{\mathbf{x}'}(G(\mathbf{x}-\mathbf{x}')) - G(\mathbf{x}-\mathbf{x}')\nabla_{\mathbf{x}'}\mathbf{u}_i\right)\cdot \mathbf{n}\, dS \,. \end{aligned} \tag{4.31}$$

This expression involves the velocity and components of its gradient at the surface. It can be simplified to

$$\begin{aligned} \mathbf{u}_b(\mathbf{x}) = &\sum_i \int_{\partial\Omega_i} G(\mathbf{x}-\mathbf{x}') \left(-(\nabla_{\mathbf{x}'}\mathbf{u}_i)^t \cdot \mathbf{n} + (\nabla_{\mathbf{x}'}\cdot \mathbf{u}_i)\mathbf{n}\right)\, dS \\ &+ \sum_i \int_{\partial\Omega_i} \left(\mathbf{u}_i \nabla_{\mathbf{x}'}(G(\mathbf{x}-\mathbf{x}'))\right)\cdot \mathbf{n}\, dS \,. \end{aligned} \tag{4.32}$$

We then note that the factor involving the gradient and divergence of $\mathbf{u}_i$ can be rearranged. We decompose the divergence into its components in and out of the plane

$$\left(\nabla_{\mathbf{x}'}\cdot \mathbf{u}_i\right)\mathbf{n} \equiv \left(\nabla^\pi_{\mathbf{x}'}\cdot \mathbf{u}_i + \frac{\partial(\mathbf{u}_i\cdot\mathbf{n})}{\partial n}\right)\mathbf{n} \,, \tag{4.33}$$

where ∇^π is the in-plane gradient. By definition of the surface normal, we have $\partial\mathbf{n}/\partial n = 0$. The second term can then be combined with the term $-(\nabla_{\mathbf{x}'}\mathbf{u}_i)^t \cdot \mathbf{n}$

$$-(\nabla_{\mathbf{x}'}\mathbf{u}_i)^t \cdot \mathbf{n} + \frac{\partial(\mathbf{u}_i \cdot \mathbf{n})}{\partial n}\mathbf{n} = -\left(\nabla_{\mathbf{x}'}\mathbf{u}_i - \frac{\partial \mathbf{u}_i}{\partial n}\mathbf{n}\right)^t \cdot \mathbf{n} \tag{4.34}$$

to cancel the normal derivatives. We can thus write the contributions of general deformations as

$$\begin{aligned}\mathbf{u}_b(\mathbf{x}) = &\sum_i \int_{\partial\Omega_i} G(\mathbf{x}-\mathbf{x}')\left(-(\nabla^\pi_{\mathbf{x}'}\mathbf{u}_i)^t \cdot \mathbf{n} + (\nabla^\pi_{\mathbf{x}'} \cdot \mathbf{u}_i)\mathbf{n}\right) dS \\ &+ \sum_i \int_{\partial\Omega_i} (\mathbf{u}_i \nabla_{\mathbf{x}'}(G(\mathbf{x}-\mathbf{x}'))) \cdot \mathbf{n}\, dS\,.\end{aligned} \tag{4.35}$$

Not surprisingly, this last expression is more complicated than the one for rigid objects. Nevertheless, it meets the physical safeguard mentioned at the beginning of this section; it only involves the surface velocity or its derivatives in the plane of the surface.

4.4 Vorticity Boundary Conditions

The problem of vorticity boundary conditions has two characteristics of note. It involves the introduction of vorticity at the boundaries. We follow Lighthill's model in this respect (see Koumoutsakos et al., 1994) and this approach yields a Neumann boundary condition on the tangential vorticity flux. The second aspect of vorticity boundary conditions is the solenoidal character of vorticity. The vorticity lines in the flow must connect to the ones inside a spinning or deforming object. This translates into a Dirichlet condition on the normal component of vorticity at the wall,

$$\boldsymbol{\omega} \cdot \mathbf{n}|_{\partial\Omega_i} = \boldsymbol{\omega}_i \cdot \mathbf{n}|_{\partial\Omega_i}\ .$$

This section will focus on this last condition, as the other aspects have been covered in Chapter 1. Let us make the assumption that we have a regular set of particles

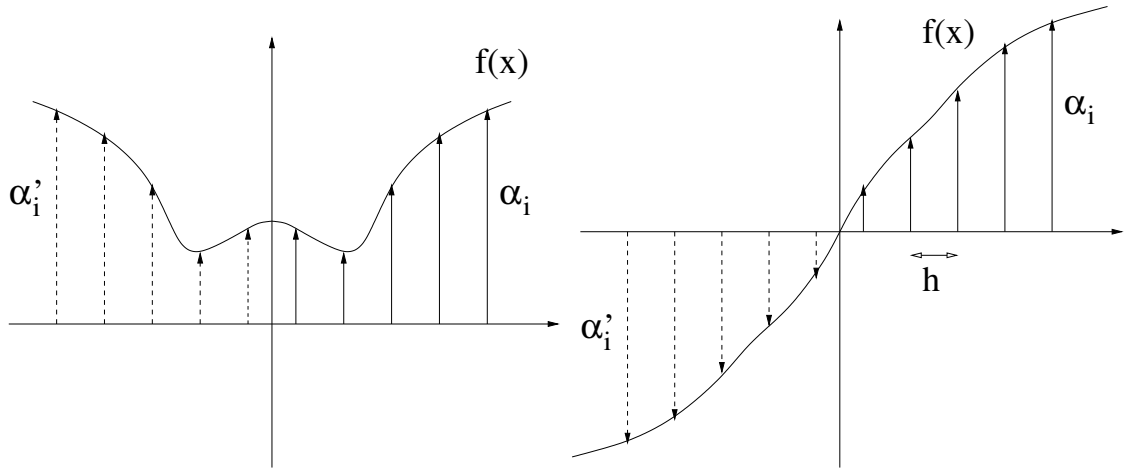

(a) Neumann (b) Dirichlet

Figure 4.2: Method of images: homogeneous boundary conditions

close to the wall. In one dimension, this would correspond to particles located at $x_i = (i + 1/2)h$. One is then confronted with the problem of the inadequacy of the unbounded smoothing functions for elements close to the boundary.

Some elegant solutions using images have been proposed in the context of viscous algorithms. While developing a one-sided test function is possible, it is relatively easy to complete the set of elements next to the wall with images across so that we can still carry out the integration in Eq. 1.19 over $\mathbb{R}^n$. These image particles will be placed across the boundary, symmetrically so that this augmented set of elements constitutes a good interpolation basis. We write for an interpolated quantity

$$f(x) = \sum_{p=0}^{n} \alpha_p \zeta(x - x_p) + \sum_{p=0}^{n} \alpha'_p \zeta(x - x'_p)\,,$$

with $x'_p = -x_p$. The strengths of the images can then be chosen accordingly: $\alpha'_p = \alpha_p$ enforces $df/dx(0) = 0$; $\alpha'_p = -\alpha_p$ imposes $f(0) = 0$. One can refer to Ploumhans et al. (2002) for an application in three dimensions where homogeneous Neumann and Dirichlet conditions are respectively imposed on the tangential and normal components of vorticity.

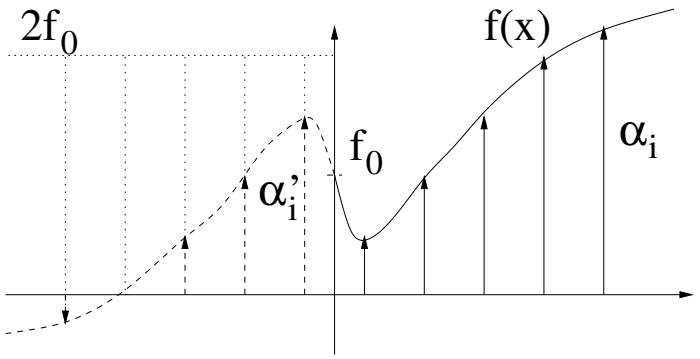

Figure 4.3: Method of images: heterogeneous Dirichlet boundary condition

A heterogeneous Dirichlet condition can be similarly derived. Thanks to our images, we have

$$\sum_{p=0}^{n} h\,\zeta(0-x_p) + \sum_{p=0}^{n} h\,\zeta(0-x'_p) = 1$$

and by symmetry,

$$\sum_{p=0}^{n} h\,\zeta(x_p) = \sum_{p=0}^{n} h\,\zeta(x'_p) = \frac{1}{2}\,.$$

The boundary condition $f(0) = f_0$ will thus be set if we set the image strengths to

$$\alpha'_p = 2hf_0 - \alpha_p\,.$$

In three dimensions, the above only applies to the normal component of vorticity; the tangential ones are treated with a zero flux condition (Ploumhans et al., 2002). For surfaces with moderate curvatures, we will therefore build images with a position and a strength given by

$$\mathbf{x}'_p = \mathbf{x}_p - 2d\mathbf{n} \tag{4.36}$$

$$\boldsymbol{\alpha}'_p = \left(2\left(\boldsymbol{\omega}_i\cdot\mathbf{n}\right)V_p - 2\boldsymbol{\alpha}_p\cdot\mathbf{n}\right)\mathbf{n} + \boldsymbol{\alpha}_p\,, \tag{4.37}$$

where $\mathbf{n}$, the local normal, is defined as the direction of the vector joining the closest point on the surface to the particle and d is the norm of that vector.

This scheme implicitly assumes a flat surface. As a result, its efficiency is contin-

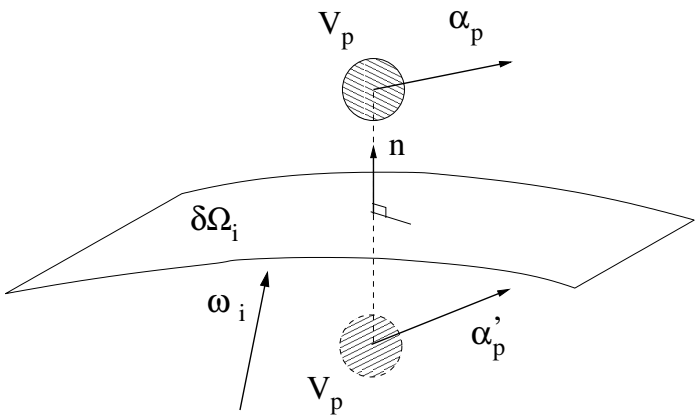

Figure 4.4: Method of images: heterogeneous Dirichlet boundary condition in three dimensions

gent on the smoothness and regularity of the surface. We will see a scheme degradation in regions of high curvature and on sharp edges. A first order correction that accounts for curvature would require a more elaborate image construction.

4.5 Conservation and Diagnostics

4.5.1 Linear Diagnostics

We are considering flows whose vorticity fields have a bounded support. For such flows, we can write (see Batchelor, 1967, 2.9)

$$\int_{\mathbb{R}^3} \boldsymbol{\omega}\, d\mathbf{x} = \mathbf{0}\,. \tag{4.38}$$

This identity holds for inviscid and viscous problems and bounded flows too, if we include vorticity inside the objects. We should then have

$$\int_{\mathbb{R}^3 \setminus \cup\Omega_i} \boldsymbol{\omega}\, d\mathbf{x} = -\int_{\cup\Omega_i} \boldsymbol{\omega}_i\, d\mathbf{x}\,. \tag{4.39}$$

For deforming objects, we can transform this last condition into a surface-based one

$$\int_{\mathbb{R}^3 \setminus \cup \Omega_i} \boldsymbol{\omega}\, d\mathbf{x} = -\int_{\cup \partial\Omega_i} \mathbf{n} \times \mathbf{u}_i \, dS\,. \tag{4.40}$$

For a set of rigid objects, it reduces to

$$\int_{\mathbb{R}^3 \setminus \cup \Omega_i} \boldsymbol{\omega}\, d\mathbf{x} = -2 \sum_i \mathbf{W}_i \,\mathrm{Vol}(\Omega_i)\,. \tag{4.41}$$

This will be of interest when we solve for the boundary vorticity. For a simply-connected geometry, our solver should indeed converge to a solution that satisfies Eq. 4.38. In the viscous case, the condition will have to be enforced on the flux of vorticity that enters the domain and will depend on the kinematics of the boundaries.

If the vortex sheets are bound to the surface, a local result can be derived. Eq. 4.38 is indeed based on the identity $\nabla \cdot \boldsymbol{\omega} = 0$; if we consider a small volume at the wall (Fig. 4.5), we see that

$$\nabla_\pi \cdot \boldsymbol{\gamma} = \boldsymbol{\omega}_i \cdot \mathbf{n}\,, \tag{4.42}$$

where ∇_π is the divergence in the plane locally tangent to the surface $\partial\Omega_i$.

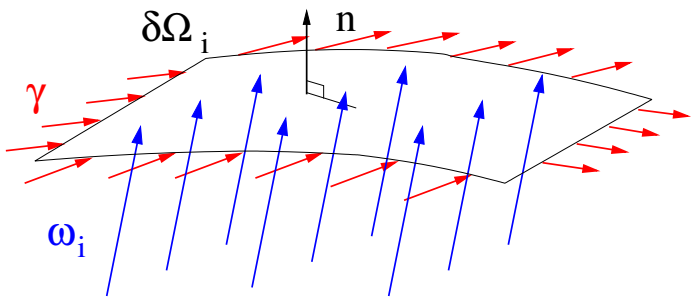

Figure 4.5: Inviscid flow around deforming boundaries: divergence of the bound vortex sheets

Let us now consider the linear impulse. The identity

$$\int_V \mathbf{x} \times \nabla \times \mathbf{a}\, d\mathbf{x} = (\mathcal{N} - 1) \int_V \mathbf{a}\, d\mathbf{x} - \int_{\partial V} \mathbf{x} \times (\mathbf{n} \times \mathbf{a})\; dS \tag{4.43}$$

is valid for a simply-connected volume V. We apply it to the velocity field $\mathbf{u}$ in $\mathbb{R}^3 \setminus \cup\Omega_i$

$$\int_{\mathbb{R}^3\setminus\cup\Omega_i} \mathbf{u}\, d\mathbf{x} = \frac{1}{2}\int_{\mathbb{R}^3\setminus\cup\Omega_i} \mathbf{x}\times\boldsymbol{\omega}\, d\mathbf{x} + \frac{1}{2}\int_{\partial\cup\Omega_i} \mathbf{x}\times(\mathbf{n}\times\mathbf{u})\; dS\,, \tag{4.44}$$

thereby assuming that the objects Ω_i are simply-connected.

4.5.2 Quadratic Diagnostics

The kinetic energy is not conserved for viscous flows. We derive an expression for bounded flows

$$\begin{aligned} E &= \frac{1}{2}\int_{\mathbb{R}^3\setminus\cup\Omega_i} \mathbf{u}\cdot\mathbf{u}\, d\mathbf{x} = \frac{1}{2}\int_{\mathbb{R}^3\setminus\cup\Omega_i} (\nabla\times\boldsymbol{\psi})\cdot(\nabla\times\boldsymbol{\psi})\; d\mathbf{x} \\ &= \frac{1}{2}\int_{\mathbb{R}^3\setminus\cup\Omega_i} \boldsymbol{\psi}\cdot(\nabla\times(\nabla\times\boldsymbol{\psi})) - \nabla\cdot((\nabla\times\boldsymbol{\psi})\times\boldsymbol{\psi})\; d\mathbf{x} \end{aligned}$$

where we used the relation $\mathbf{f}\cdot(\nabla\times\mathbf{g}) = \mathbf{g}\cdot(\nabla\times\mathbf{f}) - \nabla\cdot(\mathbf{f}\times\mathbf{g})$. We then have

$$E = \frac{1}{2}\int_{\mathbb{R}^3\setminus\cup\Omega_i} \boldsymbol{\psi}\cdot\boldsymbol{\omega}\, d\mathbf{x} + \frac{1}{2}\int_{\partial\setminus\cup\Omega_i} (\mathbf{u}\times\boldsymbol{\psi})\cdot\mathbf{n}\, dS\,. \tag{4.45}$$

This will hold for flows with a fast decaying $\boldsymbol{\omega}$ field and for which the velocity goes to 0 at ∞. Logically, flows with an oncoming free stream will have an unbounded surface term at infinity.

The helicity $\mathcal{H} = \int \mathbf{u}\cdot\boldsymbol{\omega}\, d\mathbf{x}$ is not conserved for a viscous flow. This quantity, which measures the entanglement of vorticity lines, will be particularly interesting for flows around spinning boundaries.

4.6 Conclusions

We have introduced a basis for deforming boundaries in the framework of the three dimensional vortex element method. We derived the terms due to deforming or rigid rotating objects in the Biot-Savart law and proposed a method to compute them

from a surface integral. An image method was designed to enforce the heterogeneous boundary condition on normal vorticity. The terms for rigid rotating objects (Eqs. 4.20, 4.21 and 4.22) and the enforcement of boundary conditions by image particles (Eq. 4.36) will be used in our study of flows around spinning spheres (Chapter 6) and flapping motions (Chapter 7).

Chapter 5

Near-Wall Vorticity

5.1 Introduction

The topological adaptation of vortex elements has been the focus of many efforts. From a computational standpoint, it may be interesting to adapt our discretization to the local character of the vorticity and improve the cost and accuracy of the method. A sheet-like representation of vorticity may be interesting in several flow configurations. In wall-bounded flows, vorticity in the near-wall region is mostly parallel to the wall and its gradients are mostly in a direction normal to the wall. The same can be said in multiphase flows where interfaces are a vorticity source.

5.2 Viscous Vortex Sheets

5.2.1 Definition

In a first step, we consider singular vortex sheets with a strength $\gamma(\mathbf{x}')$. We can regularize the sheet distribution by taking its convolution with a function ζ,

$$\boldsymbol{\omega}(\mathbf{x}) = \int_{\text{sheet}} \zeta_{\sigma(\mathbf{x}')}(\mathbf{x}-\mathbf{x}')\boldsymbol{\gamma}(\mathbf{x}')\, dS(\mathbf{x}')\,.$$

We choose the ζ smoothing function to be a Gaussian, i.e., the same as the one used for the particles. The sheet is discretized with flat panels of constant strength $\boldsymbol{\gamma}$; the

above convolution can then be carried out over these panels. This can be computed efficiently by means of a two-dimensional lookup table (Appendix E).

5.2.2 Viscous Diffusion

We now need to account for the viscous diffusion of vorticity. A straightforward technique in this case is the so called core-spreading technique which progressively increases the smoothing radius σ of the sheet. We will rather treat this problem with a strength exchange approach as it is the one we use for the bulk vorticity.

Particle-Sheet Diffusive Transfer

We define a strength exchange scheme between particles and sheet elements. As discussed in Chapter 1, it is based on the approximation of the diffusion operator by an integral operator Eq. 1.19. However, we will not forget to guarantee the symmetry between the perspectives of the particle and the sheet element. This is essential in order to keep the conservation property of the original scheme. Let us start with the case of a particle. We can compute the transfer from a sheet element onto this particle as

$$\left.\frac{d\boldsymbol{\alpha}_p}{dt}\right|_{\gamma_m} = \int_{V_p} \frac{2\nu}{\sigma^2} \int_{V_m} \eta_\sigma(\mathbf{x}-\mathbf{y})\,(\boldsymbol{\omega}(\mathbf{x})-\boldsymbol{\omega}(\mathbf{y}))\;d\mathbf{x}\,d\mathbf{y} \tag{5.1}$$

where V_p and V_m are the volumes of the particle and sheet element, respectively. We use midpoint quadrature for the integral over the particle volume

$$\left.\frac{d\boldsymbol{\alpha}_p}{dt}\right|_{\gamma_m} = \frac{2\nu}{\sigma^2} \int_{V_{\text{sheet}}} (\boldsymbol{\omega}(\mathbf{x})V_p - \boldsymbol{\alpha}_p)\eta_\sigma(\mathbf{x}-\mathbf{x}_p)\,d\mathbf{x}\,. \tag{5.2}$$

If we now assume that $\boldsymbol{\omega}(\mathbf{x})$ is singular inside the sheet element with a constant finite integral $\boldsymbol{\gamma}$ across the thickness of the sheet element, the above expression reduces to

$$\left.\frac{d\boldsymbol{\alpha}_p}{dt}\right|_{\boldsymbol{\gamma}_m} = \frac{2\nu}{\sigma^2}(\boldsymbol{\gamma}_m V_p - \boldsymbol{\alpha}_p\, h) \int_{S_m} \eta_\sigma(\mathbf{x}-\mathbf{x}_p)\,dS(\mathbf{x})\,, \tag{5.3}$$

where we define h as the thickness of the sheet. One technique to build a kernel η consists in using the function ζ (Degond and Mas-Gallic, 1989, Cottet and Koumoutsakos, 2000),

$$\eta(\rho) = -\frac{1}{\rho}\frac{d}{d\rho}\zeta(\rho)\,, \tag{5.4}$$

which in the case of the Gaussian yields the same Gaussian. The last factor in Eq. 5.3 is therefore the same as for the regularization.

In the converse case, the flux from the particle to the sheet element will yield

$$\left.\frac{d(\boldsymbol{\gamma}_m S_m)}{dt}\right|_{\boldsymbol{\alpha}_p} = \frac{2\nu}{\sigma^2}(\boldsymbol{\alpha}_p\, h - \boldsymbol{\gamma}_m V_p)\int_{S_m}\eta_\sigma(\mathbf{x}-\mathbf{x}_p)\,dS(\mathbf{x})\,. \tag{5.5}$$

This expression is identical to Eq. 5.3 but for the opposite sign, as it should be to enforce conservation.

Sheet Element to Element Diffusive Transfer

The transfer of vorticity between sheet elements can be handled in a similar fashion. The integration is more difficult to carry out, as it is a double surface integral

$$\left.\frac{d(\boldsymbol{\gamma}_m S_m)}{dt}\right|_{\boldsymbol{\gamma}_n} = \frac{2\nu}{\sigma^2}\,(h_m\boldsymbol{\gamma}_n - h_n\boldsymbol{\gamma}_m)\int_{S_m}\int_{S_n}\eta_\sigma(\mathbf{x}-\mathbf{y})\,dS_{\mathbf{x}}\,dS_{\mathbf{y}}\,. \tag{5.6}$$

We use quadrature for their evaluation while keeping in mind the geometry of our problem. Most of the flux goes out of the plane to the particles and therefore, we will not require the same level of accuracy for this contribution. Sample results for the case of one-sided sheets are provided in Section 5.3.2.

5.2.3 Biot-Savart

We carry out the convolution of the Biot-Savart kernel over a panel. The integrals do not have an analytical expression and have to be tabulated (see Appendix E).

5.3 Wall Vorticity

5.3.1 Regularization Near Boundaries

Let us now go back to our bounded problem. It might be interesting to consider a different set of elements in regions close to the wall for several reasons. These regions are characterized by mostly planar distributions of vorticity—the boundary layers—and the inadequacy of the spherical test function of our particles. The latter evidently affects the accuracy of the method near the wall (see Cottet and Koumoutsakos, 2000, and references therein). If we stay in the framework of regularized elements, the regularization has to be able to deform when close to the boundaries to enforce basic properties such as $\int \zeta dV = 1$.

5.3.2 One-Sided Vortex Sheet

Definition

We consider the limiting case of a vortex sheet situated right at the boundary. We have to modify its mollifier as to satisfy the above condition. We let $\zeta_{\text{one-sided}} = \frac{1}{M}\zeta_{\text{unbounded}}$; M has to be adjusted according to the local geometry (see Appendix E). In the case of a flat surface, we just have $M = 1/2$. We will take M constant over a panel, M_m.

For the same reason, we need to redefine the volume of a panel. For the sake of consistency, we choose to use the same modifier M_m as for the regularization. The volume associated to a one-sided panel is then $S_m\, h\, M_m$.

Conservative Viscous Scheme

Sheet Element to Particle Diffusive Transfer Let us begin with a one-dimensional problem such as the one in Section 4.4. We will now consider a set of elements where the first one lies at $x = 0$. We complete the set with images except for the first element. For a problem with a homogeneous Neumann condition, we can thus write

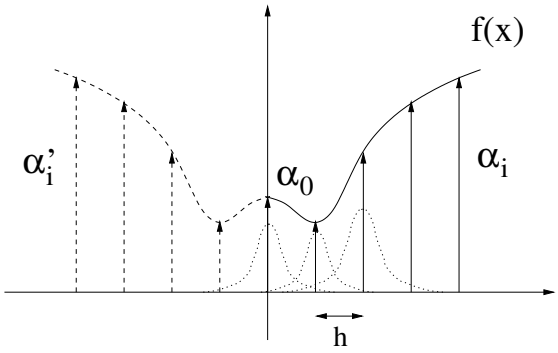

Figure 5.1: Wall element definition

for the element at $x = 0$

$$\frac{d\alpha_0}{dt} = \frac{2\nu}{\sigma^2} \sum_i (\alpha_i h_0 - \alpha_0 h_i)\, 2\eta_\sigma(x_i)$$

where the factor of two is due to the image contributions, $\alpha'_i = \alpha_i$ (Fig. 5.1). We consider only the physical part of the central element with its half on the positive side. We define $\gamma = \alpha_0/2$ and $h_\gamma = h_0/2$. We then have

$$\frac{d\gamma}{dt} = \frac{2\nu}{\sigma^2} \sum_i (\alpha_i h_\gamma - \gamma h_i)\, 2\eta_\sigma(x_i)\,.$$

From this last result, we propose the following ansatz for the diffusion flux from a particle onto a wall sheet element

$$\left.\frac{d(\boldsymbol{\gamma}_m S_m)}{dt}\right|_{\boldsymbol{\alpha}_p} = \frac{2\nu}{\sigma^2} (\boldsymbol{\alpha}_p M h - \boldsymbol{\gamma}_m V_p) \int_{S_m} \frac{1}{M} \eta_\sigma(\mathbf{x} - \mathbf{x}_p) dS\,. \tag{5.7}$$

Conversely, if one were to look at the contribution to an element $i > 0$ from the central element,

$$\begin{aligned} \left.\frac{d\alpha_i}{dt}\right|_{\alpha_0} &= \frac{2\nu}{\sigma^2} (\alpha_0 h_i - \alpha_i h_0)\, \eta_\sigma(x_i) \\ &= \frac{2\nu}{\sigma^2} (\gamma h_i - \alpha_i h_0)\, 2\eta_\sigma(x_i)\,; \end{aligned}$$

following the same ansatz, we find that our scheme is consistent

$$\left.\frac{d\boldsymbol{\alpha}_p}{dt}\right|_{\boldsymbol{\gamma}_m} = \frac{2\nu}{\sigma^2}\left(\boldsymbol{\gamma}_m V_p - \boldsymbol{\alpha}_p M h\right)\int_{S_m}\frac{1}{M}\eta_\sigma(\mathbf{x}-\mathbf{x}_p)dS = -\left.\frac{d(\boldsymbol{\gamma}_m S_m)}{dt}\right|_{\boldsymbol{\alpha}_p}. \tag{5.8}$$

We can give two interpretations to this approach. In the first place, this scheme tacitly includes contributions from images (as seen in Section 4.4). It can also be considered as a limiting case of one-sided integral operator, such as those described by Eldredge et al. (2002a,b).

Sheet Element to Element Diffusive Transfer In order to treat the diffusion right at the wall, we take some precautions. In convex regions, the unbounded algorithm ignores curvature and allows a spurious flux through the wall. In such cases, we will consider diffusion on a curved surface, which is a popular problem in molecular biology. From Balakrishnan (2000) and Faraudo (2002), we see that a first order solution in geodesic coordinates is identical to the one in a flat Euclidean space; we write

$$\left.\frac{d(\boldsymbol{\gamma}_m S_m)}{dt}\right|_{\boldsymbol{\gamma}_n} = \frac{2\nu}{\sigma^2}\left(M_m h_m \boldsymbol{\gamma}_n - M_n h_n \boldsymbol{\gamma}_m\right)\int_{S_m}\int_{S_n}\eta_\sigma(|\mathbf{x}-\mathbf{y}|')\,dS_{\mathbf{x}}\,dS_{\mathbf{y}} \tag{5.9}$$

where we now use $|\mathbf{x}-\mathbf{y}|'$, the distance measured along the surface in the PSE kernel. In a concave region, we use the same approach as in the unbounded case.

Example We consider the diffusion of a quantity f over a sphere of radius $R = 0.5$ with $\nu = 0.01$. The initial condition is a Dirac function at the top of the sphere; the solution can be developed (Balakrishnan, 2000) as

$$f(\mathbf{x},t) = \frac{1}{4\pi\nu t}e^{-\frac{u^2}{4\nu t}}\left(1+\frac{\nu t}{3R^2}+\frac{1}{15}\left(\frac{\nu t}{R^2}\right)^2\frac{4}{315}\left(\frac{\nu t}{R^2}\right)^3+\cdots\right)$$

where $u = R\arcsin(\mathbf{x}_3/R)$ is the geodesic distance to the source and R is the radius of the sphere. The double surface integral is evaluated with a one point quadrature. In Fig. 5.2, we see that our scheme is consistent but its local error exhibits a pattern

that follows the triangular mesh. This is clearly due to the one point quadrature and can be improved by increasing the order of quadrature.

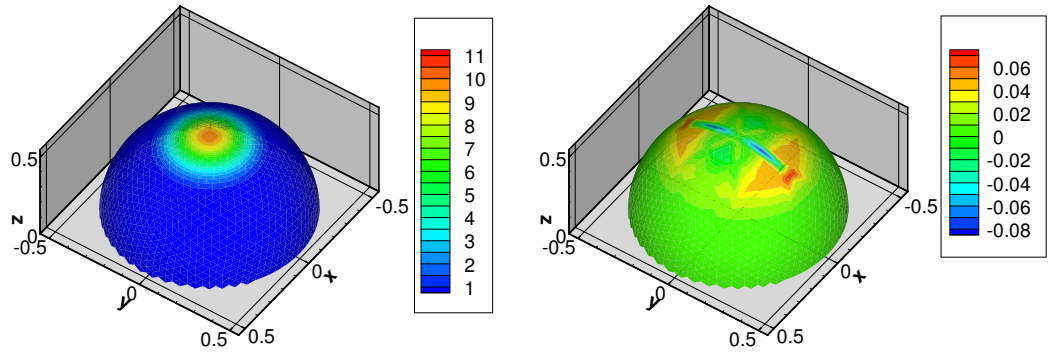

(a) f (b) Error

Figure 5.2: Diffusion on a sphere: solution and error at $t = 4$

Dirichlet Boundary Condition

In Section 4.4, we introduced an image construction to enforce the Dirichlet condition on the normal component of vorticity at the wall. Let us consider the one-dimensional example with a central element. The evolution equation for α_0 is

$$\frac{d\alpha_0}{dt} = \frac{2\nu}{\sigma^2} \sum_i \left(\alpha_i h_0 - \alpha_0 h_i\right) \eta_\sigma(x_i) + \left(\alpha_i' h_0 - \alpha_0 h_i\right) \eta_\sigma(x_i) \,.$$

The image strengths α_i' are set to $2 f_0 h_i - \alpha_i$. We also assume that α_0 is close to the value $f_0 h_0$ and add the term $(f_0 h_0 h_0 - \alpha_0 h_0)\eta(0)$ to the above expression. Because $\sum_i h\,\eta(x_i) = \sum_i h\,\zeta(x_i) = 1$, we have

$$\frac{d\alpha_0}{dt} = \frac{2\nu}{\sigma^2} \left(f_0 h_0 - \alpha_0\right) \,. \tag{5.10}$$

From the wall element standpoint, the strength exchange scheme therefore amounts to the relaxation of α_0 to the value $f_0 h_0$. We note that the relaxation coefficient is

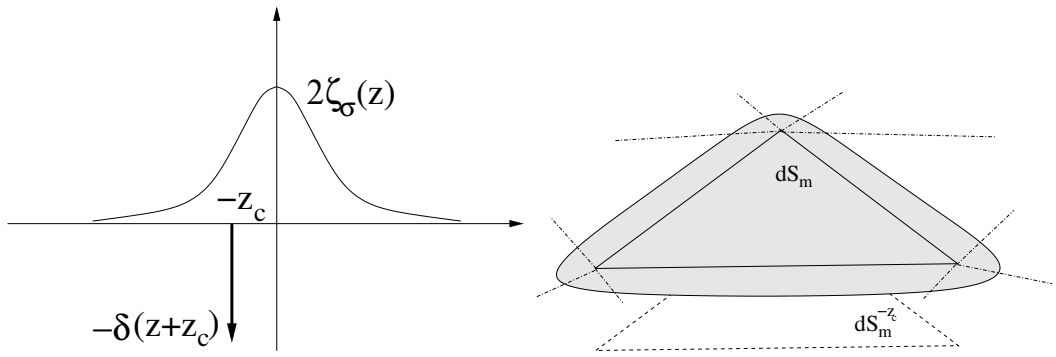

(a) 1D (b) 3D

Figure 5.3: Wall element: Biot-Savart approximation

$2\nu\Delta t/\sigma^2$, which is, up to a constant factor, the stability coefficient of the viscous scheme. We again define $\gamma = \alpha_0/2$ and use this approach for the normal component of the wall elements

$$\frac{d((\boldsymbol{\gamma}_m \cdot \mathbf{n})S_m)}{dt} = \frac{2\nu}{\sigma^2}((\mathbf{W} \cdot \mathbf{n})\, h - (\boldsymbol{\gamma}_m \cdot \mathbf{n})) \tag{5.11}$$

to enforce the Dirichlet condition of (Section 4.4).

Biot-Savart

The Biot-Savart integral over the one-sided sheet is computed approximately. We consider one surface element. For the sake of consistency with its definition, we will compute its stream-function contribution as the sum of the full panel modified by $1/M$, and of a singular panel located underneath it at the centroid of the half-distribution

$$\boldsymbol{\psi}_m = \int_{S_m} \boldsymbol{\gamma}_m \frac{1}{M} G_\sigma(\mathbf{x} - \mathbf{x}')\, dS(\mathbf{x}') + \int_{S_m^{-z_c}} \boldsymbol{\gamma}_m \left(1 - \frac{1}{M}\right) G(\mathbf{x} - \mathbf{x}')\, dS(\mathbf{x}')\,. \tag{5.12}$$

This approach is sketched in Fig. 5.3.

5.3.3 Convection and Stretching

The vorticity carried by the elements is located at the surface. We elect to convect this vorticity at the wall speed as a consequence of the no-slip condition. In the case of a rigid object, the effect of the vortex stretching term reduces to the rotation of the vorticity lines. For deforming surfaces, stretching will have to be accounted for in a fashion similar to the one for unbounded three dimensional vortex sheets (Brady, 2000, and references therein).

5.3.4 Redistribution

The presence of a buffer layer between the wall and the free elements may also prove useful for redistributions near a boundary. Several approaches have been proposed to handle this problem. One can adapt the redistribution lattice to the geometry (Koumoutsakos and Leonard, 1995) or design schemes to maintain conservation when close to the boundary (Ploumhans and Winckelmans, 2000, Ploumhans, 2001). We will use the attached elements in a simple scheme to enforce conservation of vorticity near the wall. In a first step (Fig. 5.4(a)), the particles are redistributed without any regard to the boundaries. Some of the redistributed particles are then inside or too close to the boundaries. They are destroyed and their circulation is transferred to the nearest wall-element (Fig. 5.4(b)). This scheme only conserves circulation but the construction of higher order schemes should be straightforward.

5.3.5 Corrected Value at the Wall

Our use of specific elements at the wall improves the representation near the wall, thereby ensuring conservation and a correct interpolation. However the vorticity at the wall requires a specific treatment. It is a result of the balance between its source at the wall and the diffusion into the flow, both of which are large on most of the

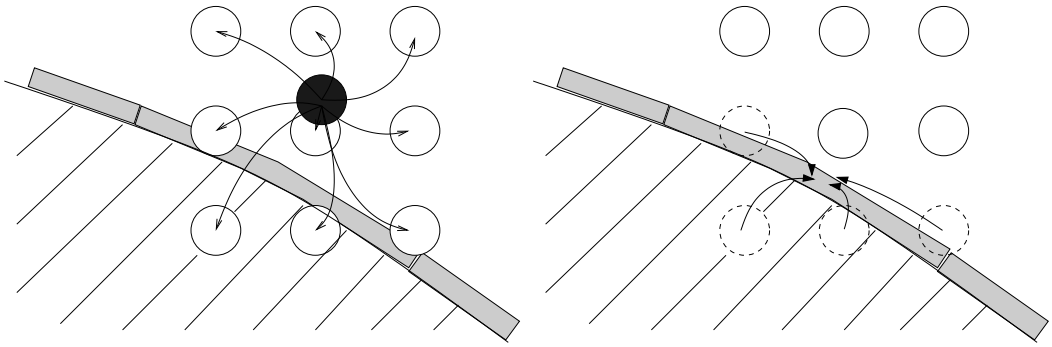

(a) Unbounded step (b) Correction

Figure 5.4: Wall element: redistribution scheme

surface. We introduce a local expression which takes the vorticity flux into account

$$\begin{aligned}\boldsymbol{\omega}(\mathbf{x}_{\text{wall}}) = &\sum_p \left(\boldsymbol{\alpha}_p \zeta(\mathbf{x}_{\text{wall}} - \mathbf{x}_p) + \boldsymbol{\alpha}'_p \zeta(\mathbf{x}_{\text{wall}} - \mathbf{x}^i_p)\right) + \\ &\sum_m \boldsymbol{\gamma}_m \int_{S_m} \frac{1}{M_m} \zeta_\sigma(\mathbf{x}_{\text{wall}} - \mathbf{x}') \boldsymbol{\gamma}_m \, dS(\mathbf{x}') - \frac{\partial \boldsymbol{\omega}}{\partial n}(\mathbf{x}_{\text{wall}}) 2\sqrt{\frac{\nu \delta t}{\pi}} \,.\end{aligned} \tag{5.13}$$

If we consider the tangential components of vorticity, the contributions of the particles, their images, and the wall element only account for the zero flux condition during the time step. The last term of Eq. 5.13 is the solution at the wall at $t = \delta t$ of the one-dimensional diffusion problem

$$\begin{aligned}\frac{\partial \boldsymbol{\omega}}{\partial t} &= \nu \nabla^2 \boldsymbol{\omega} \text{ for } x > 0 \\ \boldsymbol{\omega} &= 0 \text{ for } t = 0, x > 0 \\ \frac{\partial \boldsymbol{\omega}}{\partial n} &= \text{constant} \,.\end{aligned}$$

One could object that the flux is not known with great accuracy and affected by numerical noise. This point is addressed at the end of this section.

Example

We consider a one dimensional example that is somewhat reminiscent of our physical problem. Our domain is the positive x-axis. We discretize a function f with a set of Gaussian particles for which we take $\eta = \zeta$, $h = \sigma$. We use a wall element. The elements are therefore positioned at $x_i = ih$.

A Neumann boundary condition is imposed at $x = 0$, $-\nu\,\partial f/\partial n = g(t)$. During the first part of the time-step, we use our particles and their images to cancel the flux at $x = 0$. We then integrate the contribution of a constant flux onto the elements during the time step $\partial\alpha|_W = \int_{V_i} \partial f/\partial t dx$ (Koumoutsakos et al., 1994, Ploumhans et al., 2002).

In the case of a sinusoidal flux $g(t) = \sin(2\pi t/T)$, there exists an analytical expression for the wall value

$$f(0,t) = -\sqrt{\frac{T}{\pi\nu}}\left(S\left(2\sqrt{t/T}\right)\cos(2\pi t/T) - C\left(2\sqrt{t/T}\right)\sin(2\pi t/T)\right),$$

where $S(u)$ and $C(u)$ are the Fresnel integrals, $S(u) = \int_0^u \sin(\pi t^2/2)\,dt$ and $C(u) = \int_0^u \cos(\pi t^2/2)\,dt$. In Fig. 5.5, we investigate the behavior of the expression with respect to the resolution (h,δt) and the PSE stability parameter r_{PSE}. Eq. 5.13 does provide a better estimate than the straight summation of the shape functions and its effectiveness is fairly constant between the two values of r_{PSE}.

A last point that we have already alluded to is the use of the vorticity flux in our correction. In practice, this quantity is indeed solved for at every time step and is noisy in time and space. The space noisiness can be imputed to the interactions of the particles with the boundary. In general, the boundary will not be aligned with any of the lattice planes causing the particle coverage to be irregular near the wall. This issue was a rationale for the development of isotropic distributions (Chapter 2) and of near wall elements.

The time issue can be addressed by not including the boundary condition enforcement in the time integration. We use a second order Adams-Bashforth like Ploumhans et al. (2002), but treat the wall boundary condition as a correction that is already

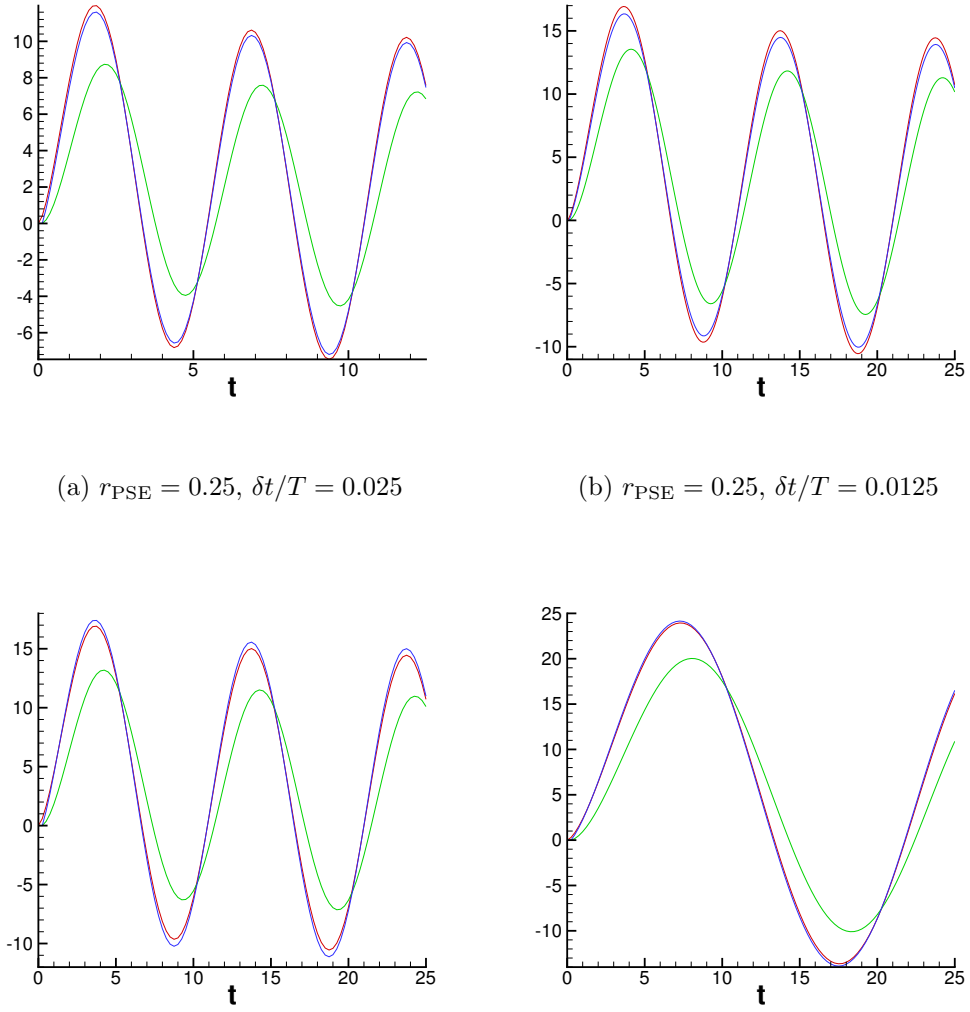

(a) $r_{\mathrm{PSE}} = 0.25$, $\delta t/T = 0.025$

(b) $r_{\mathrm{PSE}} = 0.25$, $\delta t/T = 0.0125$

(c) $r_{\mathrm{PSE}} = 0.5$, $\delta t/T = 0.025$

(d) $r_{\mathrm{PSE}} = 0.5$, $\delta t/T = 0.0125$

Figure 5.5: One-dimensional example with sinusoidal flux, wall value: analytical (red), simple summation of blobs and images (green), summation with correction (blue) for two values of the PSE stability parameter $r_{\mathrm{PSE}} = \nu\,\delta t/h^2$ and $\delta t/T$

integrated in time. As can be seen from its stability region, AB 2 does not damp purely oscillatory modes and probably leads to a cycle of over-correcting fluxes from one time step to another.

5.4 Conclusions

The vortex element method with regularized particles and Biot-Savart summation is in difficulty near the boundaries where the interpolation and integration accuracy are degraded. We introduce wall elements which have one-sided shape functions built to be conservative. These elements interact viscously with the free elements and stay attached to the wall, thus enforcing tacitly the no-slip condition for vorticity at the wall. They also allow the free elements to stand further away from the wall, thereby lowering the chances of an element to enter the boundaries and alleviating the need for images in the viscous scheme. The closest image is now at roughly 2 σ; for a Gaussian smoothing, this represents $\exp -\frac{4\sigma^2}{2\sigma^2} < \exp -\frac{\sigma^2}{2\sigma^2}$. Finally, we introduced a correction to provide an improved estimation of wall quantities by accounting for the flux at the wall.

Chapter 6

Flows Past Spinning Spheres

6.1 Introduction

Flow around spinning spheres are met in a wide array of domains, from sports to suspension problems in chemical or environmental engineering. Despite this ubiquity, studies of this problem are scarce in the literature.

In the case of the transverse rotation, the first observations are attributed to Robins (1805). However, the discovered lift effect will be named after Magnus (1853). Barkla and Auchterlonie (1971) discuss these early works with more depth and provide some measurements of the lift by using an experimental setup in direct continuation of Robins's work. Their results cover Reynolds numbers of $1.5\,10^3$ to 10^5. There are analytical results by Rubinow and Keller (1961) for very low Reynolds numbers using Stokes and Oseen expansions. Until recently, results were particularly rare for intermediate Re ranges (Tsuji et al., 1985, Oesterlé and Bui Dinh, 1998).

For an axial rotation, even fewer results are available. A couple of numerical studies were carried out recently (Kim and Choi, 2002, Pregnalato et al., 2002).

6.2 Configuration

We are considering the impulsively started flow around a spinning sphere at $Re = U_\infty D/\nu = 300$ and a spin rate $WD/2U_\infty = 0.5$, where D is the sphere diameter, U_∞ is

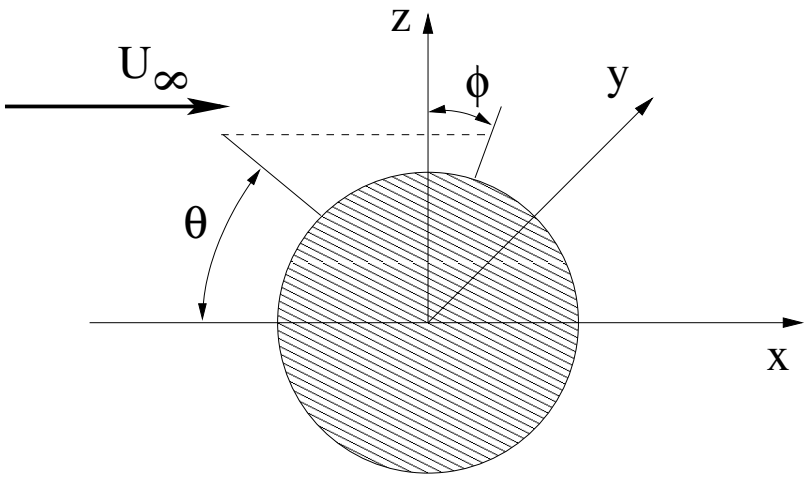

Figure 6.1: Configuration and coordinate system

the free stream velocity and W is the angular velocity of the sphere. The free-stream is in the direction of $\mathbf{e}_x$. Three configurations are studied, one per direction of the angular velocity vector: $\mathbf{e}_x$, $\mathbf{e}_y$ and $\sqrt{2}/2\mathbf{e}_x + \sqrt{2}/2\mathbf{e}_y$. Both the free-stream and the rotation are impulsively started at $t = 0$.

Fig. 6.1 shows the coordinate systems used in this chapter and the orientation of the free-stream. Cylindrical coordinates, in particular, will be used for the localization of critical points on the sphere or in its neighborhood. All the results of this chapter are non-dimensionalized

$$\begin{aligned} t &= \frac{U_\infty t^*}{D} \\ \mathbf{x} &= \frac{\mathbf{x}^*}{D} \end{aligned}$$

where * denotes the corresponding dimensional quantities.

6.3 Stream-Wise Rotation

We start with $\mathbf{W} = \mathbf{e}_x$. This first case is interesting for several reasons. Previous numerical results by Kim and Choi (2002) show that, for certain ranges of Re and WR/U_∞, the wake may be fully unsteady, steady, or steady in a rotating frame.

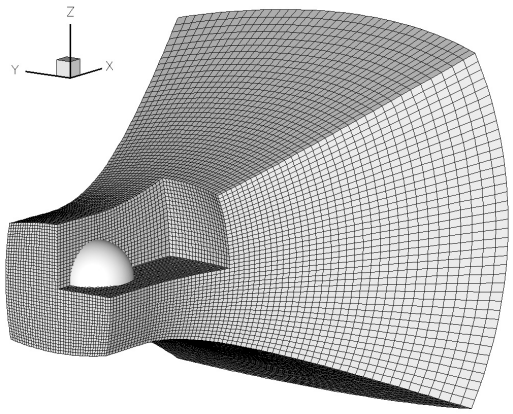

Figure 6.2: Trumpet mapping shape and position: the mapping is cut in the neighborhood of the sphere to provide a better view

We will refer to this last configuration as frozen as in our reference. Our values of $Re = 300$ and of the spin rate $WR/U_\infty = 0.5$ correspond to a frozen configuration. A perturbation is applied to the free-stream

$$\mathbf{u}_{\text{perturb}} = \mathbf{e}_z \cos(2\pi(t-2)) \; for \; t \in [2;3]$$

in order to accelerate the transition to the unsteady asymmetric wake.

6.3.1 Numerics

The sphere was discretized with 20480 triangles; it was generated by recursively dividing the faces of a icosahedron. The time step was set to 0.0125. Particles were redistributed every 5 time steps onto a face-centered cubic lattice by using the F_3' scheme of Chapter 2. The redistribution lattice was stretched using a trumpet-shaped mapping (Daeninck et al., 2004) which progressively reduces the resolution as one moves downstream (Fig. 6.2). The parameters of Table 6.1 were chosen to guarantee a roughly constant resolution in the sphere neighborhood where the particle spacing is 0.015.

Fig. 6.3 shows the evolution of numerical diagnostics. While the problem size

R_0	2
m	600
center	0 0 0

Table 6.1: Trumpet mapping parameters

(Fig. 6.3(a)) reaches a plateau, thanks to the anisotropic redistribution, the mesh Reynolds number (Fig. 6.3(b)) exhibits a growth from $t = 15$. For $t < 15$, this maximum is achieved in the boundary layers. For $t > 15$, the wake (Fig. 6.4, 6.7) contains stronger vorticity structures which are transported into coarser regions of the lattice ($x > 8$).

A quantity that is often useful in three dimensional vortex methods is $\int |\boldsymbol{\omega}_\sigma - \boldsymbol{\omega}|^2 d\mathbf{x}$; it measures the difference between vorticity represented by our elements $\sum_p \boldsymbol{\alpha}_p \zeta_{\sigma_p}(\mathbf{x}-\mathbf{x}_p)$ and the curl of the velocity given by the Biot-Savart law $\sum_p \mathbf{K}\sigma_p(\mathbf{x}-\mathbf{x}_p) \times \boldsymbol{\alpha}_p$. Because the second field is divergence-free by definition, this quantity is often referred to as the divergence error. Our results (Fig. 6.3(c)) show that this quantity is roughly constant throughout the simulation.

The last diagnostic is the Courant number (Fig. 6.3(d)). Because we use a Lagrangian method, the classical formulation in terms of the velocity, $C_u = |\mathbf{u}|_{\max} \delta t/h$, is not the most appropriate. Rather, one can consider a figure based on vorticity $C_\omega = |\boldsymbol{\omega}|_{\max} \delta t$ or even the velocity gradient $C_{|\nabla \mathbf{u}|} = |\nabla \mathbf{u}|_{\max} \delta t$, which tracks the largest relative displacement of material elements over a time step. Let us add some nuance here: in a bounded flow, C_u still has importance as we do not want elements to cross the boundaries.

The computational time was approximately 300 hours on six processors. This includes the computation and sampling of fields for visualization purposes.

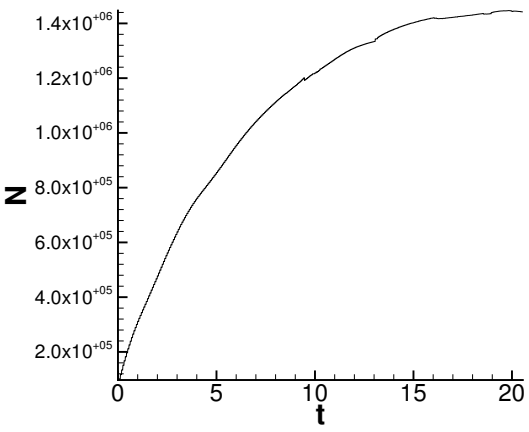

(a) Number of elements

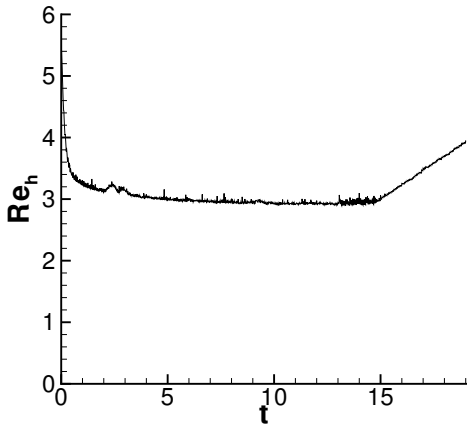

(b) Maximum mesh Reynolds number

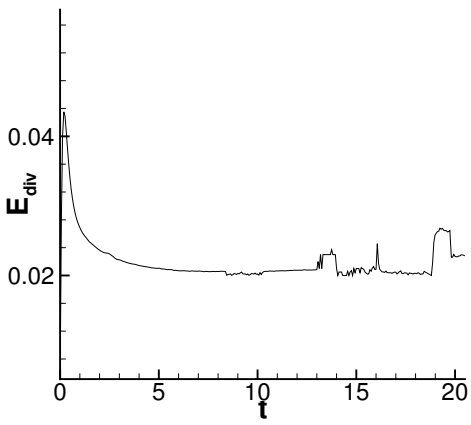

(c) Divergence error

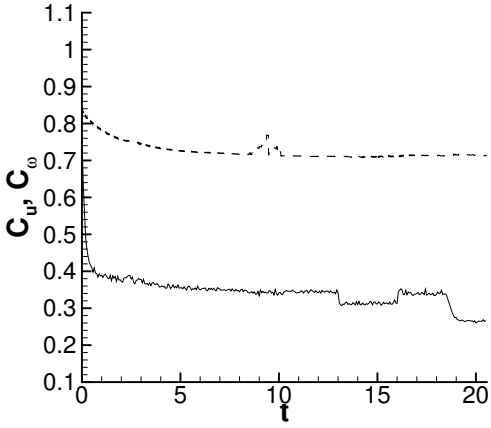

(d) Courant number, vorticity expression (solid) and velocity expression (dashed)

Figure 6.3: Spinning sphere at $Re = 300$, stream-wise rotation: numerical diagnostics

6.3.2 Wake

We begin our analysis of the physics of this flow by considering its wake. We first consider the vorticity structures using the Q-criterion (Hunt et al., 1988) where Q is the second invariant of the the $\nabla \mathbf{u}$ tensor

$$Q = \frac{1}{2}\left(\Omega_{ij}\Omega_{ij} - S_{ij}S_{ij}\right) \ . \tag{6.1}$$

In the case of an incompressible flow, it can be rewritten as

$$Q = -\frac{1}{2} Tr(\nabla \mathbf{u}_{ij} \nabla \mathbf{u}_{ij}) \ . \tag{6.2}$$

$Q > 0$ regions are characterized by the preponderance of the rotation rate over the strain rate and the likelihood of a minimum in pressure since $Q = \frac{\nabla^2 p}{2\rho}$ (Jeong and Hussain, 1995, Dubief and Delcayre, 2000). The evolution of the surfaces $Q = 0$ in Fig. 6.4 shows the growth of a nearly axis-symmetric wake and its transition to the aforementioned frozen configuration. As Fig. 6.5 suggests, the wake consists of a central vortex filament whose vorticity is pointing downstream–$\omega_x > 0$ like the sphere angular velocity–, and recirculations which also have some stream-wise vorticity pointing upstream–$\omega_x < 0$–(Fig. 6.5). This configuration is evidently a consequence of the solenoidal character of vorticity, as vortex lines originating in the back of the sphere have to make their way to the front.

The $\omega_x < 0$ structures grow in size until late into the simulation, $t \simeq 10$, at which point the oscillation of the center filament brings regions with vorticity of opposite signs closer. The viscous cancellation of oppositely signed vorticity is then locally enhanced, which brings even more asymmetry to the azimuthal velocity. For this reason, the $\omega_x < 0$ corona that was somewhat diffuse for $t < 10$ gives way to more localized structures that are wrapped around the $\omega_x > 0$ filament (Fig. 6.6 and 6.7). These structures eventually form a steady helical strand that rotates at its own rate (Fig. 6.4).

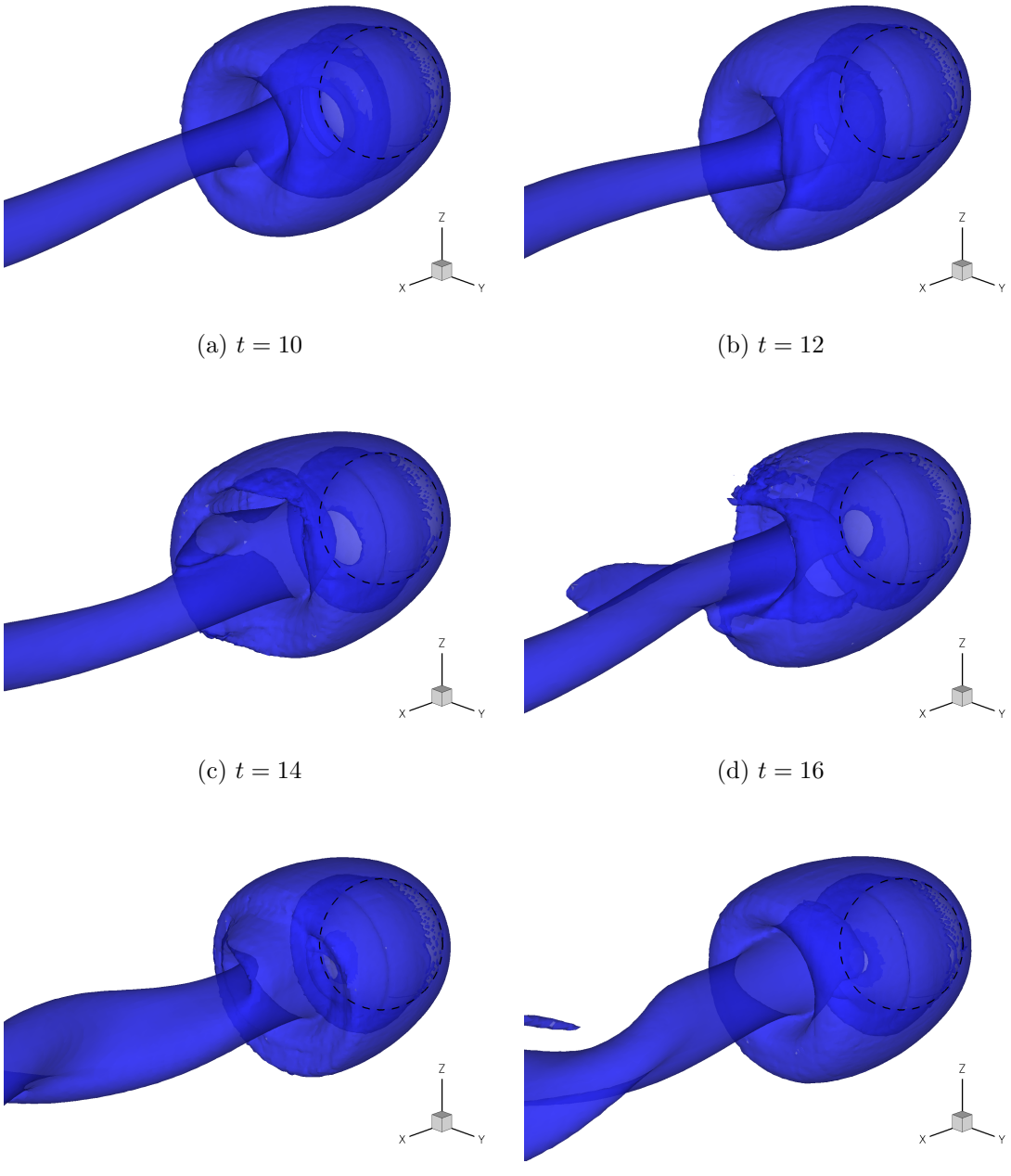

(a) $t = 10$ (b) $t = 12$

(c) $t = 14$ (d) $t = 16$

(e) $t = 18$ (f) $t = 20$

Figure 6.4: Spinning sphere at $Re = 300$, stream-wise rotation: vorticity structures identified by the iso-surface $Q = 0$; partial transparency of the iso-surfaces and the dashed lines help localizing the sphere

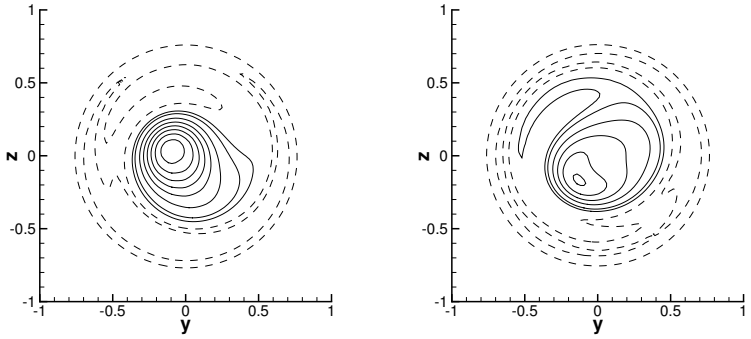

(a) $t = 10$ (b) $t = 12$

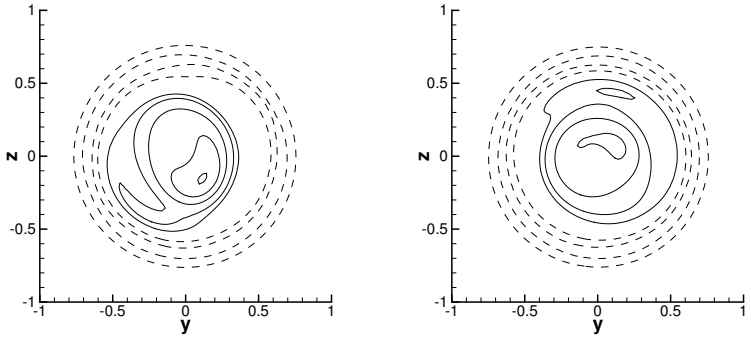

(c) $t = 14$ (d) $t = 16$

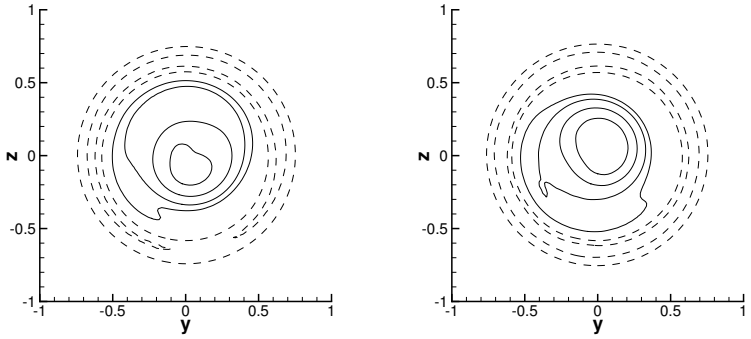

(e) $t = 18$ (f) $t = 20$

Figure 6.5: Spinning sphere at $Re = 300$, stream-wise rotation: stream-wise vorticity at $x = 1$; contours values are in the interval $[-4; 4]$ by steps of 0.5, 0 is omitted and ± 0.25 were added. Positive values are solid; negatives ones, dashed.

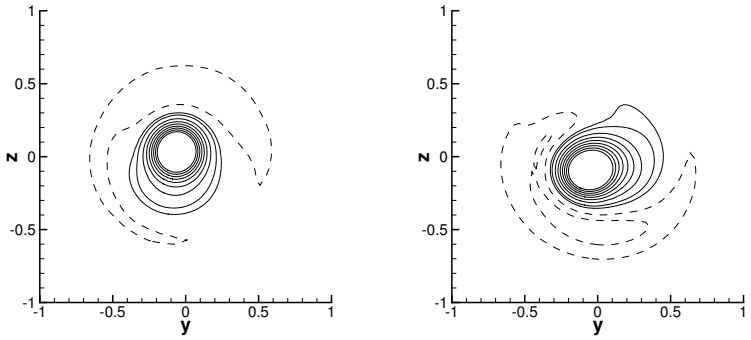

(a) $t = 10$ (b) $t = 12$

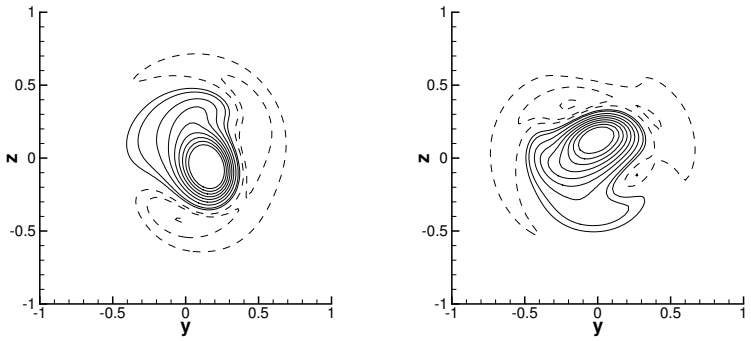

(c) $t = 14$ (d) $t = 16$

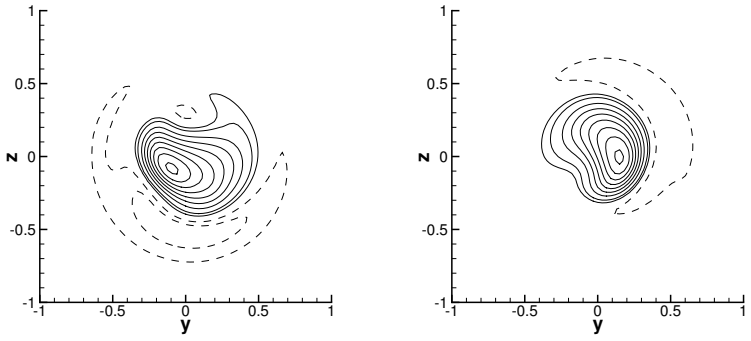

(e) $t = 18$ (f) $t = 20$

Figure 6.6: Spinning sphere at $Re = 300$, stream-wise rotation: stream-wise vorticity at $x = 2$; contours values are the same as in Fig. 6.5

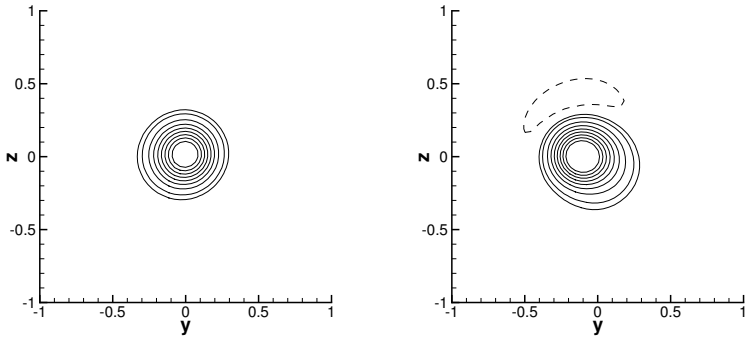

(a) $t = 10$ (b) $t = 12$

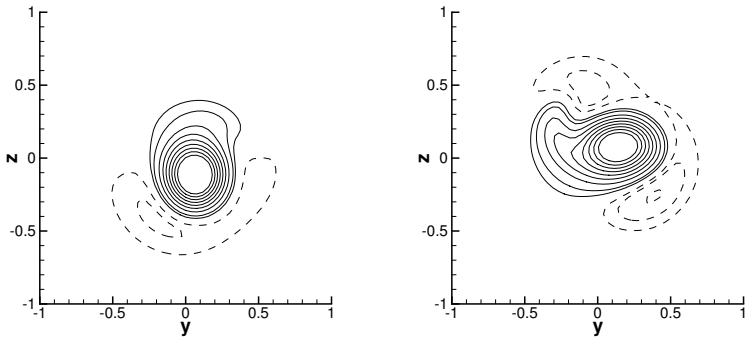

(c) $t = 14$ (d) $t = 16$

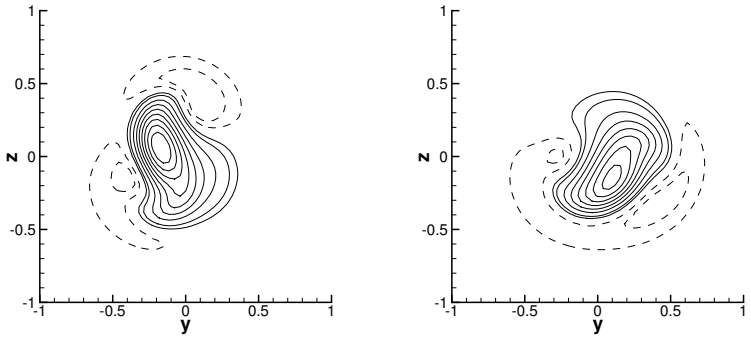

(e) $t = 18$ (f) $t = 20$

Figure 6.7: Spinning sphere at $Re = 300$, stream-wise rotation: stream-wise vorticity at $x = 3$; contours values are the same as in Fig. 6.5

6.3.3 Forces

The force $\mathbf{F}$ acting on a body can be computed with several methods. We present results generated by two of them. The first one, based on global impulse, is given by

$$\mathbf{F} = -\frac{d}{dt}\int_{\mathbb{R}^3\setminus\cup\Omega_i} \mathbf{u}\, d\mathbf{x}\,. \tag{6.3}$$

A formulation based on vorticity was derived in Section 4.5. We will note that the integral above is unbounded for a flow with a free stream. This can be easily fixed by rather considering the momentum deficit in the flow

$$\mathbf{F} = \frac{d}{dt}\int_{\mathbb{R}^3\setminus\Omega} (U_\infty \mathbf{e}_x - \mathbf{u})\; d\mathbf{x}\;. \tag{6.4}$$

The integral, once re-written in terms of vorticity, is similar to Eq. 4.44

$$\int_{\mathbb{R}^3\setminus\Omega} (U_\infty \mathbf{e}_x - \mathbf{u})\; d\mathbf{x} = -\frac{1}{2}\int_{\mathbb{R}^3\setminus\cup\Omega_i} \mathbf{x}\times\boldsymbol{\omega}\, d\mathbf{x} + \frac{1}{2}\int_{\partial\cup\Omega_i} \mathbf{x}\times(\mathbf{n}\times(U_\infty \mathbf{e}_x - \mathbf{u}))\; dS\,, \tag{6.5}$$

except for a constant term, which will not have any effect because of the time differentiation.

The second method considers the balance of momentum over a control volume (Noca et al., 1999); it was applied to the flow around a sphere by Ploumhans et al. (2002). As in this last reference, we use a spherical control volume with a radius twice that of the sphere.

Ploumhans et al. (2002) found the control volume approach to be more reliable. The other approach is based on the computation of the moments of vorticity in the whole flow and as one adds the contribution of vorticity far downstream, one uses vorticity from under-resolved regions. Moreover, this vorticity appears in differences of large terms.

Fig. 6.8 shows the drag coefficient $C_d = \frac{F_x}{\frac{1}{2}U_\infty \frac{\pi R^2}{4}}$ computed with both methods. The method based on the global impulse yields a noisier result which was filtered in our chart and tends to drift off. Past the initial transients, the control volume method

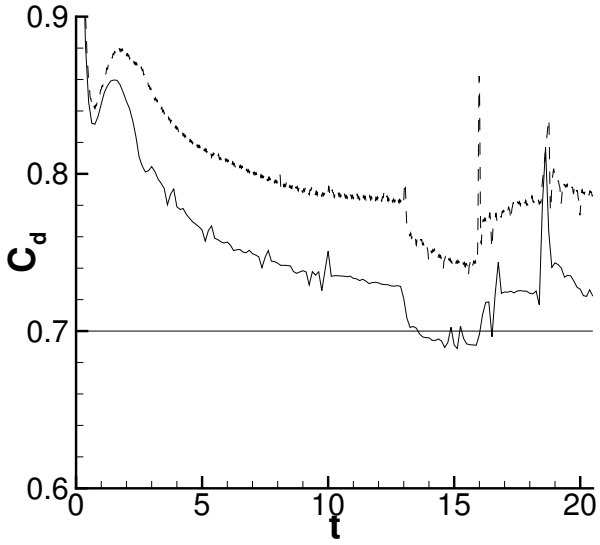

Figure 6.8: Spinning sphere at $Re = 300$, stream-wise rotation: drag coefficient C_d by the control volume (solid) and global impulse (dashed)

yields a value of ~ 0.725 for the drag coefficient; it is in agreement with the value 0.70 of Kim and Choi (2002).

The transversal force coefficients C_y and C_z (Fig. 6.9(a)) are smaller in magnitude and appear to approach a periodic behavior. Kim and Choi (2002) find that they follow the rotation of the wake structures and their norm $C_l = \sqrt{C_y^2 + C_z^2}$ is constant $= 0.025$. Our results show that we have not reached this periodic regime just yet, or that we are reaching a slightly different flow state than theirs.

6.3.4 Attachment and Separation

Fig. 6.10 shows the magnitude of wall vorticity at $t = 20$ as defined in Eq. 5.13. The quantity $\boldsymbol{\tau}/\mu = \mathbf{n} \times (\boldsymbol{\omega} - 2\mathbf{W})$ (Fig. 6.11) is perhaps more interesting as it is the actual shear up to a constant factor μ. We observe some spatial pattern in those wall quantities; its origin is the vorticity flux in the correction term of Eq. 5.13. This flux is the solution given by a panel method.

Fig. 6.11 also shows friction lines, lines tangent to the local shear; the lines were

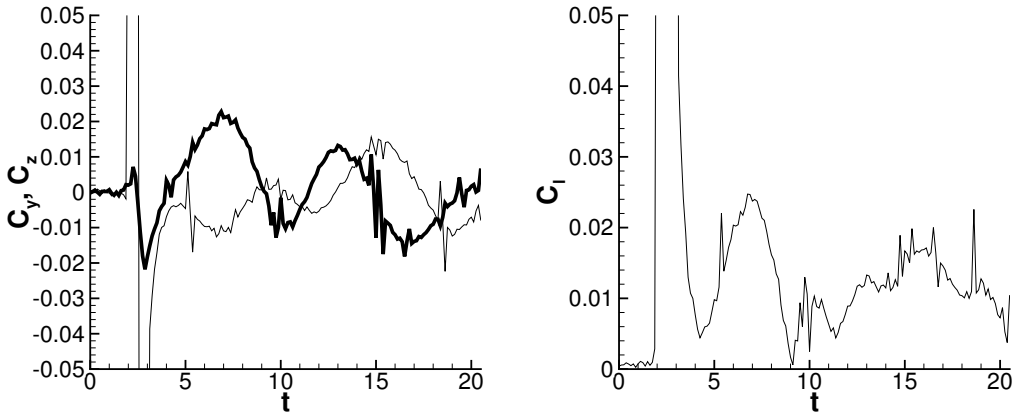

(a) C_y (bold) and C_z (plain) (b) C_l

Figure 6.9: Spinning sphere at $Re = 300$, stream-wise rotation: transversal force coefficients

seeded in the front and back of the sphere. There are two nodal points of attachment (Lighthill, 1963). One is the upstream stagnation point; the other, the reattachment point. The lines emerging from these converge to a roughly axis-symmetric separation line that we locate at $\theta \simeq 108^o$, a value close to the one of Kim and Choi (2002), 110^o. We can decompose the shear into its azimuthal and axial components

$$\tau_\phi = \tau_y \sin(\phi) - \tau_z \cos(\phi) \tag{6.6}$$

$$\tau_\theta = \tau_x \sin(\theta) - \cos(\theta)(\tau_y \cos(\phi) + \tau_z \sin(\phi)) \,. \tag{6.7}$$

Both components (Fig. 6.12 and 6.13) exhibit a difference in magnitude between the front and the back of the sphere. The flow in the recirculation region is slower and has acquired a certain amount of swirl (azimuthal velocity), thus reducing the corresponding shear component.

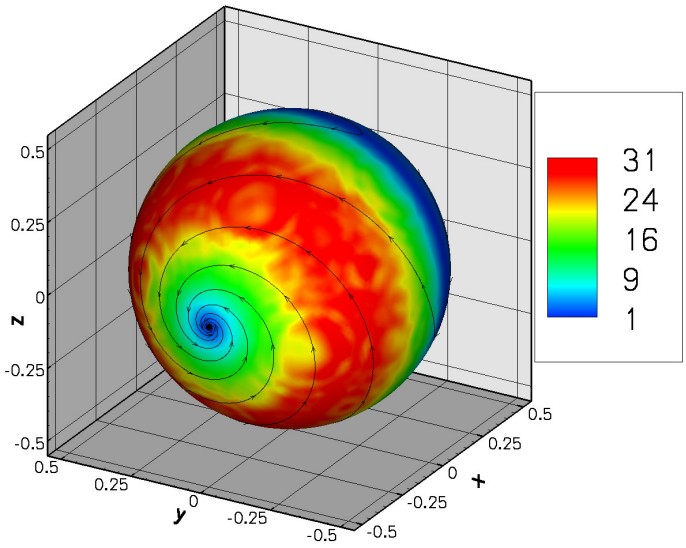

(a) Front

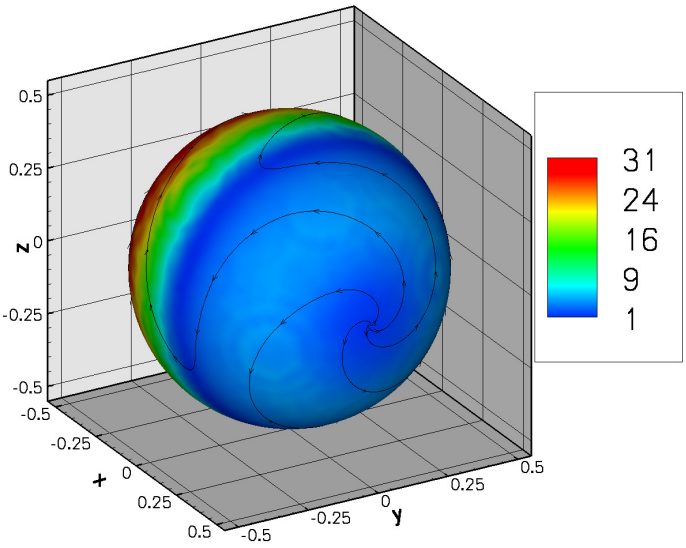

(b) Back

Figure 6.10: Spinning sphere at $Re = 300$, stream-wise rotation: wall vorticity and lines at $t = 20$

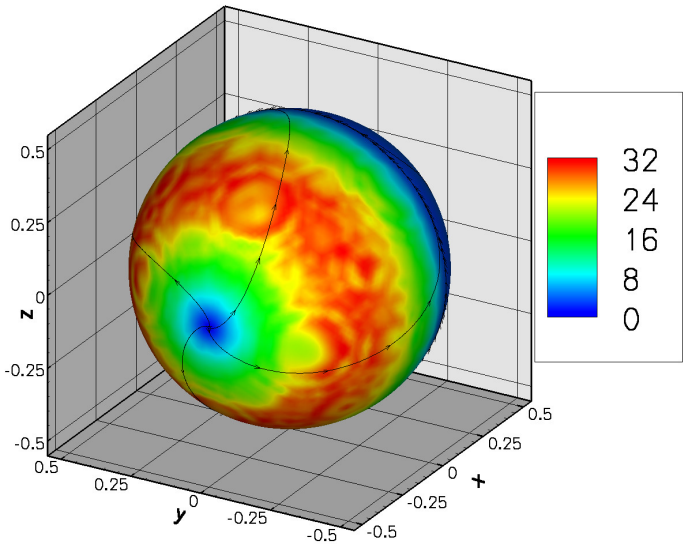

(a) Front

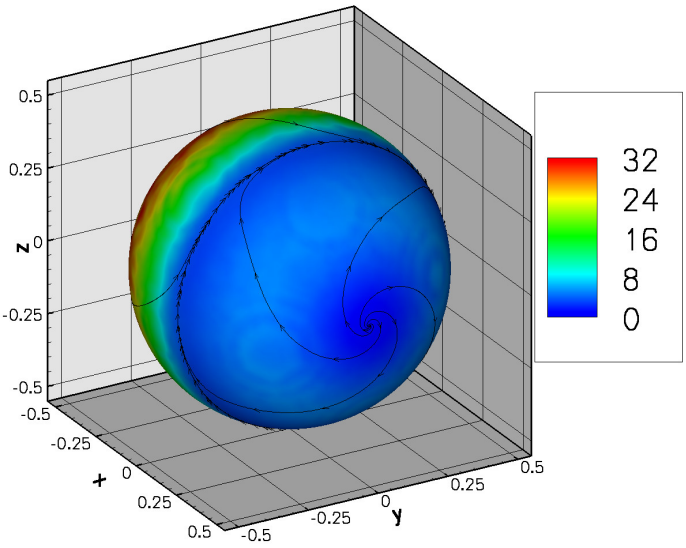

(b) Back

Figure 6.11: Spinning sphere at $Re = 300$, stream-wise rotation: shear and lines at $t = 20$

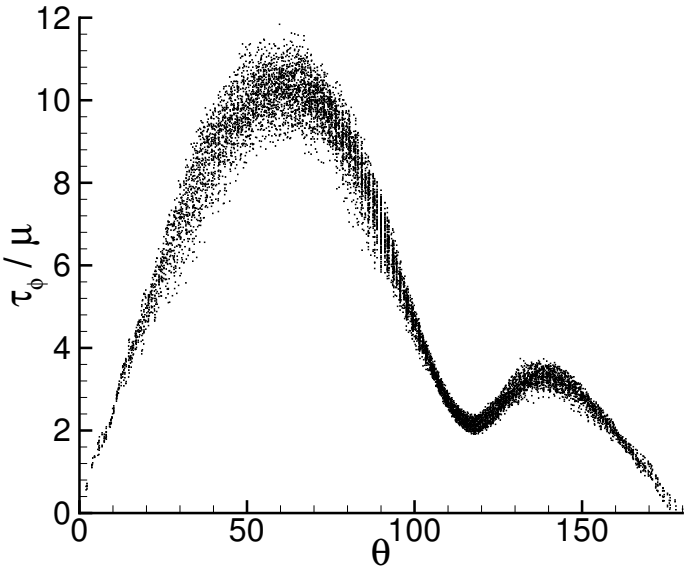

Figure 6.12: Spinning sphere at $Re = 300$, stream-wise rotation: azimuthal shear magnitude at $t = 20$

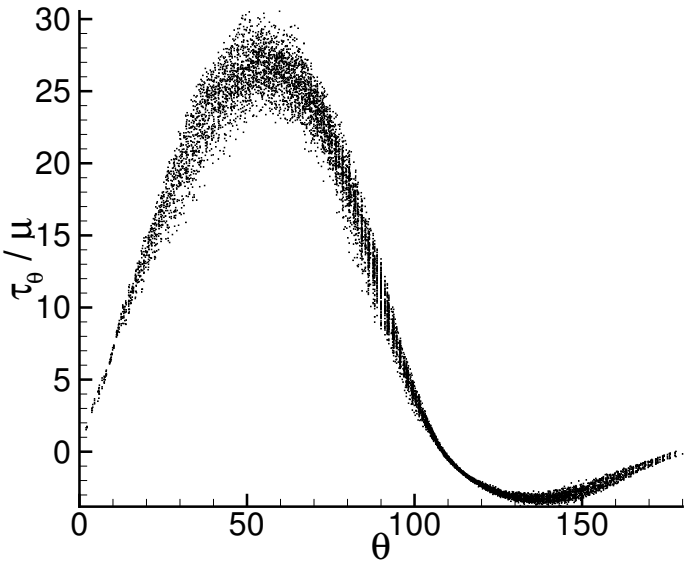

Figure 6.13: Spinning sphere at $Re = 300$, stream-wise rotation: axial shear magnitude at $t = 20$

R_0	0.5
m	700
center	-2 0 0

Table 6.2: Spherical mapping parameters

6.4 Transverse Rotation

In this case, $\mathbf{W} = \mathbf{e}_y$. The wall thus moves in the direction of the free-stream for $z > 0$ and against it for $z < 0$.

6.4.1 Numerics

This simulation was started using the same geometry and numerical parameters as in Section 6.4. At $t = 9.5$, the simulation was stopped and a spherical mapping was used for the redistributions from then on. This is the same mapping as in Ploumhans et al. (2002); its parameters are reproduced in Table 6.2. The resolution of the spherical mapping decreases rapidly with distance from the sphere. This made the simulation more affordable for longer times (Fig. 6.14). The mesh Reynolds number (Fig. 6.14(b)) jumps from 2.7 to 5 because the wake vorticity structures are re-sampled onto a coarser lattice.

6.4.2 Wake

The wake of a non-spinning sphere at $Re = 300$ is unsteady and asymmetric (Johnson and Patel, 1999, Ploumhans et al., 2002, Kim and Choi, 2002). The sphere indeed starts to sustain a small amount of lift and the shed periodic hairpin structures show a bias in the direction of this lift. Because of its rotation, the present configuration develops more lift and increases the bias. The $Q = 0$ surfaces in Fig. 6.15 and 6.16 give a overview of the shedding cycle of this flow. We will refer to the downwash-inducing vortex pair as the main pair since it corresponds to the lift. We will call the upwash-inducing one the secondary pair.

The period of this flow is $T \simeq 4.5$ and the Strouhal frequency $St_{\omega^\star=0.5} \simeq \frac{2R}{U_\infty T} = 0.22$. Those are values to compare to the frequency of a non-spinning sphere $St^{\perp}_{\omega^\star=0} = 0.136 \pm 0.002$ (Johnson and Patel, 1999, Ploumhans et al., 2002, Kim and Choi, 2002) and the rotation frequency $\frac{W}{2\pi} = 0.159$.

Fig. 6.17 and 6.18 give a closer view of the shedding of those structures. We plot transparent surfaces of $Q = 0$ and vortex lines in a $y > 0$ region near the sphere. We seed vortex lines on the surface at locations that follow the sphere rotation; more precisely,

$$x_i = R\cos(\pi/4)\cos(\psi(t) + i\pi/3)$$
$$y_i = R\sin(\pi/4)$$
$$z_i = R\cos(\pi/4)\sin(\psi(t) + i\pi/3)$$

where $i = 0 \cdots 5$ and $\psi(t) = -Wt$. Vorticity is subjected to diffusion; the vortex lines are therefore not material lines. The lines appear to be redirected abruptly; some of those events actually correspond to vortex reconnections and pinch-off which is crucial during vortex shedding.

The bottom separation (discussed below) feeds a large vorticity structure over the shedding cycle. If we consider the section of this structure in the longitudinal plane, we see that a kink appears between 0 and $T/3$ and is the early sign of the pinch off ($5T/6$). The shed structure can be seen to be the tip of a newly formed downwash-inducing hairpin vortex. The vortex lines inside the tails of the hairpin are seen to be originating from the sides of the sphere ($T/2 \rightarrow 5T/6$). As the tip is convected downstream, the tails are stretched and brought close to each other and to the next hairpin tip. Viscous diffusion eventually connects the tails to each other and to the hairpin structure of the following cycle ($0 \rightarrow T/4$, bottom right corner).

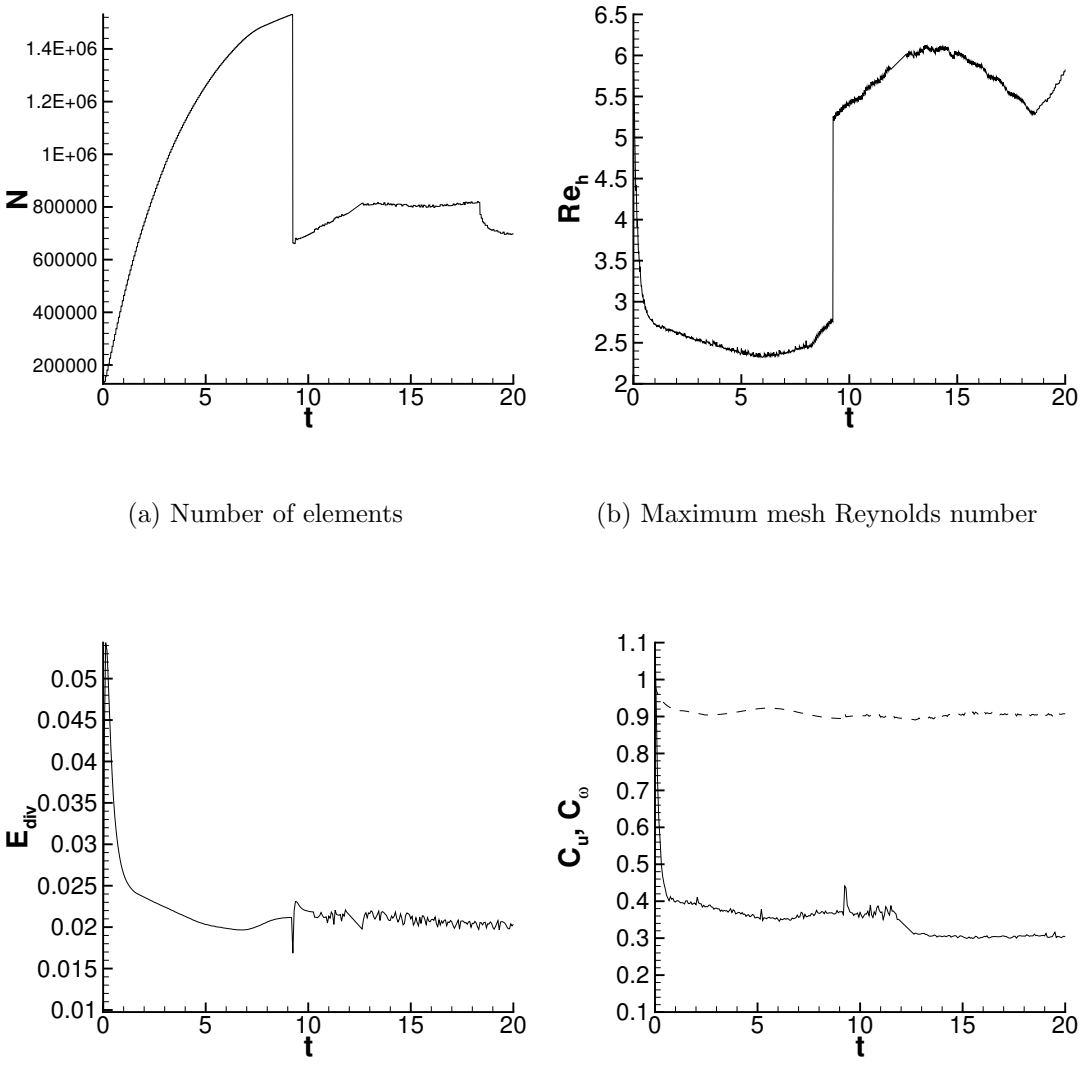

(a) Number of elements

(b) Maximum mesh Reynolds number

(c) Divergence error

(d) Courant number, vorticity expression (solid) and velocity expression (dashed)

Figure 6.14: Spinning sphere at $Re = 300$, transverse rotation: numerical diagnostics

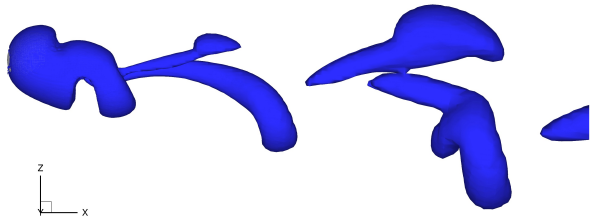

(a) 0

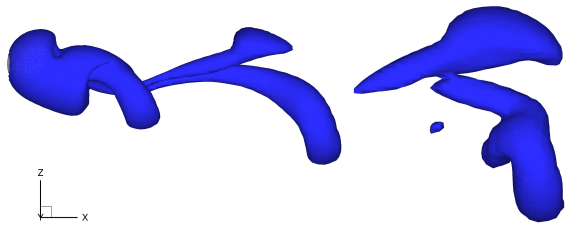

(b) $T/4$

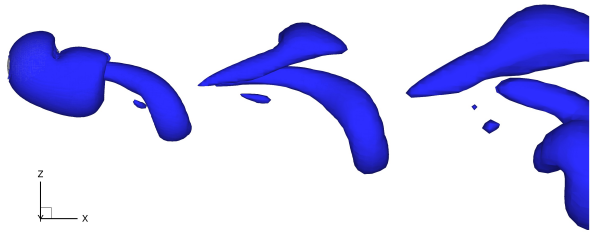

(c) $T/2$

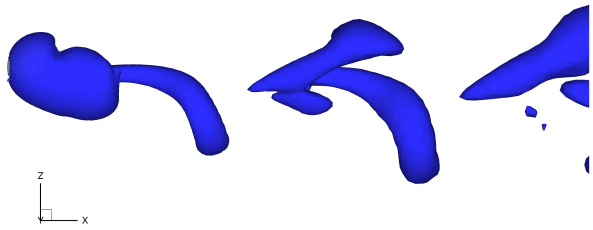

(d) $3T/4$

Figure 6.15: Spinning sphere at $Re = 300$, transverse rotation: shedding cycle, $Q = 0$ iso-surface, side view

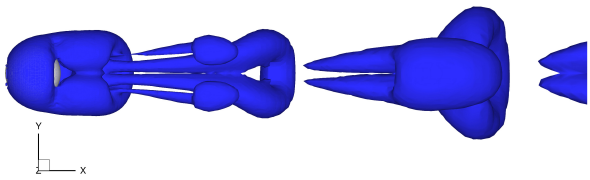

(a) 0

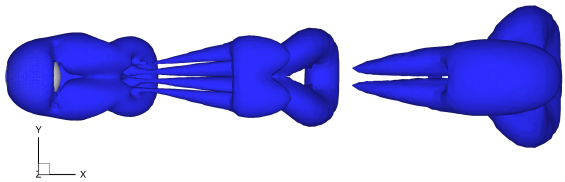

(b) $T/4$

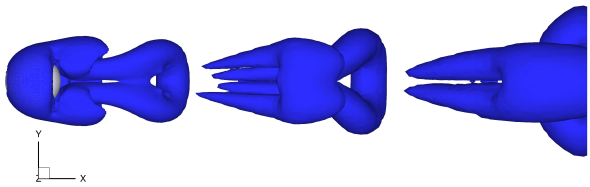

(c) $T/2$

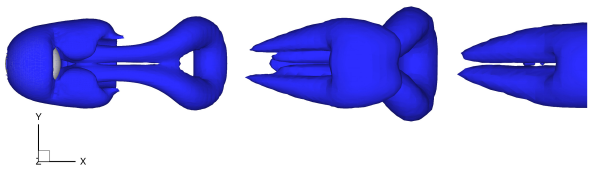

(d) $3T/4$

Figure 6.16: Spinning sphere at $Re = 300$, transverse rotation: shedding cycle, $Q = 0$ iso-surface, top view

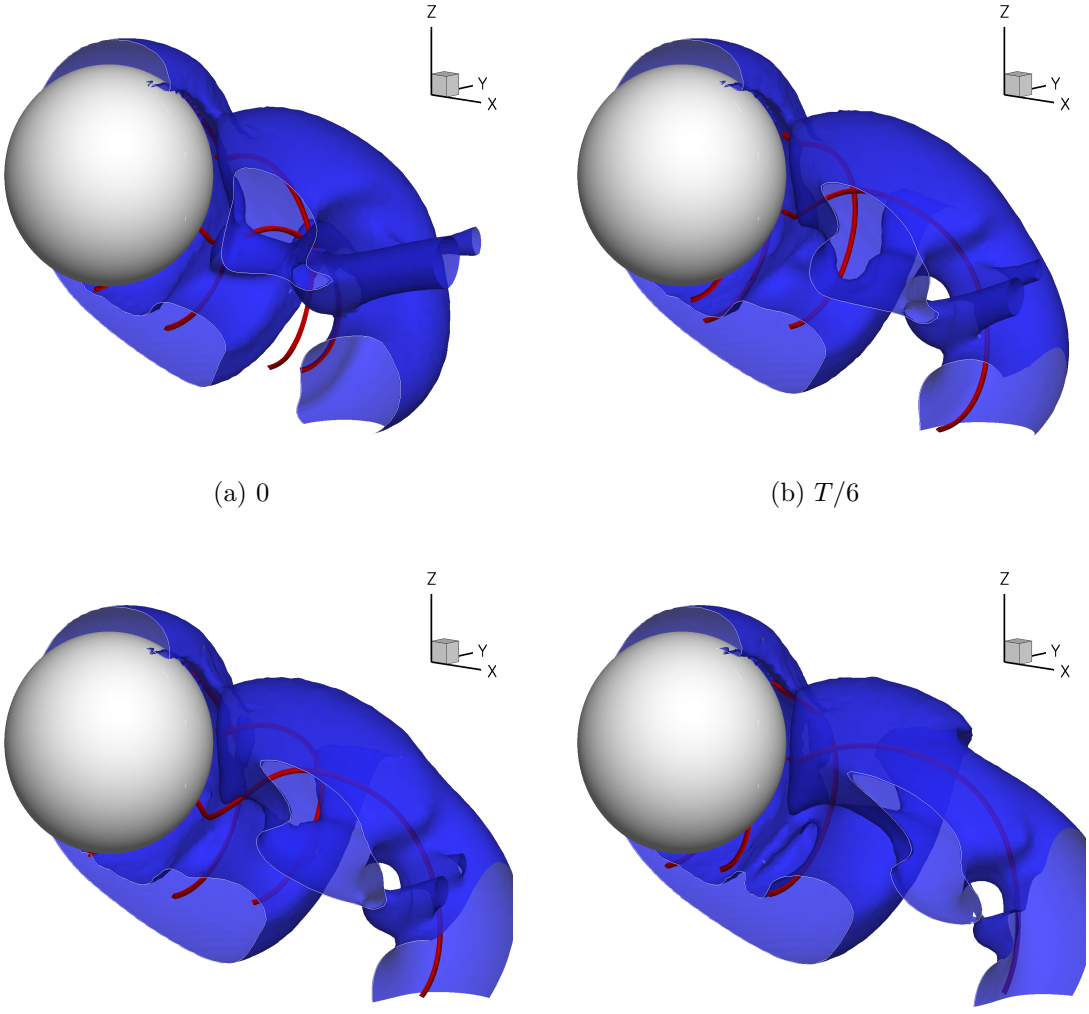

(a) 0 (b) $T/6$

(c) $T/4$ (d) $T/3$

Figure 6.17: Spinning sphere at $Re = 300$, transverse rotation: shedding cycle, $Q = 0$ iso-surface and vorticity lines

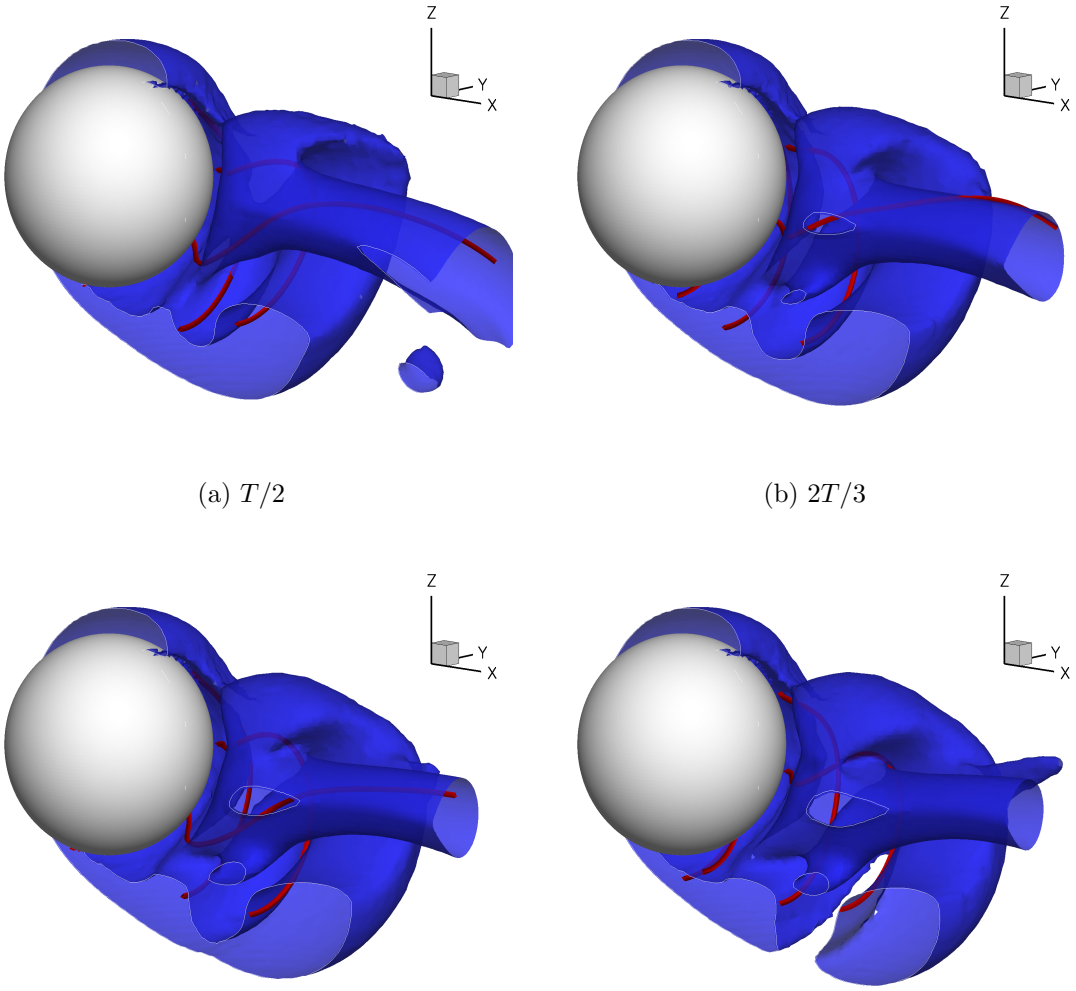

(a) $T/2$

(b) $2T/3$

(c) $3T/4$

(d) $5T/6$

Figure 6.18: Spinning sphere at $Re = 300$, transverse rotation: shedding cycle, $Q = 0$ iso-surface and vorticity lines (continued)

6.4.3 Forces

The history of the force coefficients is plotted in Fig. 6.19. They were computed using the control volume approach. We do note an abrupt transition around the time we changed the redistribution lattice.

The force coefficients are not yet showing periodicity in time. If indeed the flow and the forces remain periodic for large times, the average force coefficients can be computed for the last cycle of the simulation between $t \simeq 15.5$ and 20. We obtain $\overline{C_d} = 0.81$ and $\overline{C_l} = 0.4$; the ratio of these coefficients is then $\overline{C_l}/\overline{C_d} = 0.49$.

We can compare those values to previous correlations or analytical results that cover a wide range of conditions. For small Reynolds numbers first, Rubinow and Keller (1961) considered a Stokes expansion and found that

$$\begin{aligned} C_l &\simeq 2\,\omega^\star(1 + O(Re)) \\ C_d &\simeq 12\,Re^{-1}(1 + \frac{3}{8}Re + o(Re)) \,, \end{aligned}$$

which in our case would yield $C_l = 1$ and $C_d = 4.54$. This is not unexpected as we are quite far from $Re < 1$.

The work of Bearman and Harvey (1976), Barkla and Auchterlonie (1971), Maccoll (1928) concerned flows where $10^3 < Re < 10^5$ and involved, in some cases, not spheres but actual golf balls. We will not try to use their results, but rather, consider more recent work which focused on intermediate Re. Tsuji et al. (1985) proposed

$$\begin{aligned} C_l &\simeq (0.4 \pm 0.1)\omega^\star \\ C_d &\simeq K_1 + \frac{K_2}{Re} + \frac{K_3}{Re^2} \,. \end{aligned}$$

The second expression assumes no effect of the rotation rate and showed good agreement over their experimental range, $550 < Re < 1600$ and $\omega^\star < 0.7$; the constants K_1, K_2 and K_3 are adjusted according to the Reynolds number. In our case, this yields $C_l \simeq 0.2 \pm 0.05$ and $C_d \simeq 0.66$. More recently, Oesterlé and Bui Dinh (1998)

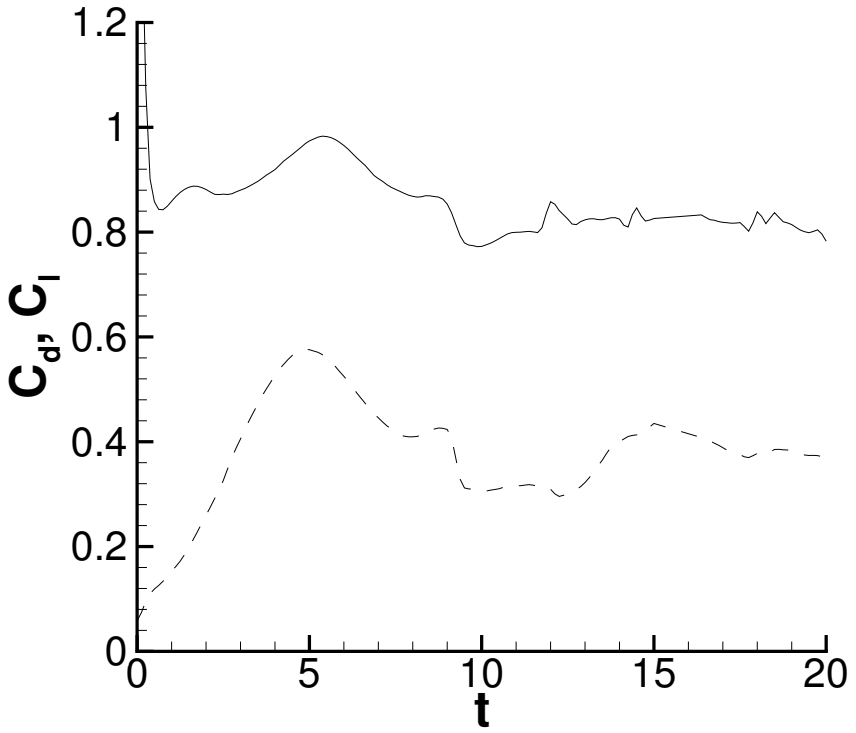

Figure 6.19: Spinning sphere at $Re = 300$, transverse rotation: drag coefficient C_d (solid) and lift coefficient C_l (dashed)

proposed

$$C_l \simeq 0.45 + (2\omega^\star - 0.45)e^{-0.075\,\omega^{\star 0.4} Re^{0.7}}$$

for the ranges, $10 < Re < 140$ and $1 < \omega^\star < 6$. This expression gives $C_l \simeq 0.475$ for the present case.

6.4.4 Attachment and Separation

Fig. 6.20 and 6.21 show the magnitude of the skin friction along with skin friction lines for several instants during a shedding cycle. The lines emerge from a first node which remains located at $\phi = 0^o$, $\theta = 14^o$. At all times during a cycle, the lines converge into a second node on the top of the sphere which does move by a few degrees around its average position at $\phi = 0$, $\theta = 110^o$.

The skin friction lines describe the velocity field relative to the wall at a small distance above it. The two skin friction nodes therefore correspond to stagnation points in a frame rotating with the sphere (Fig. 6.23). Moreover, because these two points are stationary in the laboratory frame, they must be moving in the rotating frame. In effect, from the perspective of the sphere, there is one attachment point and one separation point, both moving at a velocity WR in the $y = 0$ plane of the sphere.

In the laboratory frame, the flow does, however, have a separation near the bottom of the sphere (Fig. 6.22). The separation line stands some distance from the wall; Fig. 6.25 shows the region of its intersection with the $y = 0$ plane. It is relatively difficult to locate accurately the separation point. It is a saddle point, and moreover its eigenvectors form a very narrow angle (Fig. 6.24). If we take this into consideration, we can give a rough estimate of the position of this point which moves very little over a shedding period, $x \simeq -0.55R$, $y \simeq -0.87R$, and corresponds to a distance from the center of the sphere $r = 1.03R$, and angles $\theta \simeq 56^o$, $\phi = 180^o$. An estimation of the rest of the line is given in Appendix F.2.

Similarly, the stagnation point does not lie on the surface of the sphere. Fig. 6.26 gives an estimation of its position by considering the streamlines in a $y = 0$ plane (Fig. 6.26(a)) and projected streamlines in an oblique slice (Fig. 6.26(b)).

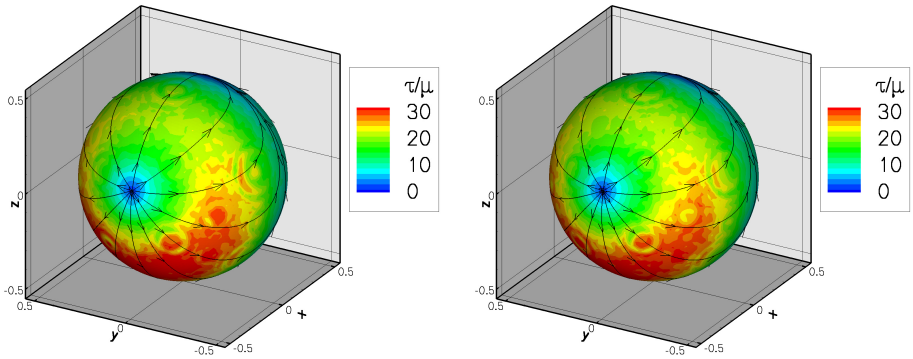

(a) $t = 15$ (b) $t = 16$

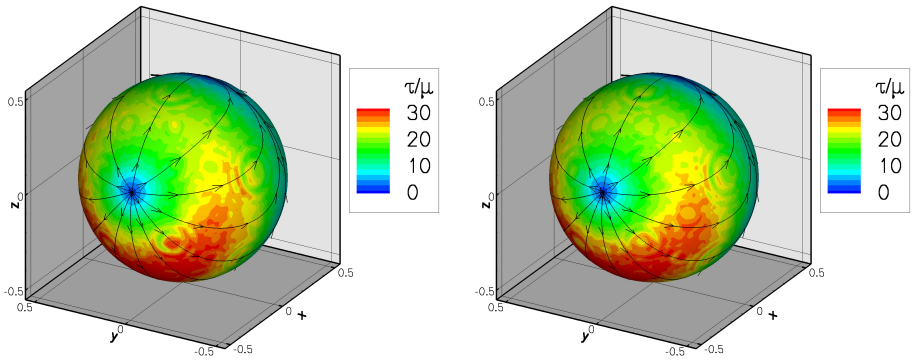

(c) $t = 17$ (d) $t = 18$

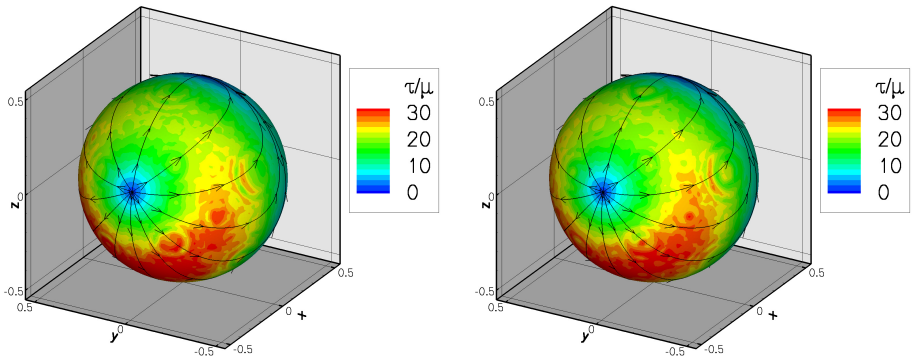

(e) $t = 19$ (f) $t = 20$

Figure 6.20: Spinning sphere at $Re = 300$, transverse rotation: skin friction magnitude and lines, front view

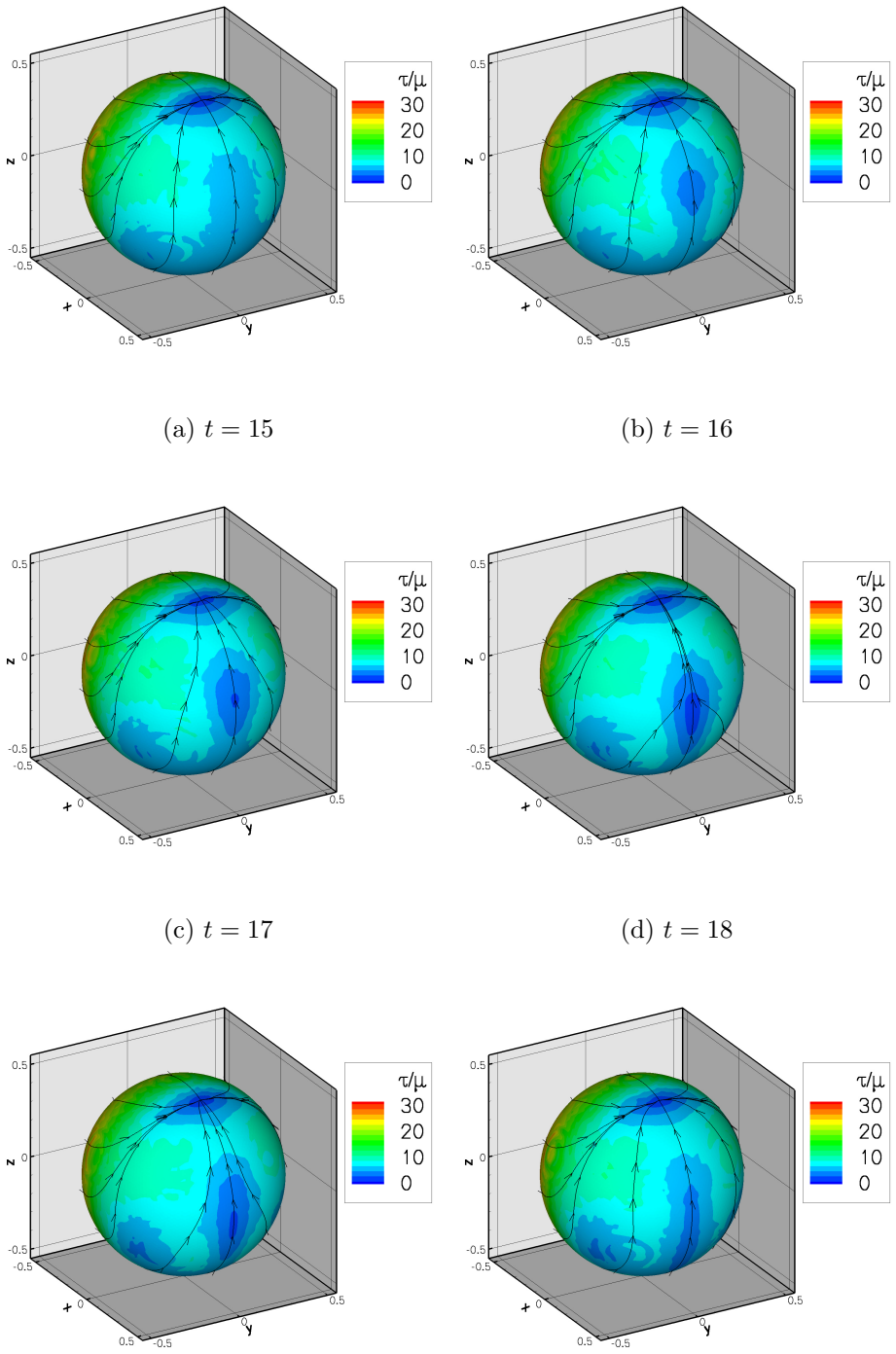

(a) $t = 15$ (b) $t = 16$

(c) $t = 17$ (d) $t = 18$

(e) $t = 19$ (f) $t = 20$

Figure 6.21: Spinning sphere at $Re = 300$, transverse rotation: skin friction magnitude and lines, back view

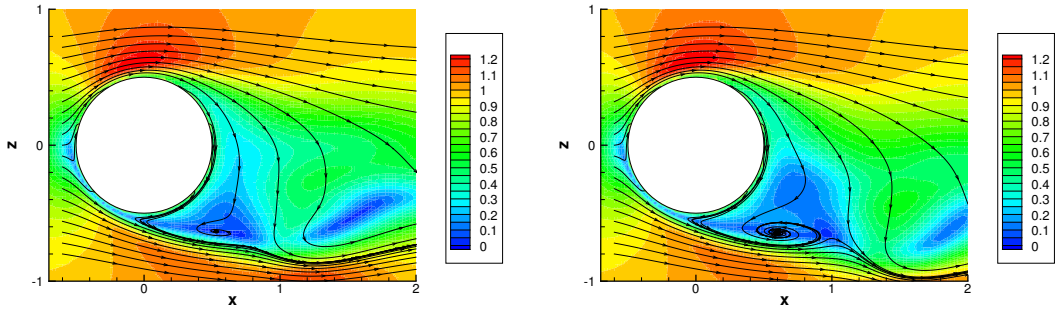

(a) $t = 15$ (b) $t = 16$

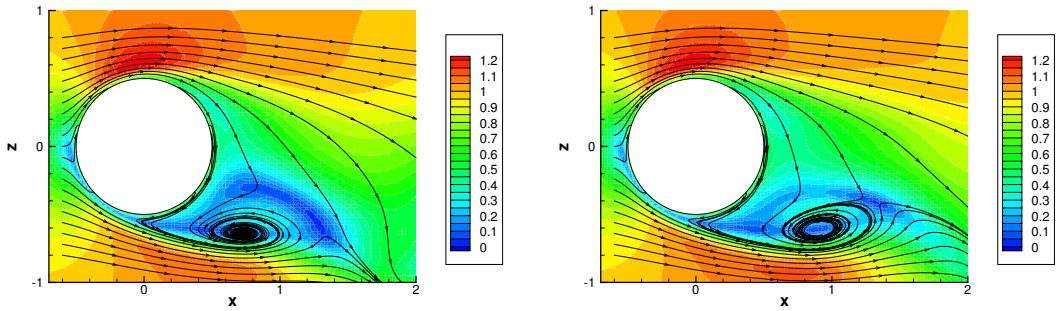

(c) $t = 17$ (d) $t = 18$

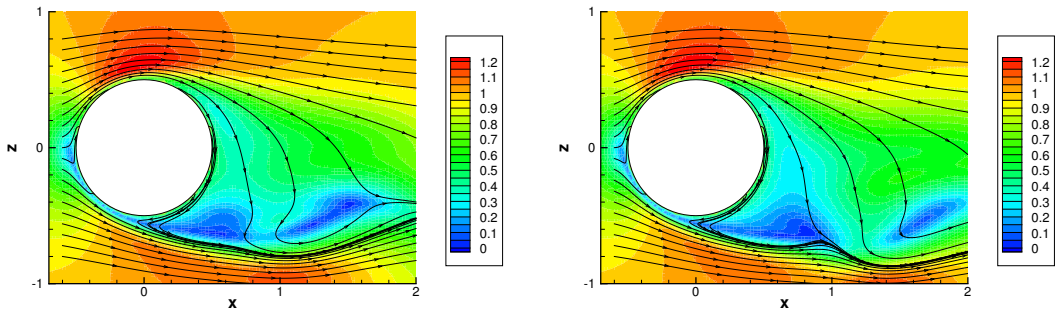

(e) $t = 19$ (f) $t = 20$

Figure 6.22: Spinning sphere at $Re = 300$, transverse rotation: velocity magnitude and streamlines in the $y = 0$ plane

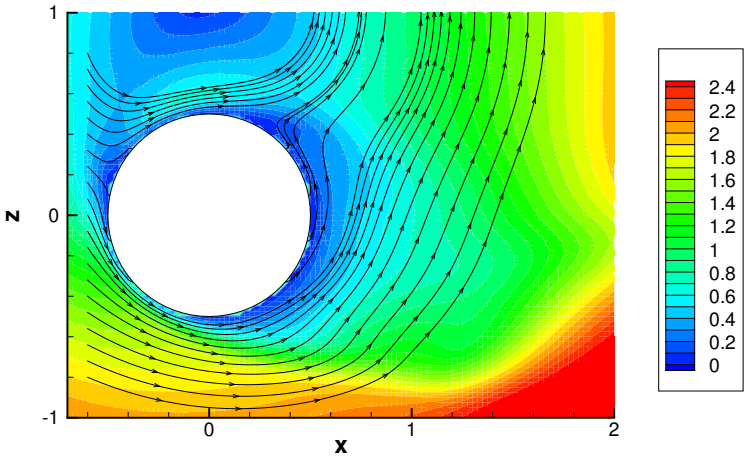

Figure 6.23: Spinning sphere at $Re = 300$, transverse rotation: velocity magnitude and streamlines in a frame rotating with the sphere, in the $y = 0$ plane at $t = 20$

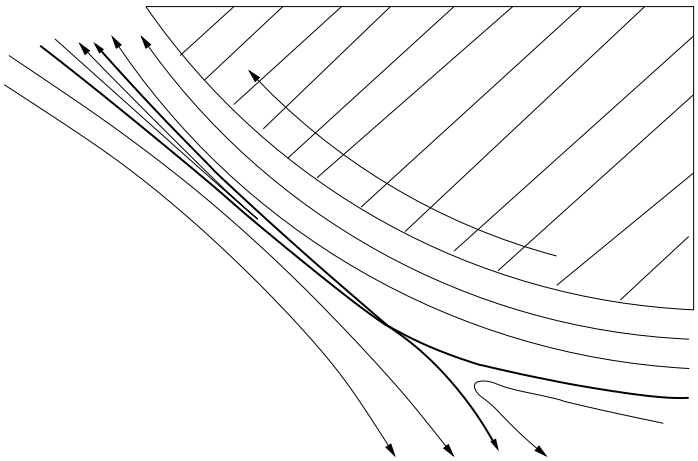

Figure 6.24: Spinning sphere at $Re = 300$, transverse rotation, bottom separation: localization of the saddle point

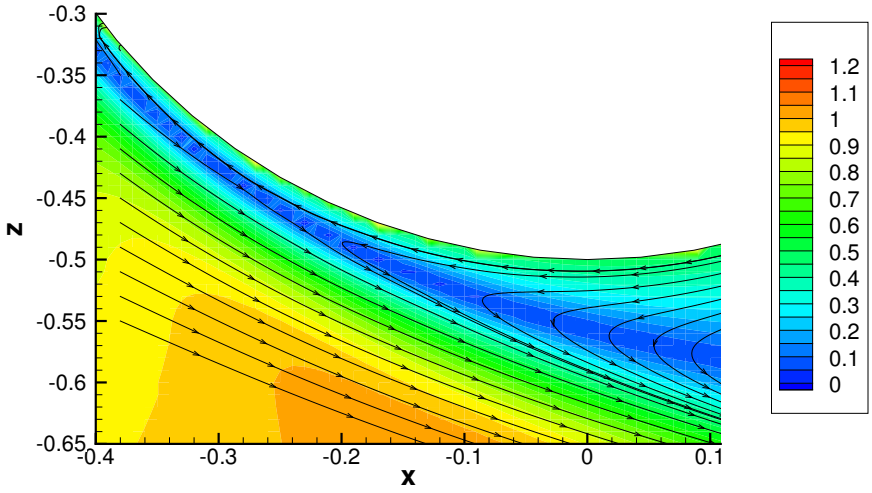

Figure 6.25: Spinning sphere at $Re = 300$, transverse rotation: velocity magnitude and streamlines in the $y = 0$ plane at $t = 20$, separation region

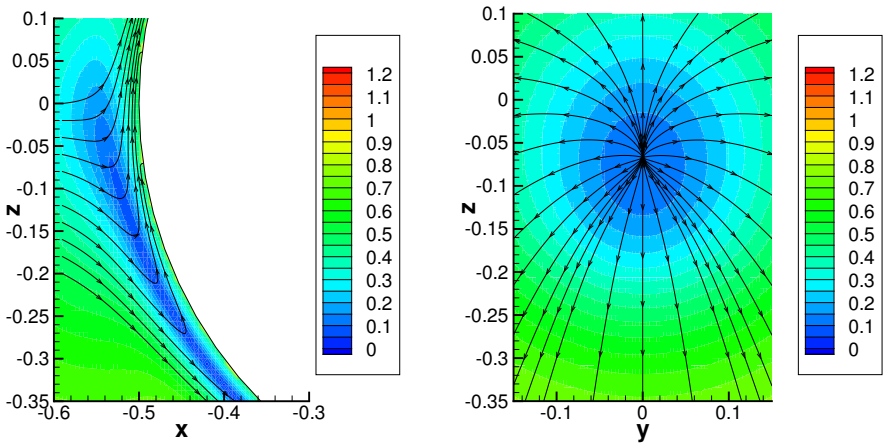

(a) velocity magnitude and streamlines in the $y = 0$ plane

(b) velocity magnitude and projected streamlines in the $0.98x + 0.18z = -0.56$ plane

Figure 6.26: Spinning sphere at $Re = 300$, transverse rotation: stagnation region at $t = 20$

6.5 Oblique Rotation

In this last case, the angular velocity is set to $\mathbf{W} = W\frac{\sqrt{2}}{2}(\mathbf{e}_x + \mathbf{e}_y)$. It loses most symmetries of the previous configurations. As a result, it is more difficult to investigate.

6.5.1 Numerics

This simulation used a spherical mapping from the start. The parameters are identical to those of Section 6.4. It also used a coarser mesh for the representation of the sphere (5120 triangles). As seen in Fig. 6.27, the only outstanding features are in the number of particles and the mesh Reynolds number plots. At $t = 12.5$, a more aggressive approach was adopted for the elimination of the weak elements in the wake. This had no or little repercussion on the other diagnostics. As in the previous cases, Re_h exhibits a growth by stages, as structures are convected into coarser regions of the redistribution lattice.

6.5.2 Wake

Fig. 6.28 and 6.29 show the different stages of a shedding cycle. The wake shares some features with the one of Section 6.4. One recognizes in particular the hairpin structures, which are this time wrapped around each other.

The shedding appears to have a period of $T \simeq 5$, which corresponds to a Strouhal frequency $St^{\angle}_{\omega^\star=0.5} \simeq 0.2$ Fig. 6.30 and 6.31 offer a closer perspective on the periodic shedding of this flow. As in the transverse case, we seed vorticity lines from points that rotate with the sphere. In this case, we added a point on the axis of rotation at $\theta = 135^o$, $\phi = 90^o$. Because the flow is not symmetric, we only hide the region $y < -0.4R$. A striking feature of the near wake is its similarity to the stream-wise rotation case of Section 6.3. It indeed consists in a main $\omega_x > 0$ filament which interacts with peripheral $\omega_x < 0$ structures.

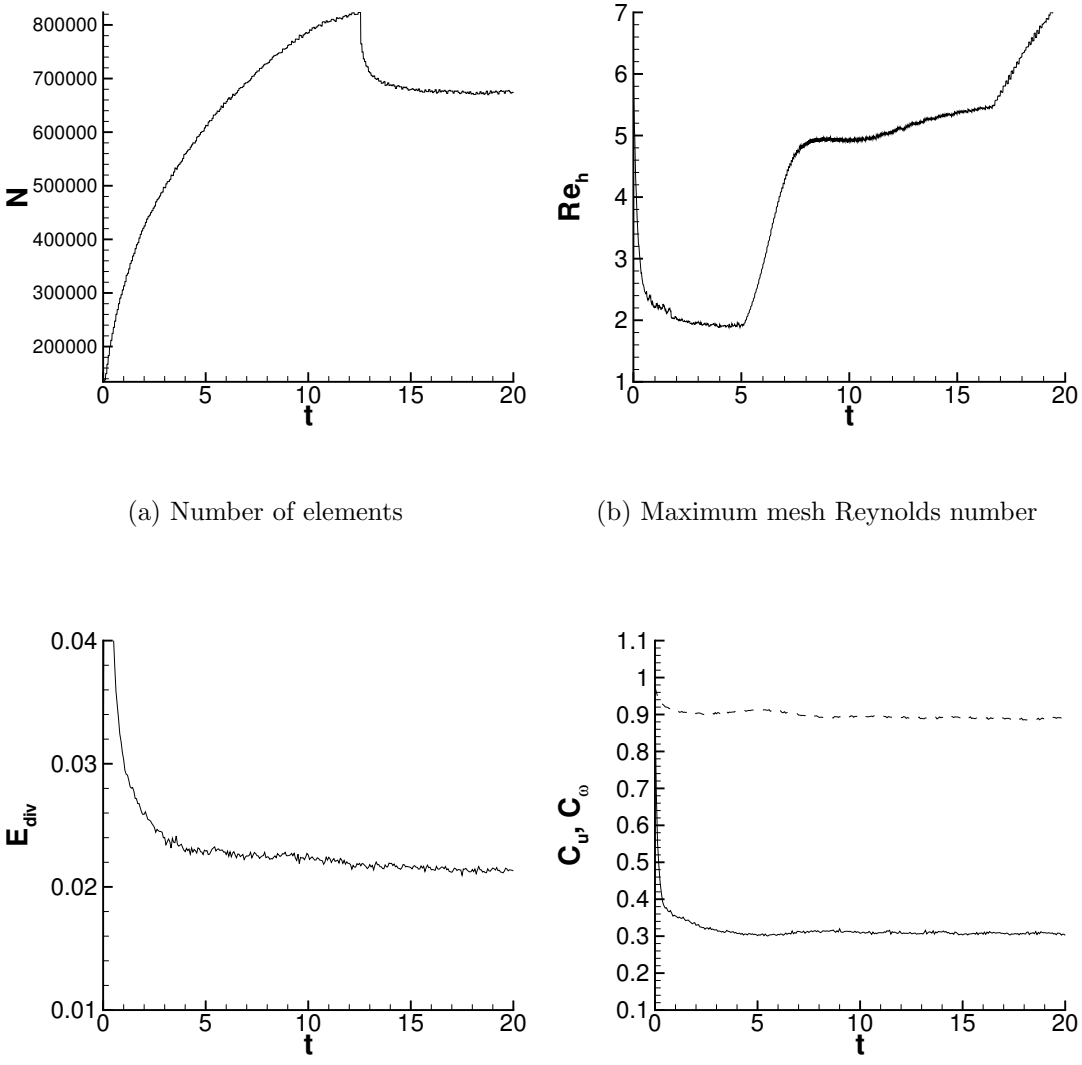

(a) Number of elements

(b) Maximum mesh Reynolds number

(c) Divergence error

(d) Courant number, vorticity expression (solid) and velocity expression (dashed)

Figure 6.27: Spinning sphere at $Re = 300$, oblique rotation: numerical diagnostics

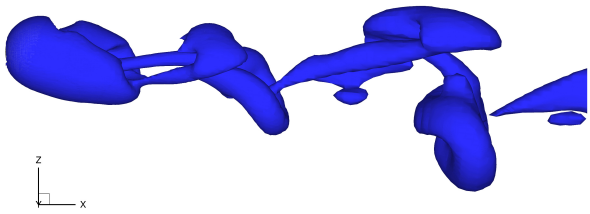

(a) 0

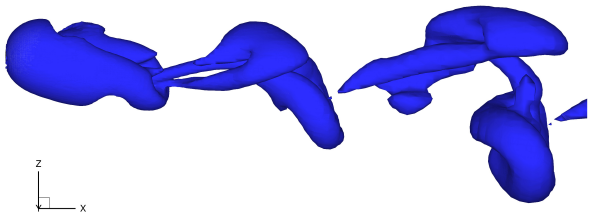

(b) $T/4$

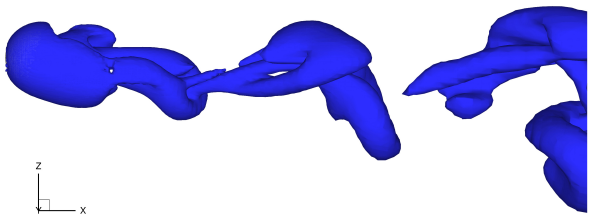

(c) $T/2$

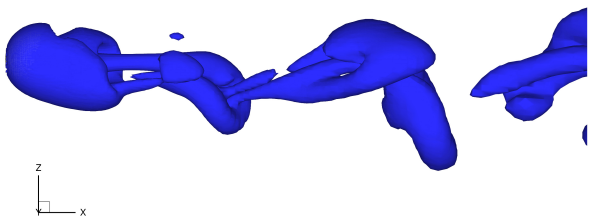

(d) $3T/4$

Figure 6.28: Spinning sphere at $Re = 300$, oblique rotation: shedding cycle, $Q = 0$ iso-surface, side view

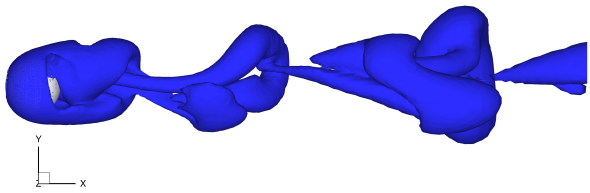

(a) 0

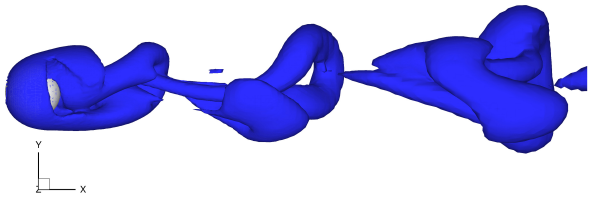

(b) $T/4$

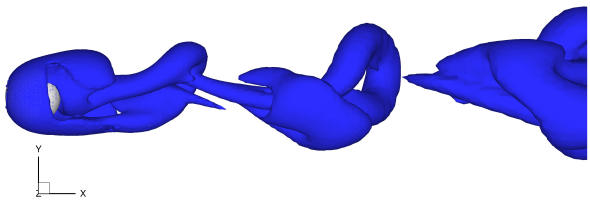

(c) $T/2$

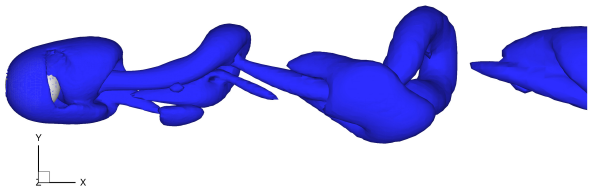

(d) $3T/4$

Figure 6.29: Spinning sphere at $Re = 300$, oblique rotation: shedding cycle, $Q = 0$ iso-surface, top view

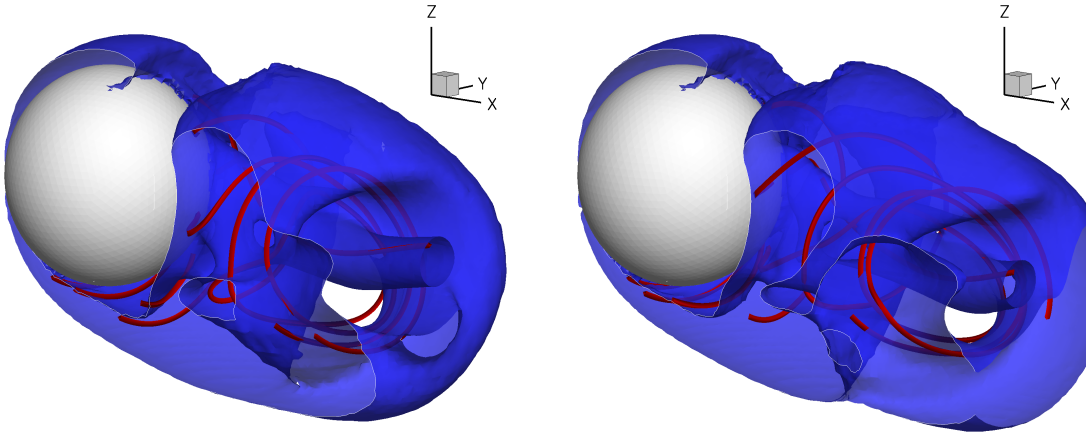

(a) 0 (b) $T/8$

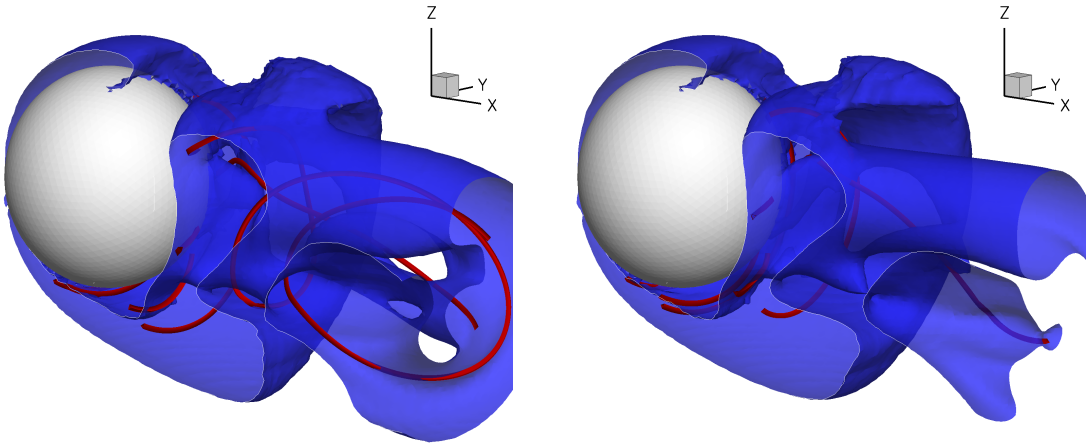

(c) $T/4$ (d) $3T/8$

Figure 6.30: Spinning sphere at $Re = 300$, oblique rotation: shedding cycle, $Q = 0$ iso-surface and vorticity lines

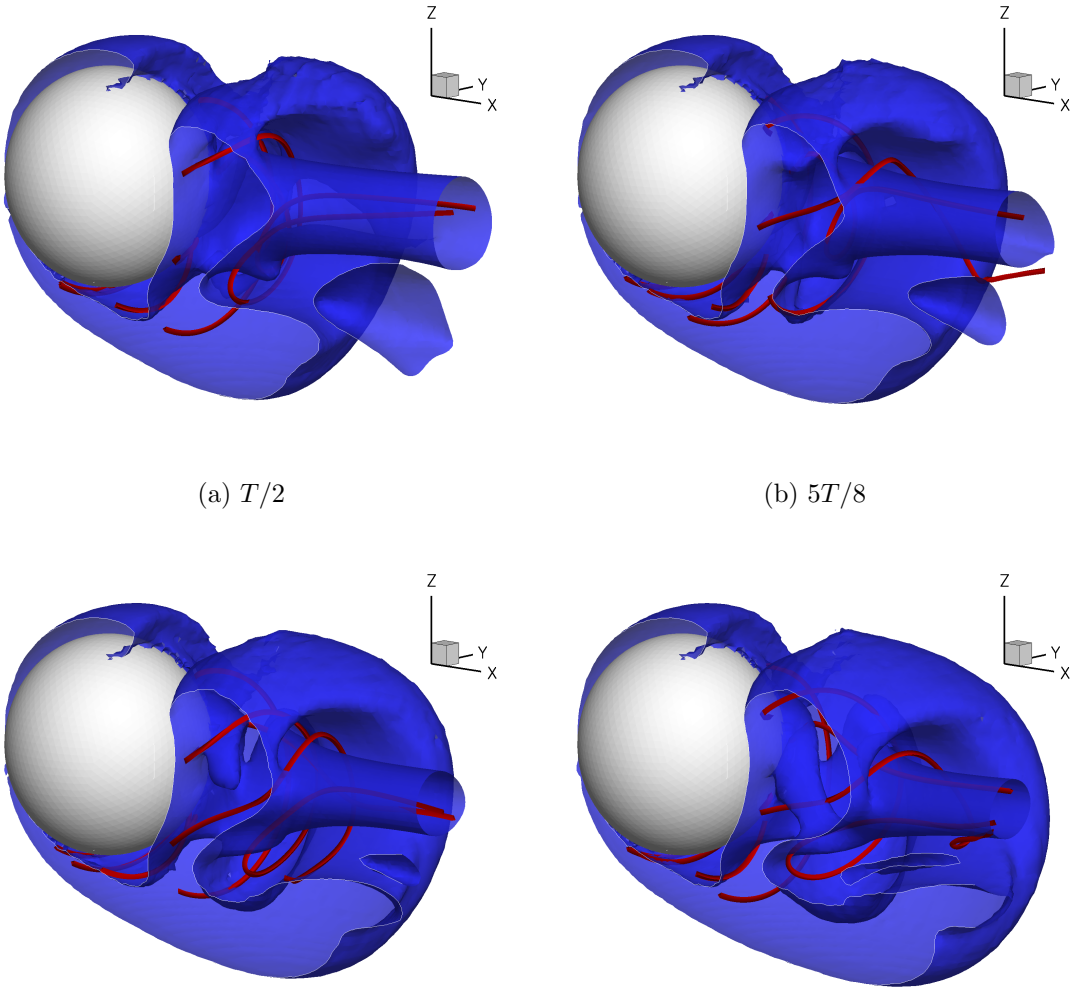

(a) $T/2$

(b) $5T/8$

(c) $3T/4$

(d) $7T/8$

Figure 6.31: Spinning sphere at $Re = 300$, oblique rotation: shedding cycle, $Q = 0$ iso-surface and vorticity lines (continued)

6.5.3 Forces

The force coefficients are plotted in Fig. 6.32. During the last shedding cycle of our simulation, the drag coefficients have nearly adopted a periodic behavior around the average values $\overline{C_d} \simeq 0.76$, $\overline{C_z} \simeq 0.26$ and $\overline{C_y} \simeq -0.165$. We note that the drag coefficient is between the stream-wise and transverse values and that interestingly enough, lift has been decreased proportionally to the amount of transverse angular velocity, $C_z^{\angle} \simeq \frac{\sqrt{2}}{2} C_z^{\perp} = 0.28$.

There is a non-zero transverse force C_y. This component manifests itself in our plot of the wake (Fig. 6.29), where the structures appear to have a positive y self-induced velocity.

The ratio between the lateral force and the drag is $\sqrt{\overline{C_y}^2 + \overline{C_z}^2}/\overline{C_d} = 0.41$. This value is lower than in the case of the transverse rotation; the decrease in drag, C_d and the transverse force, C_y are not large enough to compensate for the drop in C_z.

6.5.4 Attachment and Separation

The skin friction lines have four critical points in this configuration. There is one attachment node in the front of the sphere. Its location is fairly constant during a cycle, $\phi \simeq -14^o$, $\theta \simeq 9.5^o$. All the friction lines converge into a separation node at $\phi \simeq 14.5^o$, $\theta \simeq 106^o$. The last two points were not present on the transverse case. There is an attachment node at $\phi \simeq 133^o$, $\theta \simeq 113^o$ which does move by a few degrees during a cycle, and a saddle which remains at $\phi \simeq 103^o$, $\theta \simeq 106^o$.

As discussed in Section 6.4.4, all of these critical points do not lie on the axis of rotation of the sphere and correspond to attachments and separations in a rotating frame. The critical points and lines for the laboratory frame are at some distance in the flow. Appendix F.3 presents some additional results for the separation line.

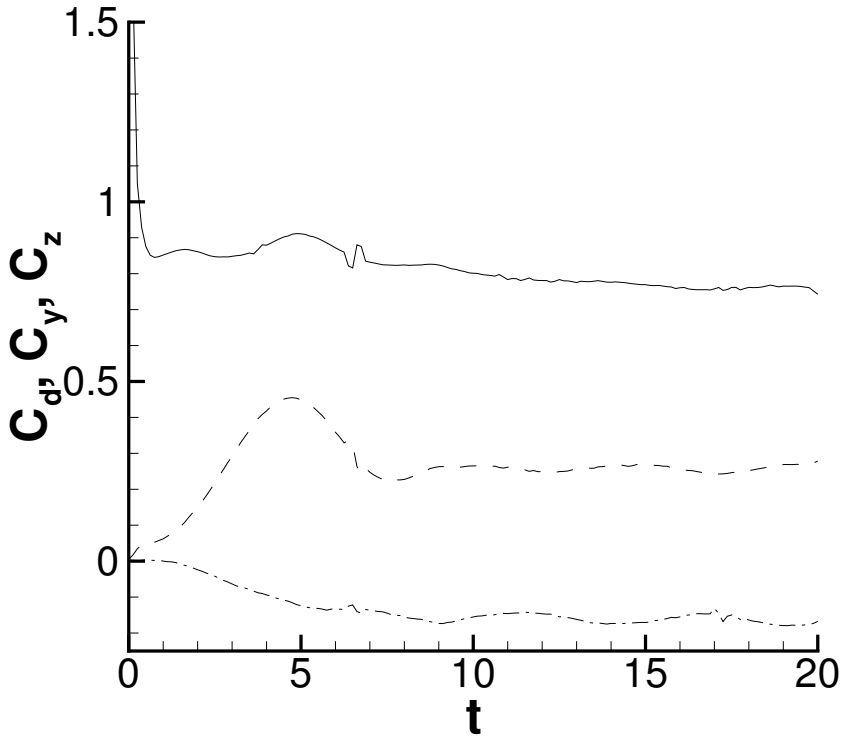

Figure 6.32: Spinning sphere at $Re = 300$, oblique rotation: drag coefficient C_d (solid), lift coefficient C_z (dashed) and transverse force coefficient C_y (dash-dotted)

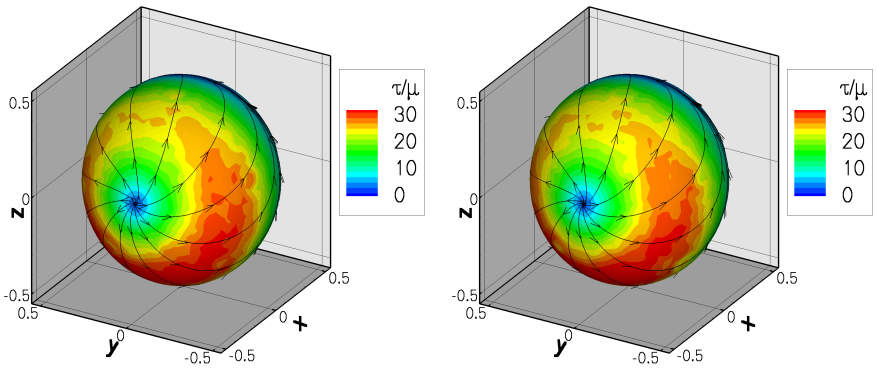

(a) $t = 15$ (b) $t = 16$

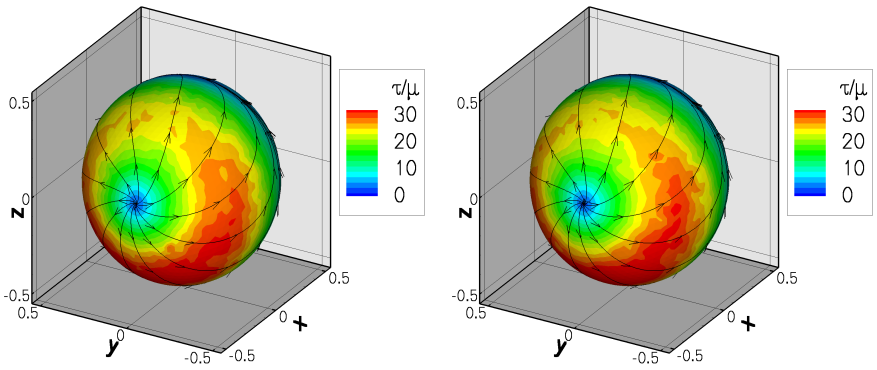

(c) $t = 17$ (d) $t = 18$

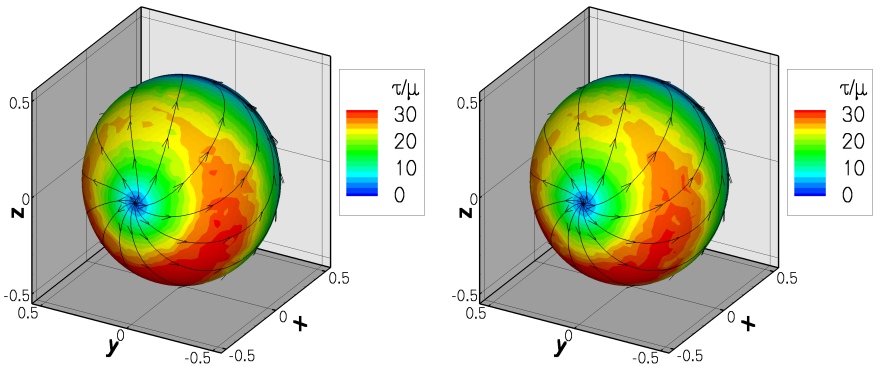

(e) $t = 19$ (f) $t = 20$

Figure 6.33: Spinning sphere at $Re = 300$, oblique rotation: skin friction magnitude and lines, front view

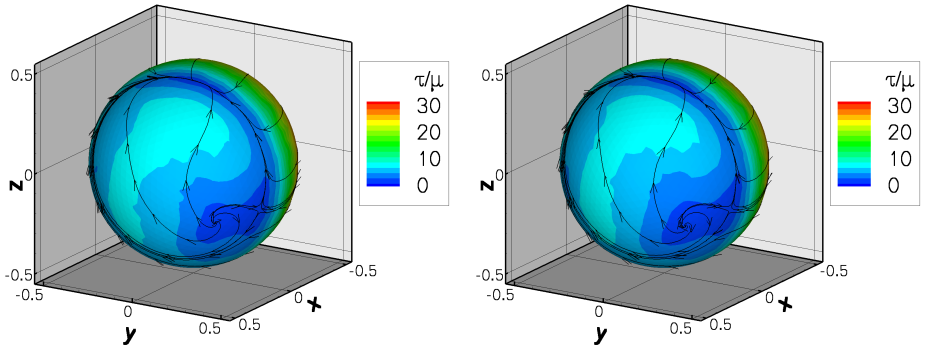

(a) $t = 15$ (b) $t = 16$

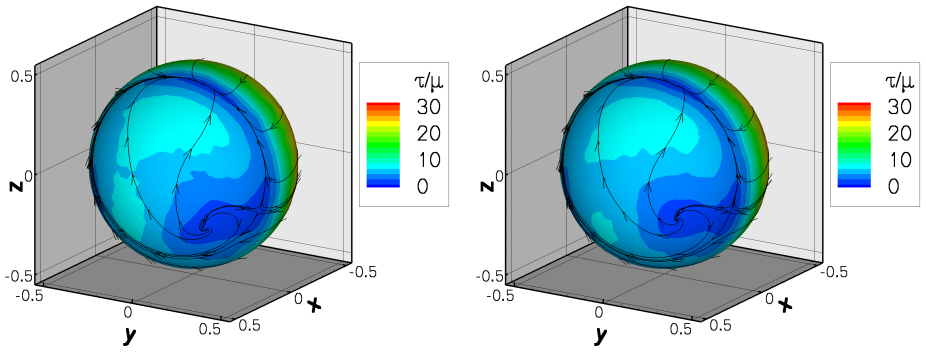

(c) $t = 17$ (d) $t = 18$

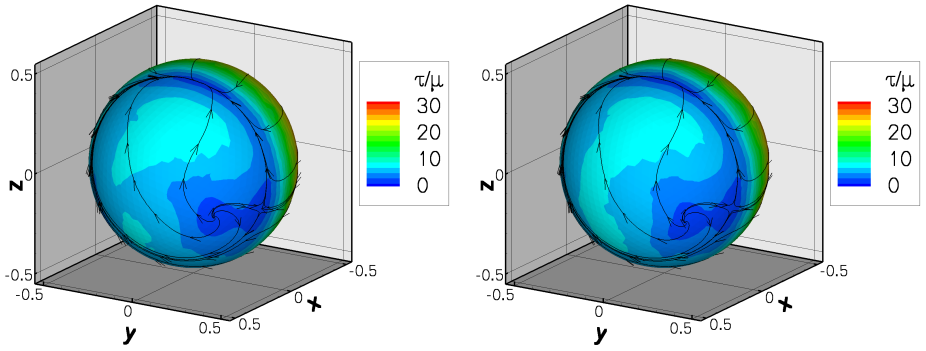

(e) $t = 19$ (f) $t = 20$

Figure 6.34: Spinning sphere at $Re = 300$, oblique rotation: skin friction magnitude and lines, back view

6.6 Conclusions

The first objective of this chapter was the validation of the approaches discussed in Chapter 4 and 5. Our results for the first configuration were found to be in agreement with recent numerical results. Our force measurements for the transverse rotation appear to be sound as they are inside the bounds given by experimental correlations for $Re \simeq 300$.

Wall vorticity measurements still display some spatial noise. The oscillations can be tracked to the solution of the boundary element method. This issue can be mitigated by increasing the size of the panels relative to the particles, as is done in Section 6.5. Beyond those numerical considerations, the present work brings new results for the spinning sphere flow at moderate Reynolds number.

Chapter 7

Flapping Motions

7.1 Introduction

The developments of Chapter 4 allow the study of flows with motions more complicated than the spinning sphere (Chapter 6). This chapter presents preliminary results for flows that involve the flapping motions of rigid objects. We consider the flow around a simplified fish in the presence of a free-stream and the swimming motion of an isolated plate.

7.2 Fish

We model a fish in a free-stream with two ellipsoids, one for the body, the other for the fin. Each ellipsoid is generated from a sphere made of 1280 triangles which is then stretched into an ellipsoid. The body is centered at the origin; its major axes are 2, 0.5 and 1 (Fig. 7.1). The fin is located at $x = 1.6$; its major axes are 1, 0.3 and 1.5. The Reynolds number based on the free-stream is $Re = U_\infty L/\nu = 100$ where L is the length of the fin.

The geometry and the results are made dimensionless by the change of variables

$$\begin{aligned} t &= \frac{U_\infty t^*}{L} \\ \mathbf{x} &= \frac{\mathbf{x}^*}{L} \,. \end{aligned}$$

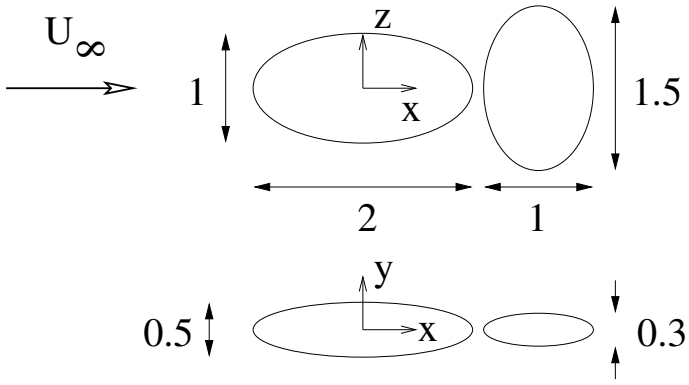

Figure 7.1: Swimming fish: geometry

The center of the fin is in a periodic translation

$$x = 1.6 \tag{7.1}$$

$$y = 0.2588 \sin(2\pi f t + \phi_t) \tag{7.2}$$

$$z = 0\ ; \tag{7.3}$$

its angle with the flow is also periodic

$$\theta_z = 0.2618 \sin(2\pi f t + \phi_r)\ .$$

7.2.1 Low Frequency

The motion frequency is chosen as 0.25. The phase shift angles ϕ_t and ϕ_r are set to 0. The time step δt is 0.02 and the redistribution used a trumpet mapping ($R_0 = 2$, $m = 400$, $\mathbf{x}_0 = [0\,0\,0]$). The numerical diagnostics of this simulation are shown in Fig. 7.2.

From the momentum plot (Fig. 7.3), we see that the wake is not momentum-less, i.e., I_x is not reaching a steady value. The fish is thus not overcoming drag. Fig. 7.4 and 7.5 show the vorticity structures shed by this configuration in terms of the sign

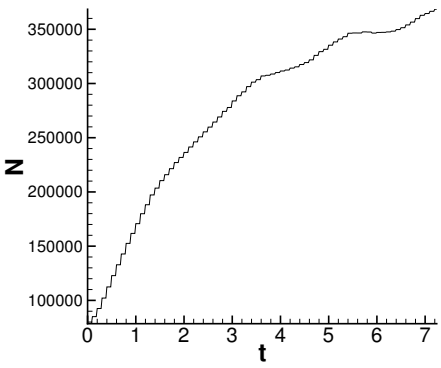

(a) Number of elements

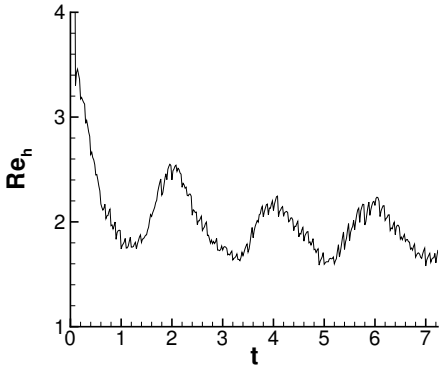

(b) Maximum mesh Reynolds number

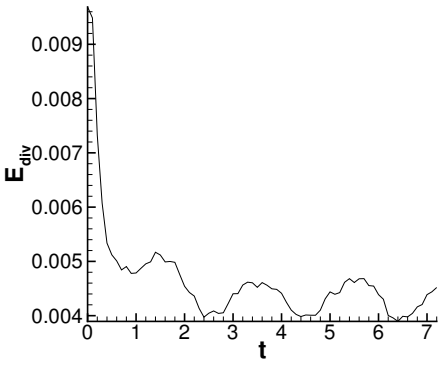

(c) Divergence error

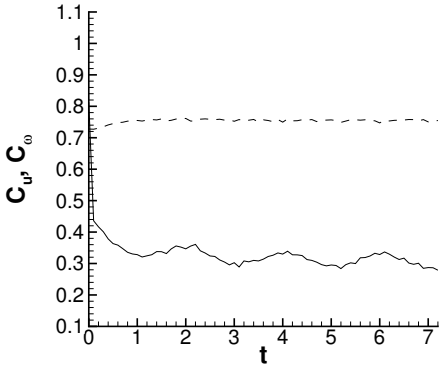

(d) Courant number, vorticity expression (solid) and velocity expression (dashed)

Figure 7.2: Swimming fish at $Re_{U_\infty} = 100$, $f = 0.25$: numerical diagnostics

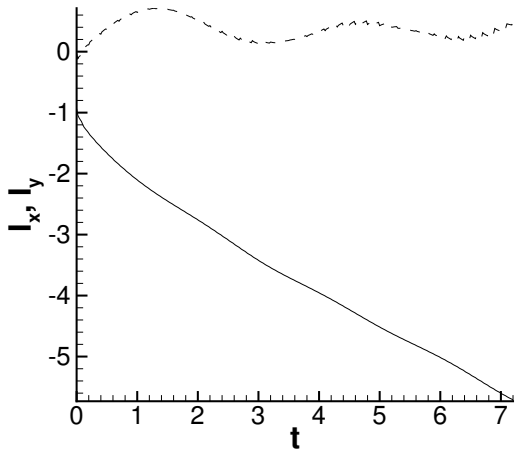

Figure 7.3: Swimming fish at $Re_{U_\infty} = 100$, $f = 0.25$: flow momentum; stream-wise momentum I_x is solid, transverse I_y is dashed.

of ω_z in the symmetry plane and $Q = 0$ surfaces.

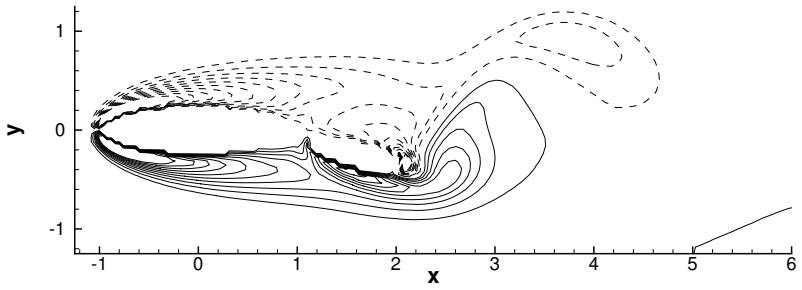

Figure 7.4: Swimming fish at $Re_{U_\infty} = 100$, $f = 0.25$: ω_z in the $z = 0$ plane at $t = 7.6$, contours in the interval $[-5; 5]$ by step of 0.5, the value 0 is omitted. Positive contours are solid; negative ones, dashed.

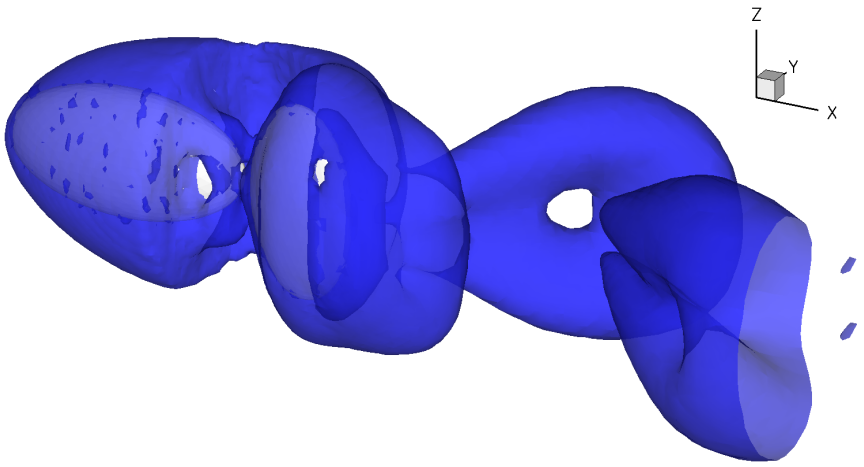

Figure 7.5: Swimming fish at $Re_{U_\infty} = 100$, $f = 0.25$: $Q = 0$ surfaces at $t = 7.6$

7.2.2 High Frequency

With the intent to produce more thrust, we increase the flapping frequency to 1. The time step δt is 0.01 and the redistribution used a trumpet mapping ($R_0 = 2$, $m = 600$, $\mathbf{x}_0 = [1\,0\,0]$). This simulation covers three periods of the flapping motion.

We see from the diagnostics in Fig. 7.6, and in particular, C_ω (Fig. 7.6(d)), that high values of vorticity are reached during this simulation. It is explained by the faster flapping and the shedding of a vortex sheet at the back end of the fin. This localized peak of vorticity evidently affects the vorticity divergence (Fig. 7.6(c)). From the momentum plot (Fig. 7.7), we note that the transverse component exhibits noise related to the vortex sheet shedding mentioned earlier. No positive thrust was achieved. Contours of ω_z and $Q = 0$ iso-surfaces are shown in Fig. 7.8 and 7.9 respectively.

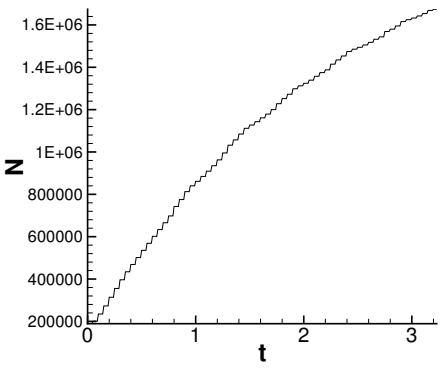

(a) Number of elements

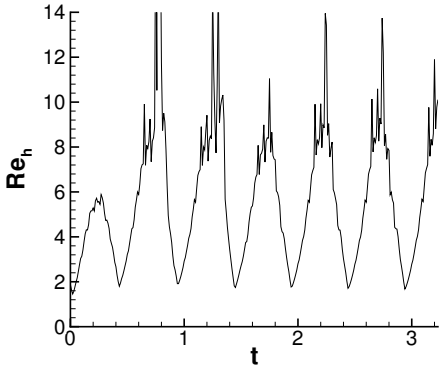

(b) Maximum mesh Reynolds number

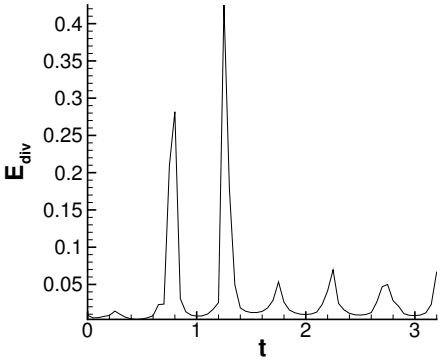

(c) Divergence error

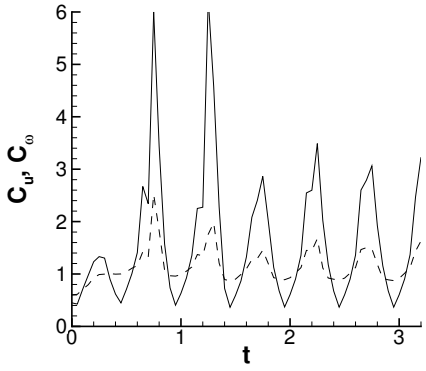

(d) Courant number, vorticity expression (solid) and velocity expression (dashed)

Figure 7.6: Swimming fish at $Re_{U_\infty} = 100$, $f = 1$: numerical diagnostics

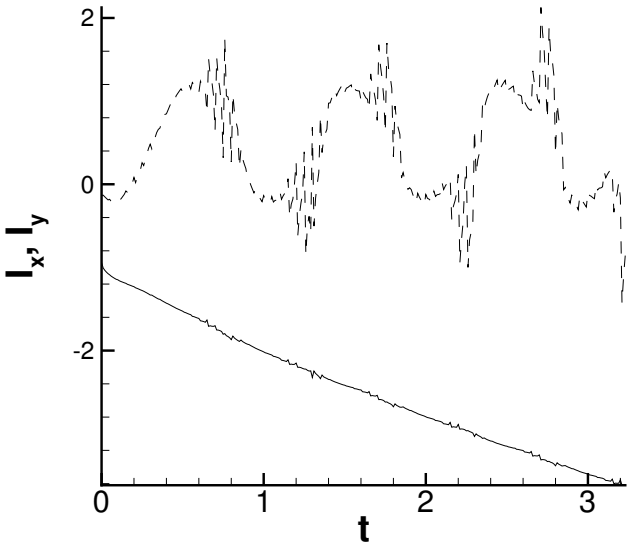

Figure 7.7: Swimming fish at $Re_{U_\infty} = 100$, $f = 1$: flow momentum; stream-wise momentum I_x is solid, transverse I_y is dashed.

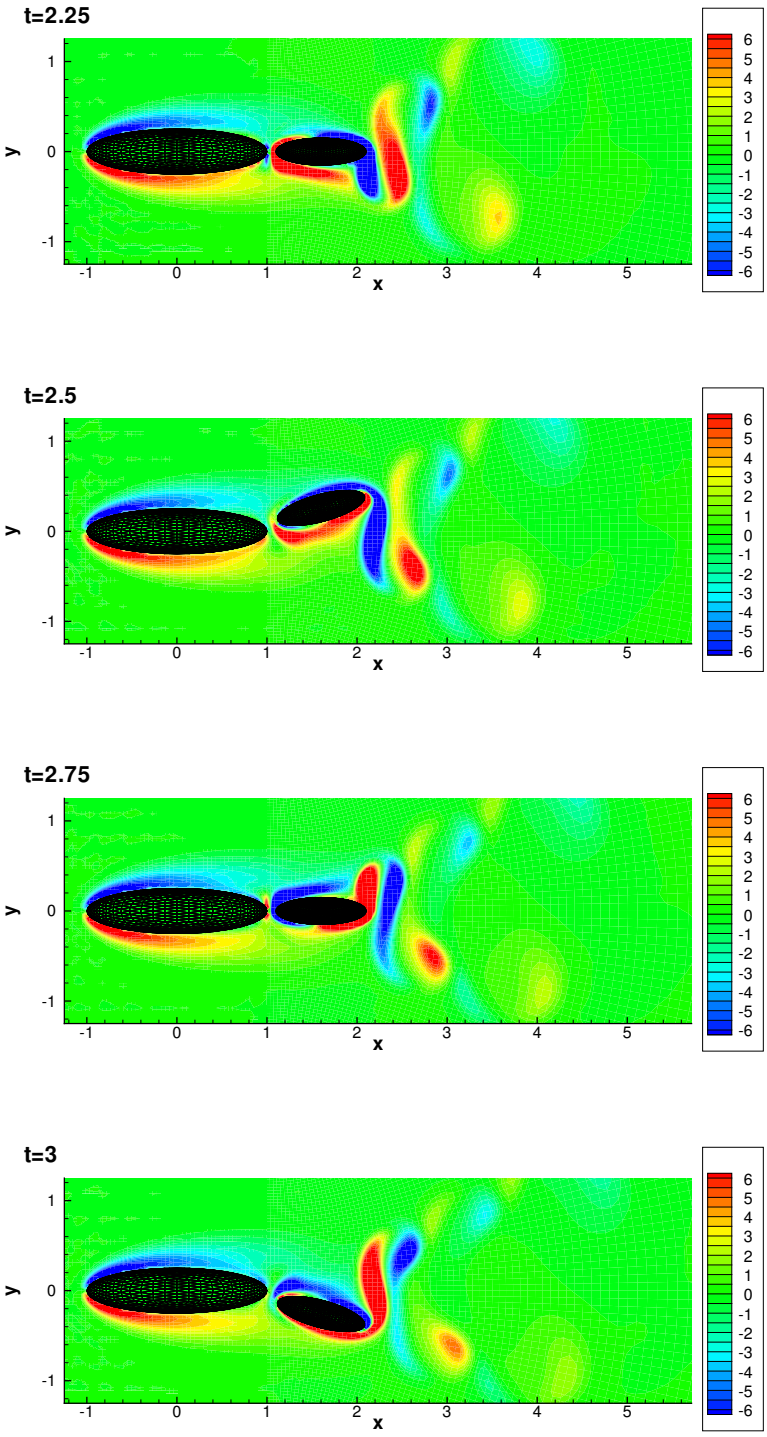

Figure 7.8: Swimming fish at $Re_{U_\infty} = 100$, $f = 1$: ω_z in the $z = 0$ plane at four stages of a stroke

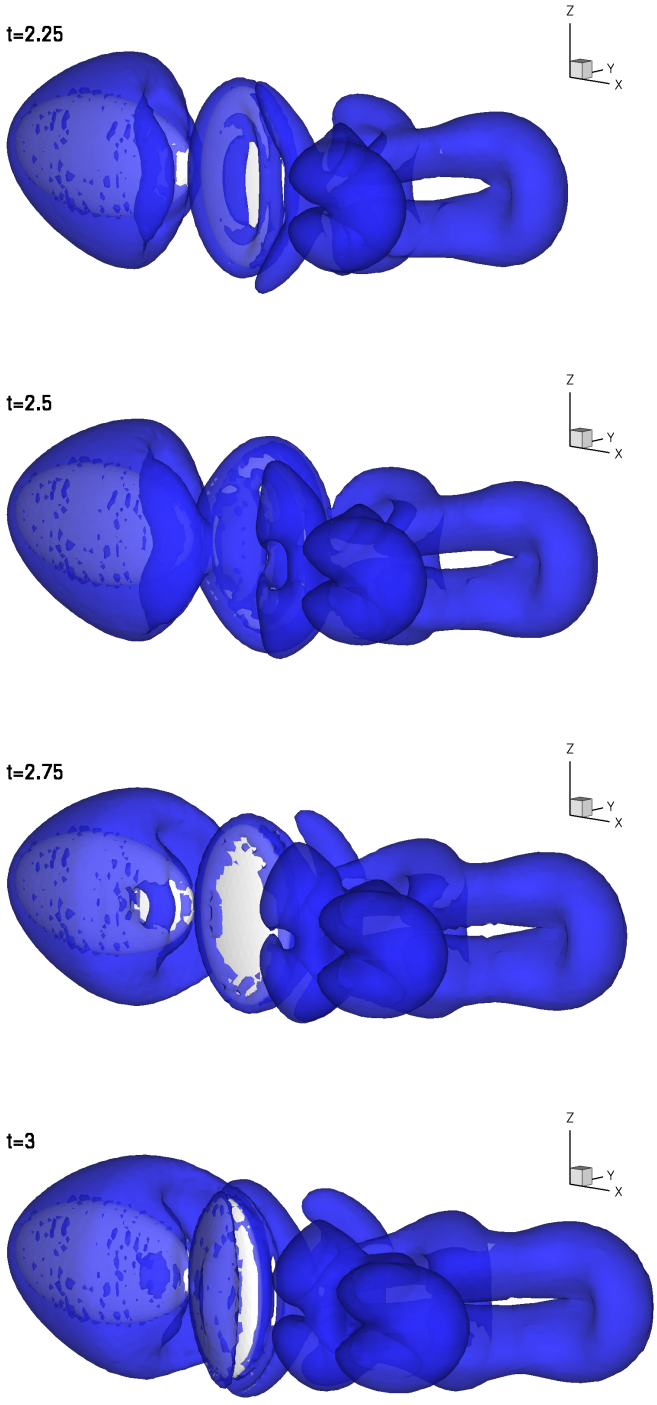

Figure 7.9: Swimming fish at $Re_{U_\infty} = 100$, $f = 1$: $Q = 0$ transparent surfaces at four stages of a stroke

7.3 Flapping Plate

Let us consider a simpler geometry with no free-stream. It is a single flat ellipsoid with major axes [1, 0.25, 2]. As for the fish, the geometry and the periodic motion are defined with respect to the first major axis of the ellipsoid L, $\mathbf{x} = \mathbf{x}'/L$. The motion is described as follows,

$$x = 0 \tag{7.4}$$

$$y = 1 \sin(2\pi f t + \phi_t) \tag{7.5}$$

$$z = 0 \ , \tag{7.6}$$

and

$$\theta_z = \pi/4 \sin(2\pi f t + \phi_r) \ ,$$

where $f = 0.25$, $\phi_t = -\pi/2$ and $\phi_r = -\pi$. The phase difference between the translation and the rotation is such that the plate is perpendicular to the axis of translation at its extreme positions and reaches an angle of attack of 45^o when it is at $y = 0$.
If we call A the amplitude of the translation, a Reynolds number of this flow can be defined as

$$Re = \frac{2\pi f A L}{\nu} = 157 \ .$$

We used a trumpet mapping with $R_0 = 4$, $m = 4$ and $\mathbf{x}_0 = [-0.500]$. The time step was set to 0.02.

This configuration exhibits the same numerical problems as the high frequency fish; the plate sheds a vortex sheet during a part of its stroke. We can see from the momentum history (Fig. 7.11) that we increase the x component. We have been through roughly two cycles and can already observe periodic features. The slope of I_x is the largest when the plate is in the middle of its translation and going through $y = 0$ (at $t = 1$, 3 and 5). As the plate goes through the extrema of the motion (at $t = 2$, 4 and 6), I_x exhibits some noise and a slight dip. We also note that the evolution of I_y displays more important slopes than I_x; this means that our flapping

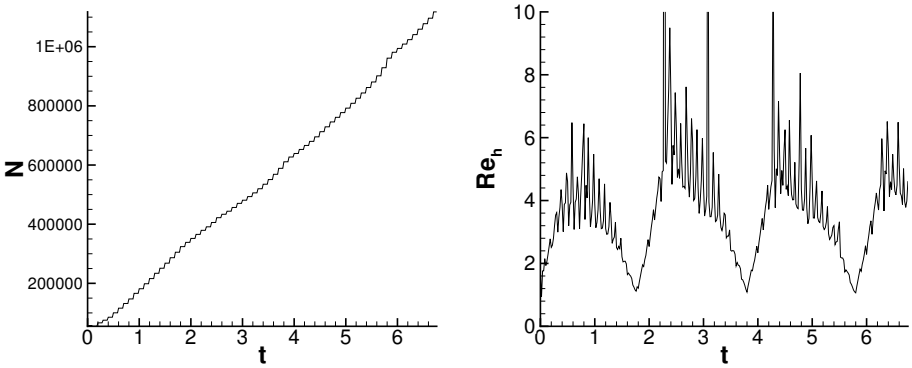

(a) Number of elements

(b) Maximum mesh Reynolds number

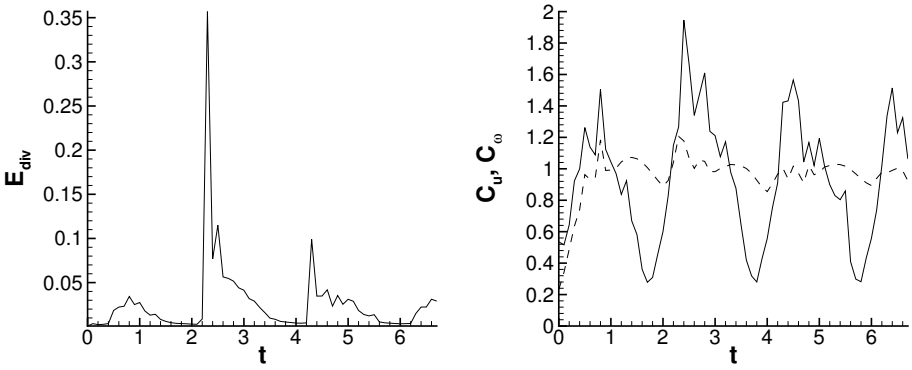

(c) Divergence error

(d) Courant number, vorticity expression (solid) and velocity expression (dashed)

Figure 7.10: Flapping plate at $Re = 157$: numerical diagnostics

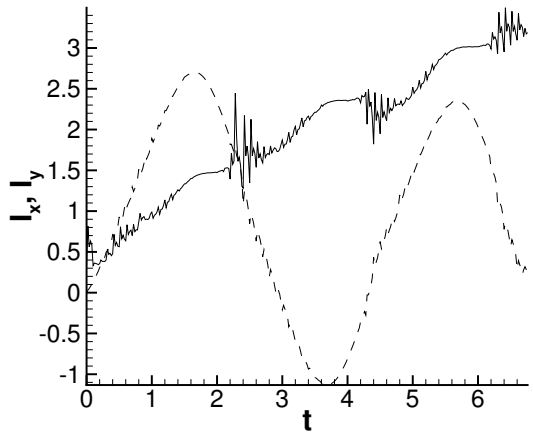

Figure 7.11: Flapping plate at $Re = 157$: flow momentum; the component I_x is solid, the transverse one I_y is dashed.

motion probably induces an important flow in the transverse direction. It may thus require significant power ($\propto F_y \dot{y}_{\text{plate}}$) and not be very efficient in this respect.

Fig. 7.12 shows the vortex structures of this flow after two periods, at $t = 8$. The plate sheds trailing vortices which, logically, have the same induced velocity for strokes in both directions. The structures shed at the extreme positions are relatively large and have moved a fair distance in the y direction, which is in agreement with our earlier interpretation of I_y.

7.4 Conclusions

From a numerical perspective, the results of this chapter show that our method can handle complex moving geometries and that it is therefore well adapted for flapping and swimming motions. However, they point to some shortcomings too; our method does not adapt its resolution in an efficient manner for this family of flows and may fail to resolve very fine scales, e.g., in the case of a separation at an edge. Our results also give us a preview of the complex physics of such flows; we see that the kinematics, in particular, will require a lot of care if we want to develop thrust efficiently.

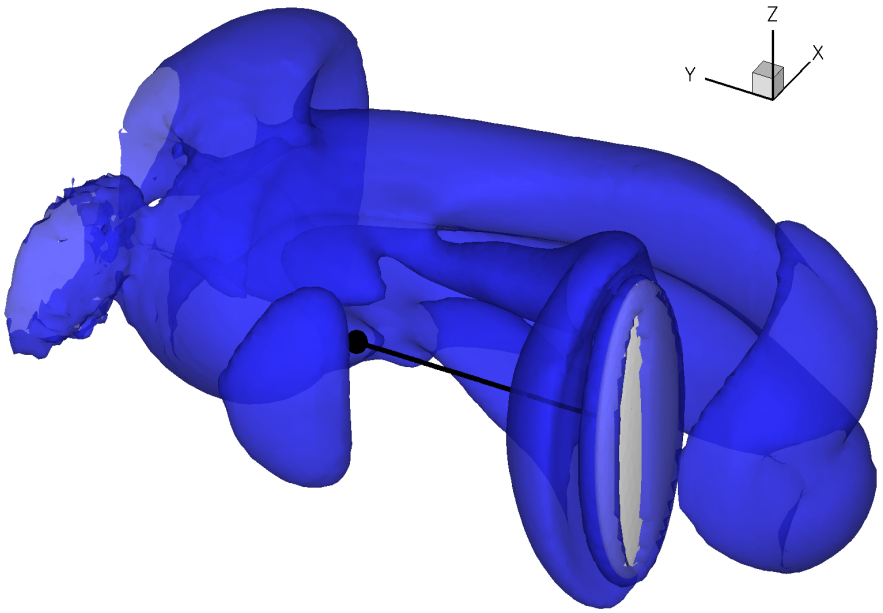

Figure 7.12: Flapping plate at $Re = 157$: transparent $Q = 0$ surfaces at $t = 8$; the black line represents the trajectory of the center of the plate

Chapter 8

Discussion and Outlook

To recapitulate, our work covered a broad range of issues for the three-dimensional vortex element method. Our first area of work was the construction and implementation of redistribution schemes based on the face-centered cubic lattice. These schemes introduce fewer new elements and display better isotropy than their counterparts in a cubic lattice. Our code was then used to investigate the physics of vortex ring reconnections. An algorithm to compute the vorticity autocorrelation and the energy spectrum was implemented, however its complexity in $O(N^2)$ restricts it to small problems.

The second part of our work concerned bounded flows. We derived the contributions for spinning or deforming boundaries in the framework of the Biot-Savart law and introduced a method to compute them from a surface integral. While the kernel for spinning rigid boundaries is quite simple and based on the angular velocity, the expression for general deformations is naturally more complex. We introduced attached elements to represent near-wall vorticity. These elements have a shape function and a velocity kernel that accounts for the surface curvature. A hybrid strength exchange scheme was developed for the viscous interaction between these attached elements and free elements. They are used to enforce the wall normal vorticity boundary condition and mitigate the need for image particles across the wall.

These tools were used to compute the flow past a spinning sphere at $Re = 300$. Three configurations were studied, one per orientation of the angular velocity. The

dimensionless spin rate was kept constant at 0.5. For stream-wise rotation, we obtained good quantitative agreement with previous work for the forces and separation position. There are very few experimental or numerical results in the case of the transverse rotation at our Reynolds number. We could only verify that our force coefficients are bounded by correlations for smaller and larger Re. Results are even scarcer if we consider an oblique rotation.

Preliminary results for more complex flows were presented in Chapter 7. We considered the swimming motion of a simplified fish at $Re_{U_\infty} = 100$ at two different frequencies and the flapping motion of a plate with no free-stream.

Future Work

In its current state, our code is able to handle rigid geometries that are more complicated than the sphere. It includes a version of Rubel (2002)'s closest point transform code to handle the computation of the distances relative to the boundaries. To reduce the memory requirements, our version includes a threshold beyond which the computed distance is approximated.

The simulation of more realistic swimming or insect flight motions at moderate Re will require the development of the boundary terms for deforming boundaries. However, in many cases, the flapping limb is thin enough to be considered a membrane. Because its volume is small, its deformations do not induce a contribution to Biot-Savart. Nevertheless, infinitely thin surfaces will need additional treatment in our code.

One other possible field of application is tumbling motions. This application will need additional work because forces must be computed efficiently at every time step.

Finally, as the results in Chapter 7 suggest, fine scales may appear rapidly for arbitrary flapping motions. A smoothly varying particle size can thus become impractical. In the long term, we will need a more flexible adaptation of the vortex element size if we want to treat complex deforming geometries at high Reynolds numbers. The answer may be in a combined Vortex-in-cell and Biot-Savart method where the latter

generates the boundary conditions of the former.

Appendix A

Face-Centered Cubic and Hexagonal Redistributions

This section present the development and analytical expressions of the schemes presented in Chapter 2.

A.1 Hexagonal Lattice

The sites of the hexagonal lattice are described as $\mathbf{x_n} = \mathbf{Rn}$, where the matrix $\mathbf{R}$'s columns contain the lattice directions

$$\mathbf{R} = \begin{pmatrix} 1 & 1/2 \\ 0 & \sqrt{3}/2 \end{pmatrix}.$$

There is a dual lattice, defined by the matrix

$$\hat{\mathbf{R}} = \left(\mathbf{R}^{-1}\right)^t = \begin{pmatrix} 1 & 0 \\ -\sqrt{3}/3 & 2\sqrt{3}/3 \end{pmatrix}.$$

These two lattices and their coordinate systems are presented in Fig. A.1.

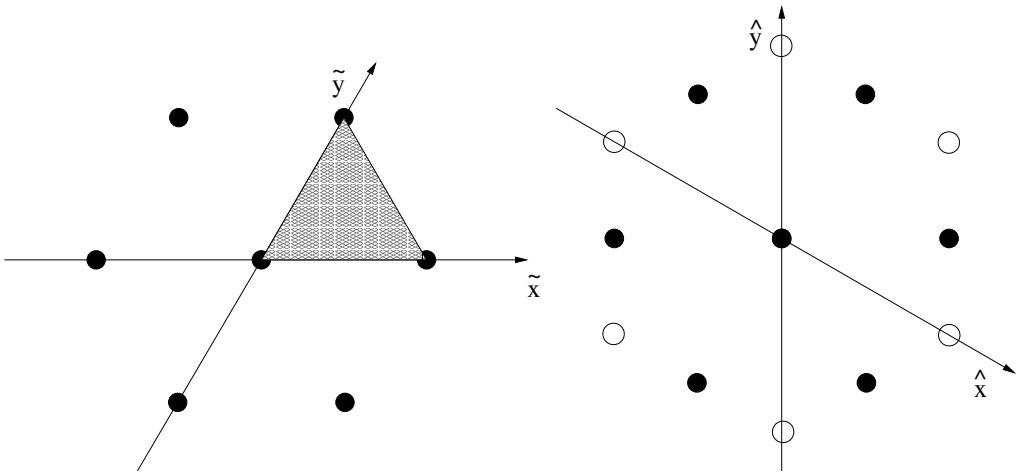

(a) Lattice coordinates (b) Dual lattice coordinates

Figure A.1: The hexagonal lattice, its dual lattice and their coordinate systems

A.1.1 Splines

The family of splines are built from the indicator function of the Voronoi cell

$$\mathfrak{F}_0 = \begin{cases} 1 & \text{if } |\hat{x}| < 0.5 \text{ and } |\hat{y}| < 0.5 \text{ and } |\hat{x} - \hat{y}| < 0.5 \\ 0 & \text{otherwise} \end{cases} \tag{A.1}$$

where $\hat{x}$ and $\hat{y}$ are dual lattice coordinates. We then take successive convolutions of $\mathfrak{F}_0$ with itself; we get for $\mathfrak{F}_1$

$$\mathfrak{F}_1 = \frac{4}{3} \begin{cases} (1-\hat{x}')(1-\hat{x}'-\hat{y}') & \text{if } |\hat{x}'+\hat{y}'| < 1 \text{ and } |\hat{x}'| > 0.5 \\ (1-\hat{y}')(1-\hat{x}'-\hat{y}') & \text{if } |\hat{x}'+\hat{y}'| < 1 \text{ and } |\hat{y}'| > 0.5 \\ ((1-\hat{y}')(1-\hat{x}'-\hat{y}') - (0.5-\hat{y}')^2) & \text{if } |\hat{x}'| \leq 0.5 \text{ and } |\hat{y}'| \leq 0.5 \\ 0 & \text{otherwise} \end{cases} \tag{A.2}$$

For conciseness, we use variables $\hat{x}'$, $\hat{y}'$ that map all the sextant onto the first one

$$\hat{x}' = \begin{cases} |\hat{x} - \hat{y}| & \text{if } \hat{x}\hat{y} > 0 \text{ and } |\hat{x}| > |\hat{y}| \\ |\hat{x}| & \text{otherwise} \end{cases} \tag{A.3}$$

$$\hat{y}' = \begin{cases} |\hat{x} - \hat{y}| & \text{if } \hat{x}\hat{y} > 0 \text{ and } |\hat{x}| <= |\hat{y}| \\ |\hat{y}| & \text{otherwise} \end{cases} \tag{A.4}$$

A.1.2 Compact Schemes

The compact schemes are expressed in the lattice coordinate system. For the C^0 scheme, we have

$$\mathfrak{H}_{C^0} = \begin{cases} 1 - \tilde{x}' - \tilde{y}' & \text{if } |\tilde{x}' + \tilde{y}'| < 1 \\ 0 & \text{otherwise} \end{cases} \tag{A.5}$$

where once again we use a mapping to work in the first sextant–the first quarter in the hexagonal lattice coordinate system–

$$\tilde{x}' = \begin{cases} |\tilde{x}| & \text{if } \tilde{x}\tilde{y} > 0 \\ |\tilde{x} + \tilde{y}| & \text{otherwise} \end{cases} \tag{A.6}$$

$$\tilde{y}' = \begin{cases} |\tilde{y}| & \text{if } \tilde{x}\tilde{y} > 0 \\ \min(|\tilde{x}|, |\tilde{y}|) & \text{otherwise} \end{cases} \tag{A.7}$$

The C^2 scheme is found by convolution of the C^0 scheme by itself

$$\mathfrak{H}_{C^2} = \frac{1}{12}\begin{cases} (\tilde{x}' - \tilde{y}' - 2)(\tilde{x}' + \tilde{y}' - 2)^3 & \text{if } |\tilde{x}' + \tilde{y}'| < 2 \text{ and } \tilde{x}' > 1 \\ (\tilde{y}' - \tilde{x}' - 2)(\tilde{x}' + \tilde{y}' - 2)^3 & \text{if } |\tilde{x}' + \tilde{y}'| < 2 \text{ and } \tilde{y}' > 1 \\ (6 + 12\tilde{x}'\tilde{y}'(\tilde{x}' + \tilde{y}' - 1) & \\ \quad - (\tilde{x}'^2 + \tilde{y}'^2)(12 + 2\tilde{x}'\tilde{y}') & \text{if } |\tilde{x}' + \tilde{y}'| < 2 \text{ and } \tilde{x}' + \tilde{y}' < 1 \\ \quad +8(\tilde{x}'^3 + \tilde{y}'^3) - \tilde{x}'^4 - \tilde{y}'^4) & \\ (10 - 12(\tilde{x}' + \tilde{y}') + 12\tilde{x}'\tilde{y}' & \\ \quad - 2\tilde{x}'\tilde{y}'(\tilde{x}'^2 + \tilde{y}'^2) & \text{if } |\tilde{x}' + \tilde{y}'| < 2 \text{ and } \tilde{x}' + \tilde{y}' \geq 1 \\ \quad +4(\tilde{x}'^3 + \tilde{y}'^3) - \tilde{x}'^4 - \tilde{y}'^4) & \\ 0 & \text{otherwise} \end{cases} \tag{A.8}$$

The third order scheme can then be written as

$$\mathfrak{H}^3_{C^1} = \mathfrak{H}^2_{C^2} + \frac{1}{12}\begin{cases} \dfrac{(2(\tilde{x}'^2 - \tilde{y}'^2) - 4\tilde{x}' - 2\tilde{y}')}{(\tilde{x}' + \tilde{y}' - 2)^2} & \text{if } |\tilde{x}' + \tilde{y}'| < 2 \text{ and } \tilde{x}' > 1 \\ \dfrac{(2(\tilde{y}'^2 - \tilde{x}'^2) - 4\tilde{y}' - 2\tilde{x}')}{(\tilde{x}' + \tilde{y}' - 2)^2} & \text{if } |\tilde{x}' + \tilde{y}'| < 2 \text{ and } \tilde{y}' > 1 \\ -\tilde{x}|\tilde{x}^2(12 - 3\tilde{y} - 2\tilde{x}) + 12\tilde{x}(\tilde{y} - 1) & \\ \quad - \tilde{y}(6 - 6\tilde{y} + \tilde{y}^2)| & \text{if } |\tilde{x}' + \tilde{y}'| < 1 \\ -\tilde{y}|\tilde{y}^2(12 - 3\tilde{x} - 2\tilde{y}) + 12\tilde{y}(\tilde{x} - 1) & \\ \quad - \tilde{x}(6 - 6\tilde{x} + \tilde{x}^2)| & \\ -\tilde{x}| - 6 + 6\tilde{x}^2 - 2\tilde{x}^3 & \\ \quad + 6\tilde{y} - 3\tilde{x}^2\tilde{y} - \tilde{y}^3| & \text{if } |\tilde{x}' + \tilde{y}'| < 2 \text{ and } \tilde{x}' + \tilde{y}' > 1 \\ -\tilde{y}| - 6 + 6\tilde{y}^2 - 2\tilde{y}^3 & \\ \quad + 6\tilde{x} - 3\tilde{y}^2\tilde{x} - \tilde{x}^3| & \\ 0 & \text{otherwise} \end{cases} \tag{A.9}$$

A.2 Face-Centered Cubic Lattice

The directions of the FCC lattice and its dual counterpart are given by

$$\mathbf{R} = \begin{pmatrix} 1 & 1/2 & 1/2 \\ 0 & \sqrt{3}/2 & \sqrt{3}/6 \\ 0 & 0 & \sqrt{6}/3 \end{pmatrix}, \; \hat{\mathbf{R}} = \begin{pmatrix} 1 & 0 & 0 \\ -\sqrt{3}/3 & 2\sqrt{3}/3 & 0 \\ -\sqrt{6}/6 & -\sqrt{6}/6 & \sqrt{6}/2 \end{pmatrix}. \tag{A.10}$$

A.2.1 Splines

The first spline is given by

$$\mathfrak{F}_0 = \begin{cases} 1 & \text{if } |\hat{x}| < 0.5 \text{ and } |\hat{y}| < 0.5 \text{ and } |\hat{z}| < 0.5 \\ & \text{and } |\hat{x} - \hat{y}| < 0.5 \text{ and } |\hat{x} - \hat{z}| < 0.5 \text{ and } |\hat{z} - \hat{y}| < 0.5 \\ 0 & \text{otherwise} \end{cases} \tag{A.11}$$

We then get by convolution

$$\mathfrak{F}_1 = \begin{cases} (1-\hat{x}')(1-\hat{y}')(1-\hat{z}') & \text{if } |\hat{x}'| \geq 0.5 \text{ and } |\hat{y}'| \geq 0.5 \\ & \text{and } |\hat{z}'| \geq 0.5 \\ (1-\hat{x}')(1-\hat{y}')\hat{z}' + (0.5-A)(B-\hat{y}'+0.5)^2 & \\ \quad + (2/3)(C-\hat{z}')^3 & \text{if } |\hat{x}'| \geq 0.5 \text{ and } |\hat{y}'| \geq 0.5 \\ \quad + 2(0.5-A)(0.5-B)(C-\hat{z}') & \text{and } |\hat{z}'| < 0.5 \\ \quad + (0.5-B)(A-\hat{x}'+0.5)^2 & \\ (1-\hat{x}')\hat{y}'\hat{z}' + (1.5-2\hat{x}'+\hat{y}')(0.5-\hat{y}')\hat{z}' & \\ + 2(0.5-\hat{x}'+\hat{z}')(0.5-\hat{y}'+\hat{z}')(0.5-\hat{z}') & \\ + (0.5-\hat{x}'+\hat{y}')(0.5-\hat{z}')^2 + 0.5(0.5-\hat{z}')^2 & \text{if } |\hat{x}'| < 0.5 \\ - 2(0.5-\hat{z}'-(\hat{y}'-\hat{z}')/3)(\hat{y}'-\hat{z}')^2 & \\ & \text{if } |\hat{x}'| \geq 0.5 \text{ and } |\hat{y}'| < 0.5 \\ C\,D\,(1-\hat{x}') & \text{and } |\hat{z}'| < 0.5 \\ & \text{and } (\hat{y}'-\hat{x}') \leq -0.5 \\ (1-\hat{x}')\hat{y}'\hat{z}' & \\ \quad + (1.5-2\hat{x}'+\hat{y}')(0.5-\hat{y}')\hat{z}' & \text{if } |\hat{x}'| \geq 0.5 \text{ and } |\hat{y}'| < 0.5 \\ \quad + 2(0.5-A)(0.5-B)(C-\hat{z}') & \text{and } |\hat{z}'| < 0.5 \\ \quad + (0.5-\hat{x}'+\hat{y}')(C-\hat{z}')^2 + 0.5(C-\hat{z}')^2 & \text{and } (\hat{y}'-\hat{x}') > -0.5 \\ \quad - 2(C-\hat{z}'-B/3)B^2)); & \\ 0 & \text{otherwise} \end{cases} \tag{A.12}$$

where the variables $\hat{x}'$, $\hat{y}'$, $\hat{z}'$ are the dual lattice variables reordered in decreasing order $\hat{x}' \geq \hat{y}' \geq \hat{z}'$ and the variables A, B and C are defined as

$$A = \hat{x}' + C - \hat{z}' - 0.5 \tag{A.13}$$

$$B = \hat{x}' + C - \hat{z}' - 0.5 \tag{A.14}$$

$$C = \min(1 + \hat{z}' - \hat{y}', 1 + \hat{z}' - \hat{x}', 0.5) \tag{A.15}$$

$$D = \min(1 + \hat{y}' - \hat{x}', 0.5) \tag{A.16}$$

A.2.2 Compact Schemes

We switch back to the lattice coordinates $\tilde{x}$, $\tilde{y}$, $\tilde{z}$

$$FCC_1 = \begin{cases} 1 - 0.5(|\tilde{x}' + \tilde{y}'| + |\tilde{y}' + \tilde{x}'| + |\tilde{x}' + \tilde{z}'|) & \text{if } \tilde{x}\tilde{y}\tilde{z}(\tilde{x} + \tilde{y} + \tilde{z}) > 0 \\ \frac{1}{6}(1 + 3(1 - (|\hat{y}'| + |\hat{z}'|)) & \\ \quad + 2|1 - (|\hat{y}'| + |\hat{z}'|)| & \text{if } \tilde{x}\tilde{y}\tilde{z}(\tilde{x} + \tilde{y} + \tilde{z}) < 0 \text{ and } \tilde{y}\tilde{z} > 0 \\ \quad - |\hat{x}' + \hat{z}'| - |\hat{x}' + \hat{y}'|) & \\ \frac{1}{6}(1 + 3(1 - (|\hat{z}'| + |\hat{x}'|)) & \\ \quad + 2|1 - (|\hat{z}'| + |\hat{x}'|)| & \text{if } \tilde{x}\tilde{y}\tilde{z}(\tilde{x} + \tilde{y} + \tilde{z}) < 0 \text{ and } \tilde{x}\tilde{z} > 0 \\ \quad - |\hat{y}' + \hat{x}'| - |\hat{y}' + \hat{z}'|) & \\ \frac{1}{6}(1 + 3(1 - (|\hat{x}'| + |\hat{y}'|)) & \\ \quad + 2|1 - (|\hat{x}'| + |\hat{y}'|)| & \text{if } \tilde{x}\tilde{y}\tilde{z}(\tilde{x} + \tilde{y} + \tilde{z}) < 0 \text{ and } \tilde{x}\tilde{y} > 0 \\ \quad - |\hat{z}' + \hat{y}'| - |\hat{z}' + \hat{x}'|) & \\ 0 & \text{otherwise} \end{cases} \tag{A.17}$$

FCC_3 was obtained numerically by the convolution of FCC_1 by itself. The high order FCC_3' was then computed from the combination of FCC_3 with its gradient. These two operations were carried out in Fourier space.

Appendix B

Energy Spectrum

B.1 Definitions

We define the Fourier transform of a field f as

$$\hat{f}(\mathbf{k}) = \frac{1}{(2\pi)^{3/2}} \int f(\mathbf{x}) e^{-i\mathbf{x}\cdot\mathbf{k}}\, d\mathbf{x}\,; \tag{B.1}$$

the inverse transform is

$$f(\mathbf{x}) = \frac{1}{(2\pi)^{3/2}} \int \hat{f}(\mathbf{k}) e^{i\mathbf{x}\cdot\mathbf{k}}\, d\mathbf{k}\,. \tag{B.2}$$

From these definitions, we have for the gradient operator

$$\mathbf{f} = \nabla g \leftrightarrow \hat{\mathbf{f}} = -i\mathbf{k}\hat{g}\,; \tag{B.3}$$

it follows that

$$\mathbf{f} = \nabla \times \mathbf{g} \leftrightarrow \hat{\mathbf{f}} = -i\mathbf{k} \times \hat{\mathbf{g}}\,,$$

$$f = \nabla \cdot \mathbf{g} \leftrightarrow \hat{f} = -i\mathbf{k} \cdot \hat{\mathbf{g}}\,.$$

$$f = \nabla^2 g \leftrightarrow \hat{f} = -|\mathbf{k}|^2 \hat{g}\,.$$

The energy is defined in the physical and Fourier spaces by Parseval's identity,

$$E = \frac{1}{2}\int \mathbf{u}^2\, d\mathbf{x} = \frac{(2\pi)^3}{2}\int \hat{\mathbf{u}}\cdot\hat{\mathbf{u}}^\star\, d\mathbf{k}\,. \tag{B.4}$$

The energy spectrum is then defined as the integral on the spherical shell $|\mathbf{k}| = k$

$$E(k) = \frac{(2\pi)^3}{2}\int \hat{\mathbf{u}}\cdot\hat{\mathbf{u}}^\star\, k^2 d\Omega_k \tag{B.5}$$

where Ω_k is a solid angle measured from the origin.

B.2 Vorticity Formulation

We derive an equivalent expression based on vorticity. From the relations $\mathbf{u} = \nabla\times\boldsymbol{\psi}$ and $\nabla^2\boldsymbol{\psi} = -\boldsymbol{\omega}$, the transforms of velocity and vorticity are related by

$$\hat{\mathbf{u}} = -i\mathbf{k}\times\hat{\boldsymbol{\psi}} = i\mathbf{k}\times\frac{\hat{\boldsymbol{\omega}}}{|\mathbf{k}|^2}\,. \tag{B.6}$$

One thus has

$$\begin{aligned} E(k) &= \frac{(2\pi)^3}{2}\int\left(i\mathbf{k}\times\frac{\hat{\boldsymbol{\omega}}}{|\mathbf{k}|^2}\right)\cdot\left(-i\mathbf{k}\times\frac{\hat{\boldsymbol{\omega}}^\star}{|\mathbf{k}|^2}\right) k^2 d\Omega_k \\ &= \frac{(2\pi)^3}{2}\int\left[(\mathbf{k}\cdot\mathbf{k})\left(\frac{\hat{\boldsymbol{\omega}}\cdot\hat{\boldsymbol{\omega}}^\star}{|\mathbf{k}|^4}\right) - \left(\frac{\mathbf{k}\cdot\hat{\boldsymbol{\omega}}}{|\mathbf{k}|^2}\right)\left(\frac{\mathbf{k}\cdot\hat{\boldsymbol{\omega}}^\star}{|\mathbf{k}|^2}\right)\right] k^2 d\Omega_k \end{aligned}$$

where the second term is nil because $\boldsymbol{\omega}$ is solenoidal,

$$E(k) = \frac{(2\pi)^3}{2}\int \hat{\boldsymbol{\omega}}\cdot\hat{\boldsymbol{\omega}}^\star\, d\Omega_k\,. \tag{B.7}$$

We wish to rewrite this expression in terms of quantities in physical space. By the definition of the Fourier transform,

$$E(k) = \frac{1}{2}\int\int_{\mathbf{x}}\int_{\mathbf{x}'} \boldsymbol{\omega}(\mathbf{x})e^{-i\mathbf{x}\cdot\mathbf{k}}\,\boldsymbol{\omega}(\mathbf{x}')e^{i\mathbf{x}'\cdot\mathbf{k}}\, d\mathbf{x}\, d\mathbf{x}' d\Omega_k\,.$$

We let $\boldsymbol{\rho} = \mathbf{x}' - \mathbf{x}$ and rewrite the triple integral as

$$E(k) = \frac{1}{2} \int \int_{\mathbf{x}} \int_{\rho} \int \boldsymbol{\omega}(\mathbf{x}) \boldsymbol{\omega}(\mathbf{x} + \boldsymbol{\rho}) e^{i\boldsymbol{\rho}\cdot\mathbf{k}} \, d\mathbf{x} \, \rho^2 \, d\rho \, d\Omega_\rho \, d\Omega_k \, ;$$

the integral over Ω_k can be carried out to finally obtain

$$E(k) = 2\pi \int_0^\infty R_\omega(r) \frac{\sin(kr)}{kr} \, dr \tag{B.8}$$

where $R_\omega(r)$ is the vorticity autocorrelation

$$R_\omega(r) = \int_{|\mathbf{r}|=r} \boldsymbol{\omega}(\mathbf{x}) \cdot \boldsymbol{\omega}(\mathbf{x} + \mathbf{r}) \, d\mathbf{x} \, r^2 d\Omega_r \, . \tag{B.9}$$

B.3 Particle Implementation

If one disposes of R_ω, computing the whole energy spectrum is relatively immediate. We will use our vortex particle discretization to sample R_ω. The sample resolution conditions the maximum wavenumber for which we can compute the energy spectrum, the integrand in Eq. B.8 being oscillatory.

The discrete form is

$$R_\omega(r) = \sum_p \sum_q \boldsymbol{\alpha}_p \cdot \boldsymbol{\alpha}_q \int_{|\mathbf{r}|=r} \int \zeta_{\sigma_p}(\mathbf{x} - \mathbf{x}_p) \zeta_{\sigma_q}(\mathbf{x} + \mathbf{r} - \mathbf{x}_q) \, d\mathbf{x} \, r^2 d\Omega_r \, ;$$

in the case of the Gaussian smoothing, we have to compute the term

$$\begin{aligned} &\int_{|\mathbf{r}|=r} \left(\zeta_{\sigma_p} * \zeta_{\sigma_q}\right)(\mathbf{r} - (\mathbf{x}_q - \mathbf{x}_p)) \; r^2 d\Omega_r \\ &= \int \zeta_{\sqrt{\sigma_p^2 + \sigma_q^2}}(\mathbf{r} - (\mathbf{x}_q - \mathbf{x}_p)) \; r^2 d\Omega_r \, . \end{aligned}$$

Integration is straightforward; the following two definitions ensue

$$\chi(\rho,\lambda) = \frac{1}{\sqrt{2\pi}}\frac{\rho}{\lambda}\left(e^{-(\rho-\lambda)^2} - e^{-(\rho+\lambda)^2}\right) \tag{B.10}$$

$$\chi_\epsilon(r,l) = \frac{1}{\epsilon}\chi\left(r/\epsilon, l/\epsilon\right) \tag{B.11}$$

and allow us to write

$$R_\omega(r) = \sum_p \sum_q \boldsymbol{\alpha}_p \cdot \boldsymbol{\alpha}_q \chi_{\sqrt{\sigma_p^2+\sigma_q^2}}\left(r, |\mathbf{x}_p - \mathbf{x}_q|\right) . \tag{B.12}$$

This is a double summation over the elements. Every pair (p,q) contributes to a few sample points r_i of R_ω. Their number will depend on the maximum frequency of the computed spectrum, e.g., one can set $\Delta r = 2\pi/(8k_{\max})$ so to have 8 sampling points per period of $\sin(k_{\max} r)$.

Appendix C

Sources of Vorticity

C.1 Solid Boundaries

This section presents the details of the implementation of wall diffusion. We have to evaluate the contribution of the viscous flux at a wall onto the nearby free elements and the attached elements. In the vicinity of a flat wall, one may use the Green's function for three-dimensional diffusion and write

$$\Delta\boldsymbol{\omega}_{\Delta t,\,dS} = \int_0^{\Delta t} \sigma dS\, 2\, G_{\text{diff}}\left(\mathbf{x}, \Delta t, \mathbf{x}', \tau\right)\, d\tau \tag{C.1}$$

$$= \int_0^{\Delta t} \frac{\Delta\gamma}{\Delta t}\, 2\, \frac{H\left(\Delta t - \tau\right)\, e^{-\frac{|x-x'|^2}{4\nu(\Delta t-\tau)}}}{\left(4\pi\nu(\Delta t-\tau)\right)^{3/2}}\, d\tau \tag{C.2}$$

where H is the Heavyside function and the factor 2 accounts for the half-space geometry. This expression has to be integrated over the particle volume,

$$\Delta\boldsymbol{\alpha}_{\Delta t,\,dS} = \int_{V_p}\int_0^{\Delta t} \sigma\, 2\, \frac{e^{-\frac{|x-x'|^2}{4\nu(\Delta t-\tau)}}}{\left(4\pi\nu(\Delta t-\tau)\right)^{3/2}}\, d\tau \tag{C.3}$$

where we substituted the flux $\boldsymbol{\sigma}$ by its value $\Delta\gamma/\Delta t$ that is constant over the time step and noted that the Heavyside function is always unity inside the integral.

We elect to perform the volume integral first and over spherical volumes. This is justified by the type of redistribution lattice (Face-Centered Cubic) we are using and

by the fewer evaluations of erf that will be required.

$$\int_{V_p} 2\, G_{\text{diff}}\, dV = \int_0^{2\pi}\int_0^{R_p}\int_0^{\pi} \frac{2\, e^{-\frac{r^2+\rho^2+2r\rho\cos(\theta)}{4\nu(\Delta t-\tau)}}}{\left(4\pi\nu(\Delta t-\tau)\right)^{3/2}}\rho^2 \sin\theta\, d\theta d\rho d\phi \tag{C.4}$$

$$= \frac{2}{r}\int_0^{R_p} \frac{e^{-\frac{(\rho-r)^2}{4\nu(\Delta t-\tau)}} - e^{-\frac{(\rho+r)^2}{4\nu(\Delta t-\tau)}}}{\left(4\pi\nu(\Delta t-\tau)\right)^{1/2}}\rho d\rho \tag{C.5}$$

The reader will note the bound R_p which we define as $4\pi/3\, R_p^3 = V_p$, making it different from the lattice step size h, be it in a FCC or cubic lattice. For convenience, we define $\theta = \Delta t - \tau$,

$$\begin{aligned}\int_{V_p} 2\, G_{\text{diff}}\, dV = \frac{2\, r^{-1}}{\left(4\pi\nu\theta\right)^{1/2}} \Bigg[&\int_{-r/\sqrt{4\nu\theta}}^{(R_p-r)/\sqrt{4\nu\theta}} \sqrt{4\nu\theta}(\sqrt{4\nu\theta}u - r)e^{-u^2}du + \\ &\int_{r/\sqrt{4\nu\theta}}^{(R_p+r)/\sqrt{4\nu\theta}} \sqrt{4\nu\theta}(-\sqrt{4\nu\theta}u + r)e^{-u^2}du\Bigg]\end{aligned} \tag{C.6}$$

The integration yields

$$\begin{aligned}\int_{V_p} 2\, G_{\text{diff}}\, dV =& \frac{\left(4\pi\nu\theta\right)^{1/2}}{\pi\, r}\left(e^{-\frac{(R_p+r)^2}{4\nu\theta}} - e^{-\frac{(R_p-r)^2}{4\nu\theta}}\right) \\ &+ \operatorname{erf}\left(\frac{r+R_p}{\sqrt{4\nu\theta}}\right) - \operatorname{erf}\left(\frac{r-R_p}{\sqrt{4\nu\theta}}\right)\end{aligned} \tag{C.7}$$

This expression can then be integrated in time,

$$\Delta\boldsymbol{\alpha}_{\Delta t,\, dS} = \Delta\gamma\, dS\, \left(F(\rho,\rho^+) - F(\rho,\rho^-)\right) \tag{C.8}$$

where we introduced the dimensionless variables $\rho = r/\sqrt{2\nu\Delta t}$, $\rho^+ = (r+R_p)/\sqrt{2\nu\Delta t}$ and $\rho^- = (r-R_p)/\sqrt{2\nu\Delta t}$ and the function F,

$$\begin{aligned}F(\alpha,\beta) =& \sqrt{\frac{2}{\pi}}e^{-\beta^2/2}\left(\beta - \frac{2}{3}\frac{\beta^2-1}{\alpha}\right) + \operatorname{erf}\left(\beta/\sqrt{2}\right)\left(\beta^2+1-\frac{2}{3}\frac{\beta^3}{\alpha}\right) \\ &+ \beta\left(-|\beta| + \frac{2}{3}\frac{\beta^2}{\alpha}\right)\end{aligned} \tag{C.9}$$

Finally, the surface integration is performed by means of quadrature on the panels.

This approach is somewhat different from Ploumhans and Winckelmans (2000). We indeed wanted to use the spherical nature of our elements here, too. As such, our scheme is not conservative. First, our integration is not exact and depends highly on the regularity of the elements' positions. Second, our integral does not cover the near-wall region where our attached elements are. One can then use this region to make the scheme conservative and give it what is left of γ after transferring contributions to particles.

Appendix D

Rotation Kernel

D.1 Multipole Approximation Error

In this section, we will follow the development from Salmon and Warren (1994) to obtain an error bound on multipole expansions for the rotation kernel. We have for the stream function

$$\boldsymbol{\psi}(\mathbf{x}) = -\sum_i \frac{\mathbf{W}_i}{4\pi} \int_{\partial\Omega_i} \frac{\mathbf{x}-\mathbf{x}'}{|\mathbf{x}-\mathbf{x}'|} \cdot \mathbf{n}\, dS(\mathbf{x}')$$

and for velocity

$$\mathbf{u} = \sum_i \frac{\mathbf{W}_i}{4\pi} \times \int_{\partial\Omega_i} \frac{\mathbf{n}}{|\mathbf{x}-\mathbf{x}'|} - \frac{((\mathbf{x}-\mathbf{x}')\cdot\mathbf{n})\,(\mathbf{x}-\mathbf{x}')}{|\mathbf{x}-\mathbf{x}'|^3}\, dS(\mathbf{x}')\,.$$

Equivalently, we can consider the function ϕ_i individually

$$\phi_i(\mathbf{x}) = \int_{\partial\Omega_i} \mathbf{H}(\mathbf{x}-\mathbf{x}')\cdot\mathbf{n}\, dS(\mathbf{x}')$$

with $\mathbf{H} = \frac{\mathbf{x}-\mathbf{x}'}{|\mathbf{x}-\mathbf{x}'|}$. We then have

$$\boldsymbol{\psi}(\mathbf{x}) = -\sum_i \frac{\mathbf{W}_i}{4\pi}\phi_i(\mathbf{x}) \tag{D.1}$$

and

$$\mathbf{u}(\mathbf{x}) = \sum_i \frac{\mathbf{W}_i}{4\pi} \times \nabla\phi_i(\mathbf{x})\,. \tag{D.2}$$

One can write the multipole approximations for ϕ_i and $\nabla\phi_i$ as

$$\phi_i(\mathbf{x}) = \sum_{n=0}^{p} \Phi_{(n)}(\mathbf{x}) + \Delta\Phi_{(p)}(\mathbf{x})$$

where

$$\Phi_{(n)}(\mathbf{x}) = \frac{(-1)^n}{n!}\partial_{i_1\cdots i_n}\mathbf{H}(\mathbf{x}-\mathbf{x}_0)\cdot\mathbf{M}_{(n)}^{i_1\cdots i_n}$$

The successive multipole moments are defined as

$$\mathbf{M}_{(n)}^{i_1\cdots i_n} = \int_S (\mathbf{x}-\mathbf{x}_0)^{i_1}(\mathbf{x}-\mathbf{x}_0)^{i_2}\cdots(\mathbf{x}-\mathbf{x}_0)^{i_n}\mathbf{n}dS\,.$$

We want to bound the error in the approximation of the gradient of ϕ_i which appears in the velocity expression

$$\nabla\phi_i(\mathbf{x}) = \sum_{n=0}^{p} \left(\nabla\Phi\right)_{(n)}(\mathbf{x}) + \Delta\left(\nabla\Phi\right)_{(p)}(\mathbf{x})$$

where

$$\left(\nabla\Phi\right)_{(n)}(\mathbf{x}) = \frac{(-1)^n}{n!}\partial_{i_1\cdots i_n}\nabla\mathbf{H}(\mathbf{x}-\mathbf{x}_0)\cdot\mathbf{M}_{(n)}^{i_1\cdots i_n}\,.$$

We have

$$\Delta\left(\nabla\Phi\right)_{(p)}(\mathbf{x}) = \int_S \left(\nabla\Phi\right)_{(p)}(\mathbf{x},\mathbf{x}')\cdot\mathbf{n}dS \tag{D.3}$$

where

$$\left(\nabla\Phi\right)_{(p)}(\mathbf{x},\mathbf{x}') = \frac{(-1)^{p+1}}{p!}(\mathbf{x}-\mathbf{x}_0)^{i_1}(\mathbf{x}-\mathbf{x}_0)^{i_2}\cdots(\mathbf{x}-\mathbf{x}_0)^{i_{p+1}} \int_0^1 (1-t)^p\partial_{i_1\cdots i_{p+1}}\nabla\mathbf{H}(\mathbf{x}-\mathbf{x}_0-t(\mathbf{x}'-\mathbf{x}_0))\,. \tag{D.4}$$

We can then bound this expression (see Salmon and Warren, 1994, appendix B) with the expansion centered about the origin,

$$\left|\left(\nabla\Phi\right)_{(p)}\left(\mathbf{x},\mathbf{x}'\right)\right| \leq \frac{1}{r}\frac{\alpha^{p+1}}{1-\alpha}$$

with $r = |x|$ and $\alpha = \frac{|x'|}{r}$. If we use this evaluation in Eq. D.3 and carry out the integration, we find

$$\left|\Delta\left(\nabla\Phi\right)_{(p)}\left(\mathbf{x}\right)\right| \leq \frac{1}{r}\frac{1}{1-\frac{b_{\max}}{r}}\frac{B_{(p+1)}}{r^{p+1}} \tag{D.5}$$

where we bounded $(1-\alpha)^{-1}$ by $(1-\alpha_{\max})^{-1}$ and defined the moment $B_p = \int_S |\mathbf{x}-\mathbf{x}_0|^p \, dS$.

If we use the multipoles up to order $p = 2$, this yields the following bound for the velocity

$$\begin{aligned} |\Delta\mathbf{u}|_{(p)} &\leq \frac{|\mathbf{W}_i|}{4\pi}\frac{1}{r}\frac{1}{1-\frac{b_{\max}}{r}}\frac{B_{(3)}}{r^3} &\text{(D.6)}\\ &\leq \frac{|\mathbf{W}_i|}{4\pi}\frac{B_{(2)}}{b_{\max}^3}\frac{1}{1-\frac{b_{\max}}{r}}\left(\frac{b_{\max}}{r}\right)^4, &\text{(D.7)}\end{aligned}$$

where we used the inequality $B_{(3)} < b_{\max}B_{(2)}$; $B_{(2)}$ is indeed a moment that is cheaper to compute and already used in our error bounds for the normal Biot-Savart interactions.

D.2 Kernel and Derivatives

For the sake of completeness, we list here the first few derivatives of $\mathbf{H}$:

$$\mathbf{H}_i(\mathbf{u}) = \frac{\mathbf{u}_i}{|\mathbf{u}|} \tag{D.8}$$

$$\partial_j\mathbf{H}_i = \frac{\delta_{ij}}{|\mathbf{u}|} - \frac{\mathbf{u}_i\mathbf{u}_j}{|\mathbf{u}|^3} \tag{D.9}$$

$$\partial_j\partial_k\mathbf{H}_i = -\frac{\delta_{ij}\mathbf{u}_k + \delta_{ik}\mathbf{u}_j + \delta_{jk}\mathbf{u}_i}{|\mathbf{u}|^3} + 3\frac{\mathbf{u}_i\mathbf{u}_j\mathbf{u}_k}{|\mathbf{u}|^5} \tag{D.10}$$

$$\begin{aligned}\partial_j\partial_k\partial_l\mathbf{H}_i = &-\frac{\delta_{ij}\delta_{kl}+\delta_{ik}\delta_{jl}+\delta_{jk}\delta_{il}}{|\mathbf{u}|^3}\\ &+3\frac{\delta_{ij}\mathbf{u}_k\mathbf{u}_l+\delta_{ik}\mathbf{u}_j\mathbf{u}_l+\delta_{jk}\mathbf{u}_i\mathbf{u}_l+\delta_{il}\mathbf{u}_j\mathbf{u}_k+\delta_{jl}\mathbf{u}_i\mathbf{u}_k+\delta_{kl}\mathbf{u}_i\mathbf{u}_j}{|\mathbf{u}|^5}\\ &-5\frac{\mathbf{u}_i\mathbf{u}_j\mathbf{u}_k\mathbf{u}_l}{|\mathbf{u}|^7}\,.\end{aligned} \tag{D.11}$$

Appendix E

Near-Wall Vorticity

E.1 Viscous Vortex Sheets

E.1.1 Regularization

We have to carry out the convolution

$$\boldsymbol{\omega}(\mathbf{x}) = \int_{\text{sheet}} \zeta_{\sigma(\mathbf{x}')}(\mathbf{x}-\mathbf{x}')\boldsymbol{\gamma}(\mathbf{x}')\, dS(\mathbf{x}')\,.$$

The sheet is discretized with flat panels with a constant strength $\boldsymbol{\gamma}$. The Gaussian can be rewritten as a divergence in cylindrical coordinates attached to the panel and centered at the evaluation point. We have, in coordinates made dimensionless with respect to σ,

$$\zeta(\rho, w) = e^{-\frac{w^2+\rho^2}{2}} = e^{-\frac{w^2}{2}} \frac{1}{\rho}\frac{\partial}{\partial \rho}\left(1 - e^{-\frac{\rho^2}{2}}\right)\,.$$

We can then use the 2D divergence theorem along the perimeter of the panel m

$$\begin{aligned}
\boldsymbol{\omega}(\mathbf{x})|_m &= \int_{S_m} \frac{1}{\sigma^3}\zeta\left(\frac{\mathbf{x}-\mathbf{x}'}{\sigma}\right)\boldsymbol{\gamma}_m\, dS(\mathbf{x}') \\
&= \int_{S_m^u} \frac{1}{\sigma}\zeta\left(\mathbf{u}-\mathbf{u}'\right)\boldsymbol{\gamma}_m\, dS^u = \frac{\boldsymbol{\gamma}_m}{(2\pi)^{3/2}\sigma} e^{-\frac{z^2}{2\sigma^2}} \int_{S_m^u} e^{-\frac{\rho^2}{2}}\, dS^u \\
&= \frac{\boldsymbol{\gamma}_m}{(2\pi)^{3/2}\sigma} e^{-\frac{z^2}{2\sigma^2}} \int_{\Gamma_m^u} \frac{1-e^{-\frac{\rho^2}{2}}}{\rho}\hat{\boldsymbol{\rho}}\cdot\left(d\mathbf{l}^u \times \mathbf{n}\right),
\end{aligned}$$

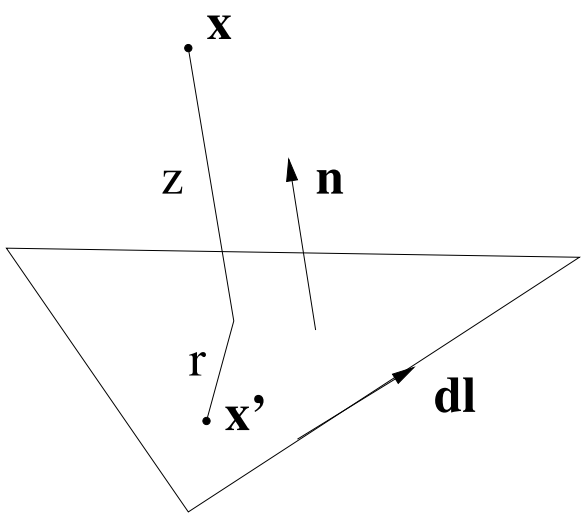

Figure E.1: Sheet regularization: coordinate system

where we have introduced several notations: $\mathbf{u} = \mathbf{x}/\sigma$ are dimensionless coordinates, ρ is the dimensionless radius in the plane of the panel, $\hat{\boldsymbol{\rho}}$ is the radial vector, dS^u and $d\mathbf{l}^u$ are respectively a surface and contour element in the dimensionless coordinate system. The integral we are left with can be decomposed in contributions from each segment of the polygon which can be written as

$$\int_{u_1}^{u_2} \frac{1 - e^{-\frac{u^2+v^2}{2}}}{u^2 + v^2} \, v \, du$$

where we defined u as the coordinate parallel to the segment and v, the perpendicular one. This last expression shows that we have to tabulate the primitive $I_\zeta(u, v) = \int_0^u \cdots du$ for values of u and v within the the kernel cutoff (typically 5). For values of u or v beyond the cutoff, we have an analytical form

$$\left[\arctan\left(\frac{u}{v}\right)\right]_{u_1}^{u_2}.$$

E.1.2 Kernel

We here give the development of the contribution to the stream-function ψ. Contributions to the velocity and velocity gradients are similar or in direct continuation of

the present calculation. We need to compute

$$\boldsymbol{\psi}(\mathbf{x}) = \int_{\text{sheet}} G_{\sigma(\mathbf{x}')}(\mathbf{x}-\mathbf{x}')\boldsymbol{\gamma}(\mathbf{x}')\, dS(\mathbf{x}')\,.$$

As for the regularization, we consider the contribution of a single panel and switch to dimensionless coordinates. We first have

$$G(\rho, w) = \frac{1}{4\pi}\frac{\operatorname{erf}(\sqrt{\frac{w^2+\rho^2}{2}})}{\sqrt{w^2+\rho^2}}\,. \tag{E.1}$$

The contribution of a panel can then be written as

$$\begin{aligned}
\boldsymbol{\psi}(\mathbf{x})|_m &= \int_{S_m} \frac{1}{\sigma} G\left(\frac{\mathbf{x}-\mathbf{x}'}{\sigma}\right)\boldsymbol{\gamma}_m\, dS(\mathbf{x}') \\
&= \sigma\boldsymbol{\gamma}_m \int_{S_m^u} G\left(\mathbf{u}-\mathbf{u}'\right)\, dS^u = \frac{\sigma\boldsymbol{\gamma}_m}{4\pi}\int_{S_m^u}\frac{\operatorname{erf}(\sqrt{\frac{w^2+\rho^2}{2}})}{\sqrt{w^2+\rho^2}}\, dS^u
\end{aligned}$$

We then re-write G as a divergence in the plane of the panel.

$$\begin{aligned}
G(\rho, w) = \frac{1}{4\pi}\frac{1}{\rho}\frac{\partial}{\partial\rho}\Bigg(&\sqrt{\rho^2+w^2}\operatorname{erf}\left(\sqrt{\frac{\rho^2+w^2}{2}}\right) - \sqrt{w^2}\operatorname{erf}\left(\sqrt{\frac{w^2}{2}}\right) \\
&-\sqrt{\frac{2}{\pi}}e^{-\frac{w^2}{2}}\left(1-e^{-\frac{\rho^2}{2}}\right)\Bigg)\,;
\end{aligned} \tag{E.2}$$

we then use the divergence theorem and integrate along the sides of the panel. The integral does not have an analytical form and has to be tabulated in three dimensions.

E.2 Near-Wall Elements

E.2.1 Regularization

We need to re-normalize the unbounded smoothing function by some function $M(\mathbf{x})$ that will depend on the geometry. We have

$$M(\mathbf{x}) = \int_{\mathbb{R}\setminus\Omega_i} \zeta_\sigma(\mathbf{x}-\mathbf{x}')d\mathbf{x}' \tag{E.3}$$

where $\mathbf{x} \in \partial\Omega_i$. If we assume that the boundary is locally spherical–within ζ_σ support–, with a roughly constant curvature radius R, the above integral can be written more explicitly as a function of the local curvature R. In the concave case, we have $R < 0$

$$\begin{aligned} M(R) &= \int_0^{2\pi}\int_0^{\pi/2}\int_0^{2|R|/\sigma\cos(\theta)} \zeta(\rho)\rho^2\sin\theta\, d\rho\, d\theta\, d\phi & \text{(E.4)}\\ &= 2\pi\int_0^{\pi/2} q(2|R|/\sigma\cos(\theta))\sin(\theta)d\theta & \text{(E.5)}\\ &= \frac{\pi\sigma}{|R|}\int_0^{2|R|/\sigma} q(u)\, du & \text{(E.6)} \end{aligned}$$

where $q(\rho) = \int_0^\rho \zeta(t)t^2dt$. For the Gaussian, we have

$$q(\rho) = \frac{1}{4\pi}\left(\mathrm{erf}(\rho/\sqrt{2}) - \sqrt{2/\pi}\rho e^{-\rho^2/2}\right),$$

to finally obtain

$$M(R) = \frac{1}{2}\,\mathrm{erf}(\sqrt{2}|R|/\sigma) - \frac{1}{2}\sqrt{2/\pi}\frac{1-e^{-2|R|^2/\sigma^2}}{|R|/\sigma}. \tag{E.7}$$

In the convex case, $R > 0$, we just have the complementary relation

$$M(R) = 1 - \frac{1}{2}\,\mathrm{erf}(\sqrt{2}R/\sigma) + \frac{1}{2}\sqrt{2/\pi}\frac{1-e^{-2R^2/\sigma^2}}{R/\sigma}. \tag{E.8}$$

We will assume that curvature is constant across a panel. In three dimensions,

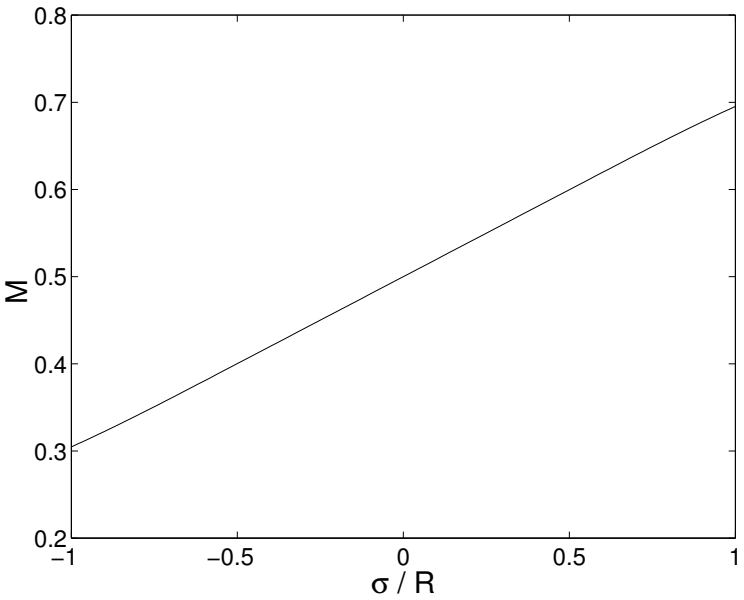

Figure E.2: One-sided panels: Regularization modifier function

it will be taken as the mean curvature which is the average of the two principal curvatures of the surface. This is a good approximation. In the case of a saddle, where the curvatures have opposite signs, the volumes lost and gained in the two main directions should be evened out with this average.

Appendix F

Additional Results for the Flows Past Spinning Spheres

F.1 Stream-Wise Rotation

F.1.1 Helicity

Helicity is a quantity defined by

$$\mathcal{H} = \int \mathbf{u} \cdot \boldsymbol{\omega} \, d\mathbf{x} \, .$$

It measures the entanglement of vortex lines.

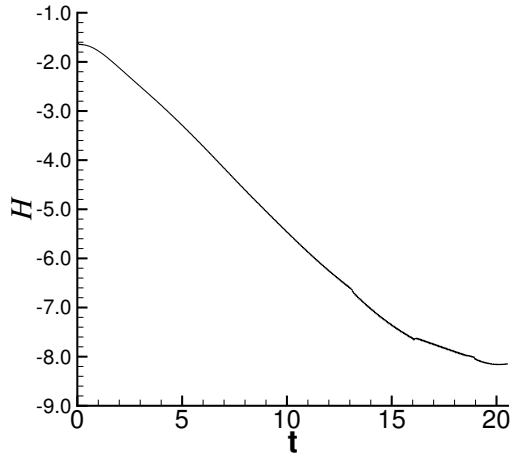

Figure F.1: Spinning sphere at $Re = 300$, stream-wise rotation: helicity

F.2 Transverse Rotation

F.2.1 Helicity

This configuration remains symmetric with respect to the $y = 0$ plane

$$
\begin{aligned}
u_x(\cdot, y, \cdot) &= u_x(\cdot, -y, \cdot) & \omega_x(\cdot, y, \cdot) &= -\omega_x(\cdot, -y, \cdot) \\
u_y(\cdot, y, \cdot) &= -u_y(\cdot, -y, \cdot) & \omega_y(\cdot, y, \cdot) &= \omega_y(\cdot, -y, \cdot) \\
u_z(\cdot, y, \cdot) &= u_z(\cdot, -y, \cdot) & \omega_z(\cdot, y, \cdot) &= -\omega_z(\cdot, -y, \cdot)
\end{aligned}
$$

if one neglects slight numerical deviations. As a consequence, $\mathcal{H} \simeq 0$.

F.2.2 Stream-Wise Vorticity

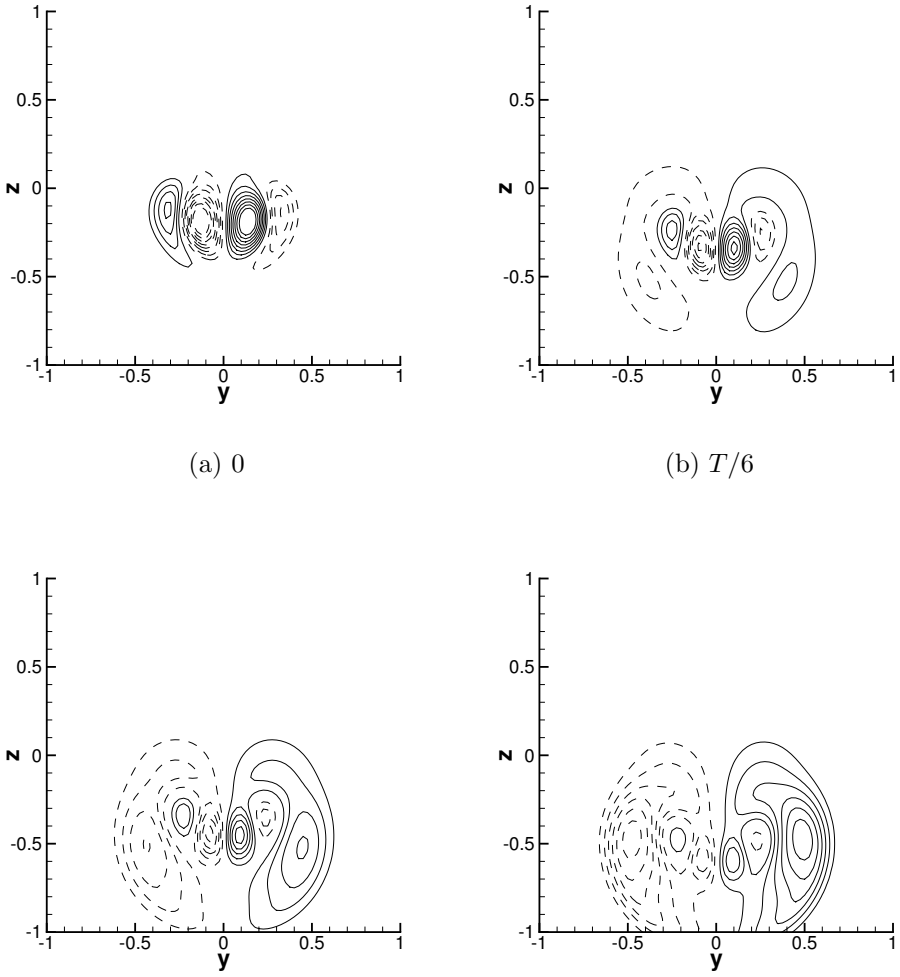

(a) 0

(b) $T/6$

(c) $T/4$

(d) $T/3$

Figure F.2: Spinning sphere at $Re = 300$, transverse rotation: shedding cycle, stream-wise vorticity in the $x = 2$ plane; contours values are in the interval $[-4; 4]$ by steps of 0.5, 0 is omitted

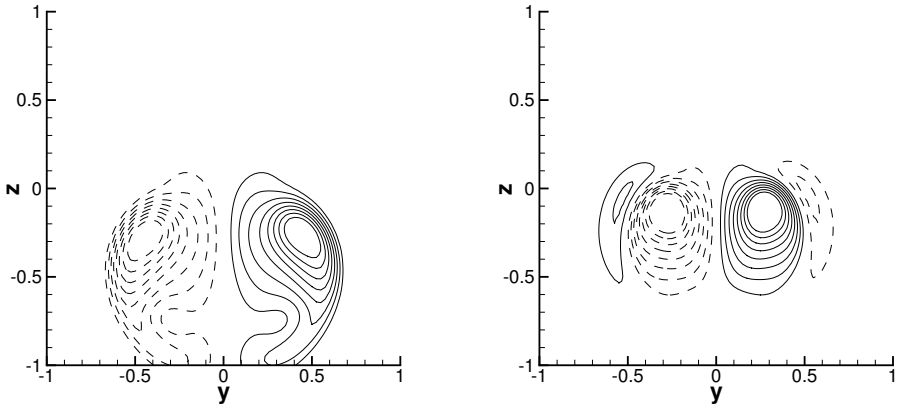

(a) $T/2$

(b) $2T/3$

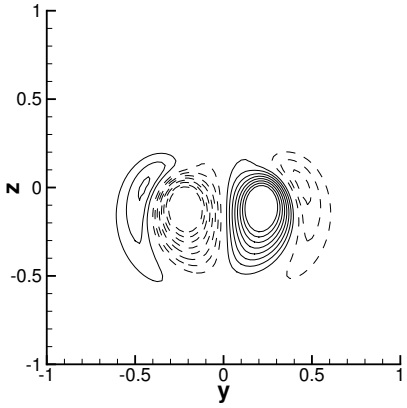

(c) $3T/4$

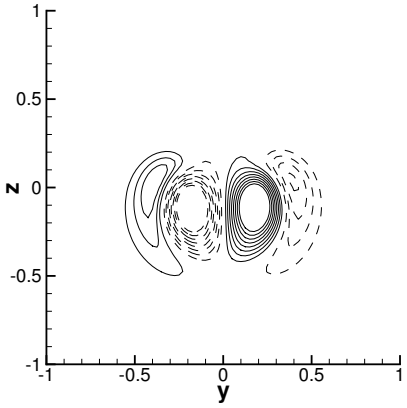

(d) $5T/6$

Figure F.3: Spinning sphere at $Re = 300$, transverse rotation: shedding cycle, streamwise vorticity contours in the $x = 2$ plane (continued)

F.2.3 Bottom Separation

We consider constant ϕ planes and the projection of the velocity field in those planes. For each ϕ, we estimate the position of the saddle.

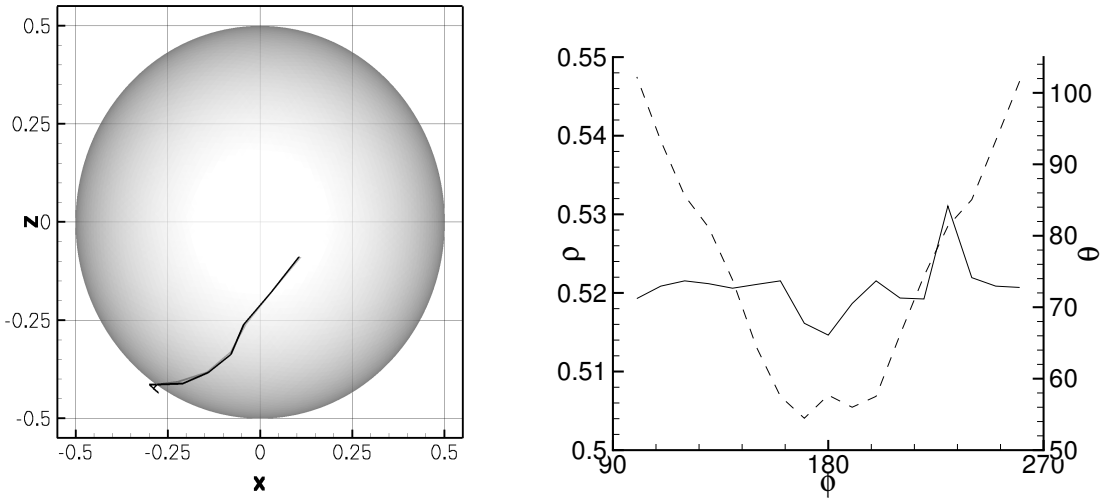

(a) Location with respect to the sphere

(b) Cylindrical coordinates as a function of ϕ: radius $\rho = r/D$ (solid), angle θ (dashed)

Figure F.4: Spinning sphere at $Re = 300$, transverse rotation: separation line

F.3 Oblique Rotation

F.3.1 Helicity

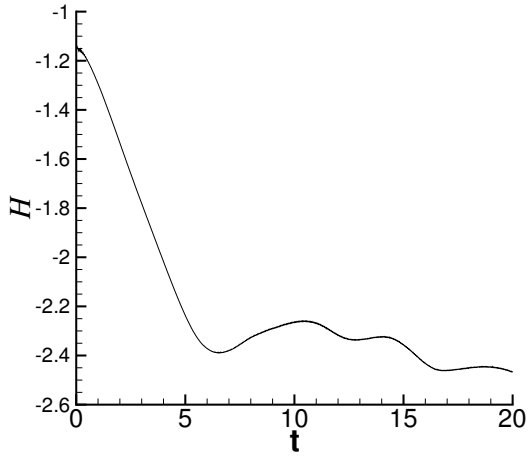

Figure F.5: Spinning sphere at $Re = 300$, oblique rotation: helicity

F.3.2 Stream-Wise Vorticity

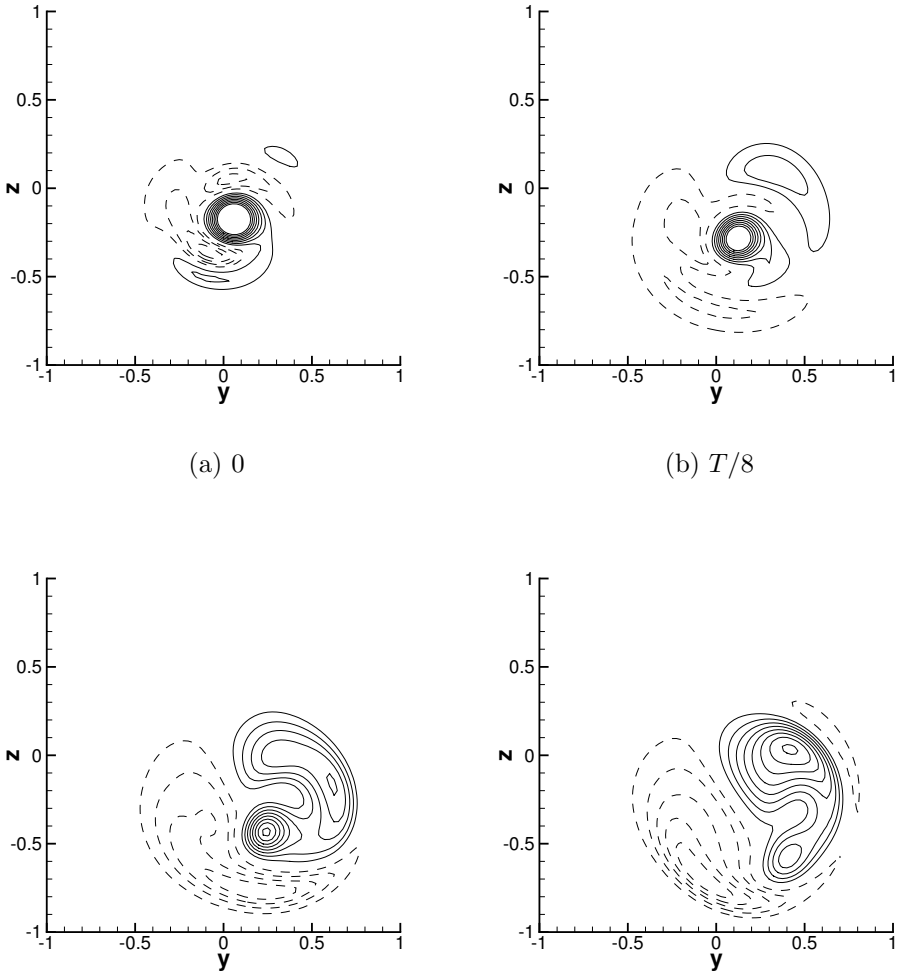

(a) 0

(b) $T/8$

(c) $T/4$

(d) $3T/8$

Figure F.6: Spinning sphere at $Re = 300$, transverse rotation: shedding cycle, stream-wise vorticity in the $x = 2$ plane; contours values are in the interval $[-4; 4]$ by steps of 0.5, 0 is omitted

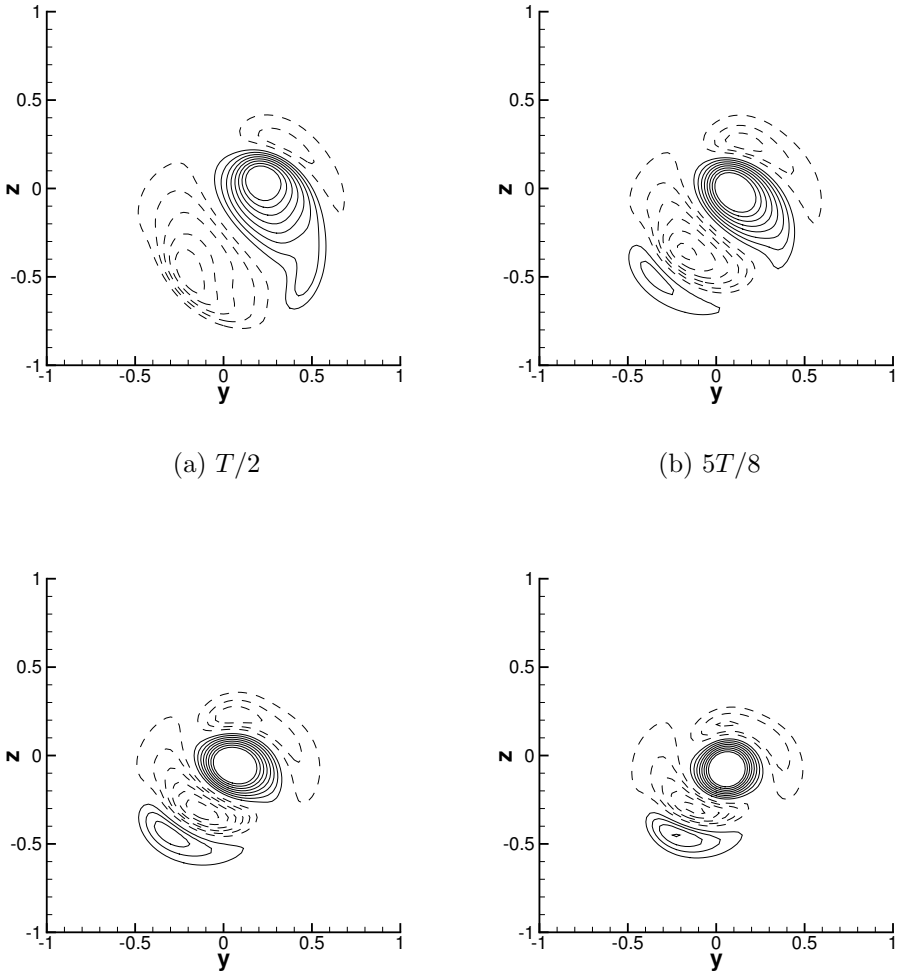

(a) $T/2$

(b) $5T/8$

(c) $3T/4$

(d) $7T/8$

Figure F.7: Spinning sphere at $Re = 300$, oblique rotation: shedding cycle, streamwise vorticity in the $x = 2$ plane (continued)

F.3.3 Bottom Separation

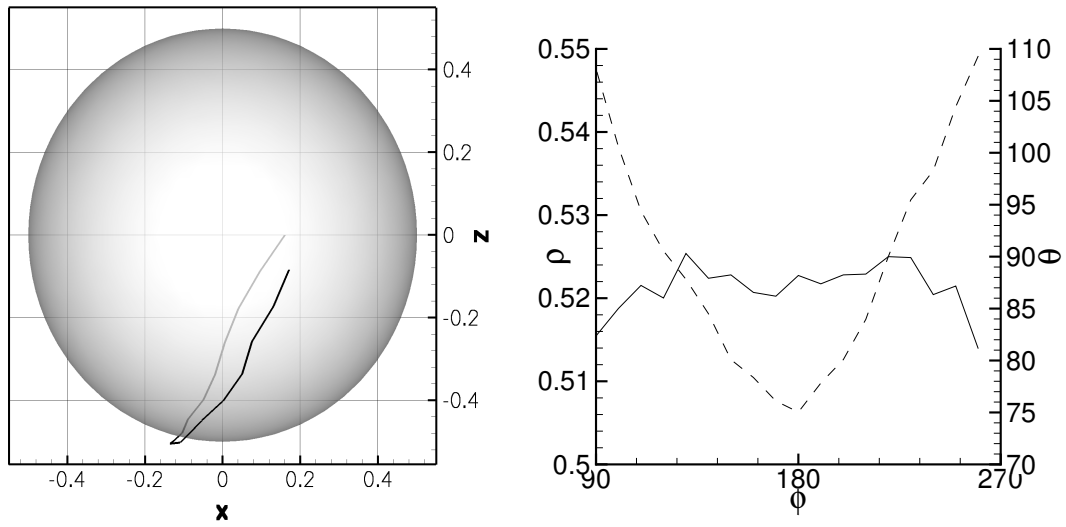

(a) Location with respect to the sphere

(b) Cylindrical coordinates as a function of ϕ: radius $\rho = r/D$ (solid), angle θ (dashed)

Figure F.8: Spinning sphere at $Re = 300$, oblique rotation: separation line

Bibliography

C. Anderson and C. Greengard. On vortex methods. *SIAM J. Num. Anal.*, 22: 413–440, 1985. 9

H. Aref and I. Zawadzki. Linking of vortex rings. *Nature*, 354(6348):50–53, 1991. 31

W. T. Ashurst and D. I. Meiron. Numerical study of vortex reconnection. *Phys. Rev. Lett.*, 58(16):1632–1635, 1987. 31

J. Balakrishnan. Spatial curvature effects on molecular transport by diffusion. *Phys. Rev. E*, 61(4):4648–4651, 2000. 62

H.M. Barkla and L.J. Auchterlonie. The magnus or robins effect on rotating spheres. *J. Fluid Mech.*, 47(3):437–447, 1971. 70, 93

J. Barnes and P. Hut. A hierarchical O(N log N) force calculation algorithm. *Nature*, 324, 1986. 9

G. K. Batchelor. *An Introduction to Fluid Dynamics*. Cambridge Univ. Press, London, 1967. 53

J. T. Beale and A. Majda. Vortex methods ii: high order accuracy in two and three dimensions. *Math. Comput.*, 32:29–52, 1982. 9

P. W. Bearman and J. K. Harvey. Golf ball aerodynamics. *Aeronaut. Q.*, 27:112–122, 1976. 93

M. Brady. *Regularized vortex sheet evolution in three dimensions*. Ph.D. thesis, California Institute of Technology, 2000. 65

R. Brard. A vortex theory for bodies moving in water. In R. Brard and A. Castera, editors, *Proc. 9th Symposium on Naval Hydrodynamics*, pages 1187–1284, 1973. 41, 44

P. Chatelain, D. Kivotides, and A. Leonard. Reconnection of colliding vortex rings. *Phys. Rev. Lett.*, 90(5):054501, 2003. 30

A.J. Chorin. Numerical study of slightly viscous flows. *J. Fluid. Mech.*, 57:785–796, 1973. 6

M. Christensson and M. Hindmarsh. Magnetic fields in the early universe in the string approach to MHD. *Phys. Rev. D*, 60(063001), 1999. 30

G.-H. Cottet and P. Koumoutsakos. *Vortex Methods, Theory and Practice*. Cambridge University Press, 2000. 4, 6, 7, 9, 13, 14, 15, 16, 41, 45, 59, 60

G. Daeninck, P. Chatelain, M. Rubel, G. S. Winckelmans, and A. Leonard. Simulation of vehicle aerodynamics using a vortex element method. In Springer, editor, *The aerodynamics of heavy vehicles: trucks, buses and trains, Lecture notes in applied and computational mechanics*, 2004. 72

P. Degond and S. Mas-Gallic. The weighted particle method for convection-diffusion equations. part 1: The case of an isotropic viscosity. *Math. Comput.*, 53(188): 485–507, October 1989. 6, 7, 59

Y. Dubief and F. Delcayre. On coherent-vortex identification in turbulence. *J. Turbulence*, 1, 2000. 75

J. D. Eldredge, T. Colonius, and A. Leonard. A vortex particle method for two dimensional compressible flow. *J. Comp. Phys.*, 179:371–399, 2002a. 62

J. D. Eldredge, A. Leonard, and T. Colonius. A general deterministic treatment of derivatives in particle methods. *J. Comp. Phys.*, 180:686–709, 2002b. 62

J. Faraudo. Diffusion equation on curved surfaces. i. theory and application to biological membranes. *J. Chem. Phys.*, 116(13):5831–5841, 2002. 62

C. F. Gauss. Besprechung des buchs von l. a. seeber: Intersuchungen ber die eigenschaften der positiven ternren quadratischen formen usw. *Göttingsche Gelehrte Anzeigen (1831, July 9)*, 2:188–196, 1876. 17

A. Gharakhani. Grid-free simulation of 3d vorticity diffusion by a high-order vorticity redistribution method. In *15th AIAA Comp. Fluid Dyn. Conf. (Anaheim, CA, 2001)*. AIAA, 2001. 12

T. C. Hales. The sphere packing problem. *J. Comput. Appl. Math.*, 44:41–76, 1992. 17

T. C. Hales. Sphere packings i. *Discrete & Computational Geometry*, 17:1–51, 1997a. 17

T. C. Hales. Sphere packings ii. *Discrete & Computational Geometry*, 18:135–149, 1997b. 17

J. C. R. Hunt, A. A. Wray, and P. Moin. Eddies, stream and convergence zones in turbulent flows. Report CTR-S88, Center For Turbulence Research, 1988. 75

J. Jeong and F. Hussain. On the identification of a vortex. *J. Fluid Mech.*, 285:69–94, 1995. 75

T. A. Johnson and V. C. Patel. Flow past a sphere up to a reynolds number of 300. *J. Fluid Mech.*, 378:19–70, 1999. 86, 87

R. M. Kerr and F. Hussain. simulation of vortex reconnection. *Physica D*, 37:474–484, 1989. 31

S. Kida and M. Takaoka. Vortex reconnection. *Annu. Rev. Fluid Mech.*, 26:169–189, 1994. 31

D. Kim and H. Choi. Laminar flow past a sphere rotating in the streamwise direction. *J. Fluid Mech.*, 461:365–386, 2002. 70, 71, 81, 82, 86, 87

D. Kivotides, J. C. Vassilicos, D. C. Samuels, and C. F. Barenghi. Kelvin waves cascade in superfluid turbulence. *Phys. Rev. Lett.*, 86(14):3080–3083, 2001. 39

D. Kivotides, J. C. Vassilicos, D. C. Samuels, and C. F. Barenghi. Velocity spectra of superfluid turbulence. *Europhys. Lett.*, 57(6):845–851, 2002. 30

P. Koumoutsakos and A. Leonard. High resolution simulation of the flow around an impulsively started cylinder using vortex methods. *J. Fluid Mech.*, 296(1), 1995. 7, 65

P. Koumoutsakos, A. Leonard, and F. Pépin. Boundary conditions for viscous vortex methods. *J. Comput. Phys.*, 113:52–61, 1994. 7, 50, 67

A. Leonard. Computing three-dimensional incompressible flows with vortex elements. *Annu. Rev. Fluid Mech.*, 17:523–559, 1985. 30

J. Lighthill. *Laminar boundary layers*, chapter Attachment and separation in three-dimensional flow. Oxford Univ. Press, 1963. 7, 82

J. H. Maccoll. Aerodynamics of a spinning sphere. *J. Roy. Aero. Soc.*, 32:777–798, 1928. 93

G. Magnus. Ueber die abweichung der geschosse, und ueber: eine auffallende erscheinung bei rotirenden körpern. *Poggendorfs Annalen der Physik und Chemie*, 88:1, 1853. 70

R. M. Merserau. The processing of hexagonally sampled two-dimensional signals. *Proceedings of the IEEE*, 1979. 14, 18

J. J. Monaghan. Extrapolating b-splines for interpolation. *J. Comput. Phys.*, 60: 253–262, 1985. 21

F. Noca, D. Shiels, and D. Jeon. A comparison of methods for evaluating time-dependent fluid dynamic forces on bodies, using only velocity fields and their derivatives. *J. Fluids and Structures*, 13:551–578, 1999. 80

B. Oesterlé and T. Bui Dinh. Experiments on the lift of a spinning sphere in a range of intermediate reynolds numbers. *Exps. Fluids*, 25:16–22, 1998. 70, 93

R. B. Pelz. Locally self-similar, finite-time collapse in a high-symmetry vortex filament model. *Phys. Rev. E*, 55(2):1617–1626, 1997. 31

P. Ploumhans. *Simulation of high Reynolds number flows past bluff bodies using vortex and boundary element method.* Ph.D. thesis, Université Catholique de Louvain, Faculté des Sciences Appliquées, 2001. 7, 10, 65

P. Ploumhans, G. S. Winckelmans, J. K. Salmon, A. Leonard, and M. S. Warren. Vortex methods for direct numerical simulation of three-dimensional bluff body flows: application to the sphere at $re = 300$, 500, and 1000. *J. Comput. Phys.*, 178, 2002. 51, 52, 67, 80, 86, 87

P. Ploumhans and G.S. Winckelmans. Vortex methods for high resolution simulations of viscous flow past bluff-bodies of general geometry. *J. Comput. Phys.*, 165:354–406, 2000. 13, 65, 142

C. J. Pregnalato, M. C. Thompson, and K. Hourigan. Flow transitions in the wake of a streamwise-rotating sphere. Conference on bluff body wakes and vortex-induced vibrations, Port Douglas, Australia, December 2002. 70

A. Pumir and R. M. Kerr. Numerical simulation of interacting vortex tubes. *Phys. Rev. Lett.*, 58(16):1636–1639, 1987. 31

B. Robins. *New principles of gunnery.* ed. Hutton, 1805. first printed in 1742. 70

M. Rubel. Octree algorithms for the implicit closest point transform. To be submitted, 2002. 127

S. I. Rubinow and J. B. Keller. The transverse force on a spinning sphere moving in a viscous fluid. *J. Fluid Mech.*, 11:447–459, 1961. 70, 93

J. K. Salmon and M. S. Warren. Skeletons from the treecode closet. *J. Comput. Phys.*, 111:136–155, 1994. 9, 143, 145

J. K. Salmon, M. S. Warren, and G. S. Winckelmans. Fast parallel tree codes for gravitational and fluid dynamical N-body problems. *The International Journal of Supercomputer Applications*, 8(2):129–142, Summer 1994. ISSN 0890-2720. 9

P. R. Schatzle. *An Experimental Study of Fusion of Vortex Rings*. Ph.D. thesis, California Institute of Technology, 1987. 31, 36, 39

I. J. Schoenberg. *Cardinal spline interpolation*. Society for Industrial and Applied Mathematics, Philadelphia, PA, 1973. 14

M. J. Shelley, D. I. Meiron, and S. A. Orszag. Dynamic aspects of vortex reconnection of perturbed anti-parallel vortex tubes. *J. Fluid. Mech.*, 246:613–652, 1993. 31

Y. Tsuji, Y. Morikawa, and O. Mizuno. Experimental mesaurement of the magnus force on a rotating sphere at low reynolds numbers. *J. Fluids Eng. – Trans. A.S.M.E.*, 107:484–488, 1985. 70, 93

D. Van De Ville, T. Blu, M. Unser, W. Philips, I. Lemahieu, and R. Van de Walle. Hex-splines: a novel spline family for hexagonal lattices. *IEEE Transactions on Image Processing*, 2004. 14, 18, 19, 20

G. S. Winckelmans. Annual Research Briefs, C.T.R. Stanford, 1995. 31

G. S. Winckelmans. *Encyclopedia of Computational Mechanics*, chapter Vortex Methods. John Wiley and Sons, 2004. 6

G. S. Winckelmans and A. Leonard. Contributions to vortex particle methods for the computation of three-dimensionnal incompressible unsteady flows. *J. Comput. Phys.*, 109(2):247–273, December 1993. 5

G. S. Winckelmans, J. K. Salmon, M. S. Warren, and A. Leonard. Application of fast parallel and sequential tree codes to computing three-dimensional flows with the vortex element and boundary element methods. Second International Workshop on Vortex Flows and Related Numerical Methods, Montréal, August 1995. 9

N.J. Zabusky, M.H. Hugues, and K.V. Roberts. Contour dynamics for the Euler equations in two dimensions. *J. Comput. Phys.*, 1979. 47

I. Zawadzki and H. Aref. Mixing during vortex ring collision. *Phys. Fluids A*, 3(5): 1405–1410, 1991. 31